

Thermal management studies for a high temperature proton exchange membrane fuel cell stack

Ellamla Harikishan Reddy

A Dissertation Submitted to
Indian Institute of Technology Hyderabad
In Partial Fulfillment of the Requirements for
The Degree of Doctor of Philosophy



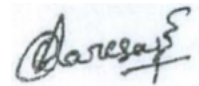
भारतीय प्रौद्योगिकी संस्थान हैदराबाद
Indian Institute of Technology Hyderabad

Department of Chemical Engineering

Jun, 2013

Declaration

I declare that this written submission represents my ideas in my own words, and where others' ideas or words have been included, I have adequately cited and referenced the original sources. I also declare that I have adhered to all principles of academic honesty and integrity and have not misrepresented or fabricated or falsified any idea/data/fact/source in my submission. I understand that any violation of the above will be a cause for disciplinary action by the Institute and can also evoke penal action from the sources that have thus not been properly cited, or from whom proper permission has not been taken when needed.



(Signature)

(E Harikishan Reedy)

(CH09P001)

Approval Sheet

This thesis entitled "**Thermal management studies for a high temperature proton exchange membrane fuel cell stack**" by E Harikishan Reddy is approved for the degree of Doctor of Philosophy from IIT Hyderabad.

P.S.L. 24.6.13

Prof. P. Ghoshdastidar
IIT Kanpur
Examiner

[Signature]
24/6/2013

Prof. Sanjay Mahajani
IIT Bombay
Examiner

[Signature]
24/6/13

Dr. Vinod Janardhanan
IIT Hyderabad
Examiner

[Signature]

Prof. Sreenivas Jayanti
IIT Madras
Supervisor

[Signature]

Dr. Dayadeep Monder
IIT Hyderabad
Supervisor

[Signature]
24/6/2013

Dr. Raja Banerjee
IIT Hyderabad
Chairperson

Acknowledgements

It gives me an immense pleasure to acknowledge my sincere thanks to the people who have helped me directly or indirectly for making this day possible.

I express gratitude to IIT Hyderabad for giving me an opportunity to pursue my PhD program and IIT Madras for providing lab, computational and library facilities. I express my sincere gratitude to my research advisors Prof. Sreenivas Jayanti (IIT Madras) and Dr. Dayadeep S. Monder (IIT Hyderabad) for their valuable guidance and support during my PhD program.

I am extremely fortunate to have Prof. Sreenivas Jayanti as my PhD advisor. I would like to express my heartfelt thanks to him for his constant guidance, encouragement and continuous support throughout my stay at IITM, without which, I could not have finished this dissertation. He has been a great inspiration for me. His concern about students, uninhibited support during tough times, positive attitude and avid thirst for advanced research are highly commendable. He was always there to listen to my ideas and problems and helped in shaping up or coming out of the problem by his critical questioning and enticing pieces of advice. His enlightening discussions on both professional and personal front have helped me a lot while taking critical decisions. I am highly indebted to him for making my stay a comfortable and memorable at IIT Madras. The last few years that I spent with him, have been a great learning experience to me.

My devout thanks to Dr. Dayadeep S. Monder, who is my co-advisor. The cooperation extended by him in a cheerful and friendly manner is always memorable. I am also very thankful to him for reviewing this work.

I would like to thank my doctoral committee members -Dr. Vinod Janardhanan and Dr. Raja Banerjee for their insightful comments, valuable suggestions. My sincere thanks to Prof. Krishnaiah and Dr. Arun K. Tangirala for their support and encouragement during my early days. I thank to Dr. Saptarshi Majumdar, Dr. Sunil K. Maity and faculty of chemical engineering department, IITH. My special thanks to Prof. U B Desai (director, IIT Hyderabad) for providing a conducive environment to work during my PhD program.

Special acknowledgements go to Ravi Kumar Gujjula and Kranthi Maniyam, one of my best pals who is there for me right from the first day of joining and helped me in numerous ways.

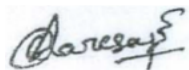
I am also thankful to my friend, Ravi Gujjula, who has carried me on his bicycle patiently for about six months in the IIT Madras, and then on a powered vehicle on the IIT Hyderabad campus. I have enjoyed his company very much on both campuses.

Special thanks to my labmates Dr. Gigi Sebstein, Dr. Srinivas M., Dr. Prabu V., Nowneesh Challa, Harikrishna B., Dr. Suresh A., Satyam Naidu V., Prasad B and also my fuel cell lab group friend Vikas Jaggi and P. V. Suresh. I am fortunate to have good friends -Dr.Vasu Gollangi, Dr. Hemanth B., Arun Srikanth, Anadan Mukesh, Kirthi Vasan, Srinivas Appari, Durga Rao T., Abdual Haq Ghouse, Sudhakara Reddy Y., Vandana N, V.T.S.R. Kumar Reddy, B.V.R.S.N. Prasad, Kiran Ch, Balraju V., V.C.S. Palla, Laxmi, Govardhan P., Nagarajan, Sam David, Rahual Trevedhi, Baswaraju, Balakrishna and Narsimha Reddy.

I would like to thank ‘Comfort Tavera batch (CTB)’ friends - Dr. Kranthi M., Dr. Srinivas M., Dr. Venkat Reddy R., Dr. P. V. Suresh, Pradeep M., Ravi Kumar G., Dr. Sandilya D., Dr. Siva and Harish V., who made my stay at IIT Madras pleasant and unforgettable. I had wonderful time with them during the outing trips and will always cherish fond memories of our time together. I am gratified to them for their support and help during my stay. Thanks to all of them.

My infinite love and thanks are due to my parents, because all what I have accomplished in life is the result their unconditional love and years of sacrifice. My beloved parents, brothers (Dharma and Harinath) loving affection drive me to achieve higher heights in my life. I am thankful to my loving grandparents late Chandhra Kala and Raghava Reddy and their affection and encouragement during all my endeavors. I am thankful my beloved friends Poorna, Harikrishna, Somesh, Ashraf, Koti, Jabes, Gopi, Kali, Padma, Jeevan, Tarangini and Sirisha for their valuable suggestions. Also I thank my wife Srujana for her support, quiet patience during my thesis write-up.

Finally, I would like to thank the ALMIGHTY for providing this opportunity and helped me in countless ways.



Harikishan Reddy Ellamla

DEDICATED
TO
MY BELOVED PARENTS
AND
Prof SREENIVAS JAYANTI

Abstract

Keywords: Thermal management, polymer electrolyte membrane fuel cells, high temperature operation, temperature mapping, computational fluid dynamics, hydrogen storage, current density, pressure drop, flow distribution.

High temperature proton exchange membrane fuel cells (HT-PEMFCs) operate in the temperature range of 100 to 200°C and offer several advantages compared to the better known low temperature proton exchange membrane fuel cells (LT-PEMFCs) which typically operate at temperatures below 100°C. During the operation of a HT-PEMFC stack, heat is generated in the electrodes and electrolyte of each cell, and this heat must be effectively removed without creating any hot or cold spots. Proper thermal management of the HT-PEMFCs stack is required to ensure that the cell temperature is neither too low (which would lead to low cell efficiency) nor too high (which would damage the materials of the stack). The high heat generation rate in HT-PEMFCs, especially at high current densities where it can exceed the total electric power output, poses a challenge to the thermal management of HT-PEMFC stacks.

Against this background, the objective of the present work is to systematically study the thermal management of an HT-PEMFC stack and quantify the effect of various stack cooling strategies on the overall performance of the stack using a multi-scale computational fluid dynamics (CFD) model. The stack model couples the flow and temperature fields with the electrochemistry using an empirical cell polarization curve to capture local current density - a function of local temperature within the active regions of each cell. This approach greatly reduces computational effort and time while retaining the essential physics and the coupling between the temperature and current density fields, thus enabling studies that clarify thermal management at the stack level: the focus of this study. A specific goal of this study is to investigate stack cooling methods that enable as high an average stack temperature as possible while ensuring that the temperature does not exceed 200°C anywhere in the stack. The thermal management techniques investigated in this work are: i) integrated cathode air cooling, ii) external air flow over the hot stack, iii) coupling a H₂ storage system to the cathode air cooling system, iv) the use of liquid coolants in a separate cooling circuit.

Integrated cathode air cooling uses excess air directed through cooling channels between cells to remove heat from the stack before directly introducing this air into the channels feeding air to the cell. A large air-side stoichiometric factor of the order of 10 is required to maintain cell temperature under 200°C using this approach, but a combination of cathode air cooling and external air cooling can give good heat management in a transport application with lower air flow-rates. As a hydride based H₂ storage system absorbs heat in fuel supply mode, this heat sink can be used to cool the fuel cell stack. Extension of the integrated cathode air cooling model to use the heated air for H₂ desorption from a sodium alanate based hydrogen storage system shows that, with a cathode air flow rate seven times in excess of the stoichiometric requirement, it is possible to meet the triple requirement of supplying preheated cathode air, maintaining uniform stack temperature, and supplying the heat required for desorption of the required amount of H₂.

While air cooled systems are simpler to design, liquid cooled stacks promise better performance and this work investigates the possibility of using a separate liquid coolant circuit to cool the stack. Several key design and operating parameters for a liquid cooled HT-PEMFC stack are varied to examine their effects on stack performance. The parameters varied include cooling plate material, number of cooling plates, cathode/coolant inlet temperatures, cell/stack voltage, channel geometry and flow field configurations. This detailed parametric analysis of the HT-PEMFC stack shows that considerable scope exists for fine-tuning the design to achieve a desired level of stack performance.

Finally, the role of cell size in stack thermal management is examined. The results show that stacks up to 5 kWe in size can be adequately cooled with cathode air alone or in combination with external air cooling thus showing potential for small scooter/motorcycle applications. Stacks larger than 5 kWe need liquid cooling and while it may be sufficient to use parallel flow fields in the cooling plate to avoid excessive pressure drop losses, a four parallel serpentine flow field in the bipolar plates is recommended with graphite cooling plate.

LIST OF SYMBOLS

$\Delta H_{g,T}$	enthalpy of water formation in gas phase (J)
ΔG_T	Gibbs free energy (J)
ΔP	pressure drop (Pa)
ΔT_{cat1}	maximum to minimum temperature difference on CCL-1 (K)
ΔT_{cat2}	maximum to minimum temperature difference on CCL-2(K)
ΔT_{oil}	cooling oil inlet to outlet temperature difference (K)
A	area (m ²)
C _p	specific heat of the medium (J/kg K)
D	hydraulic mean diameter (m)
F	Faraday constant (C/mol)
f	friction factor
Gr	Grashof number
h	convective heat transfer coefficient (W/m ² k)
i	current density (A/m ²)
i _{avg}	volumetric average current density (A/m ²)
j	type of edges
I	current (A)
i _o	exchange current density (A/m ²)
k	thermal conductivity (W/m k)
m	mass flow rate (kg/s)
n	number of electrons in electrochemical reaction
N _{cell}	number of cells
Re	Reynolds number
Nu	Nusselt number
P	electrical power (W)
p	static pressure (Pa)
Pr	Prandtl number
Q	thermal energy produced by reaction (W)

q_{catalyst}	volumetric heat produced in the catalyst (W/m^3)
Q_{irrev}	irreversible heat of reaction (W)
Q_{rev}	reversible heat of reaction (W)
R_{conc}	concentration losses
R_{ohmic}	ohmic losses
Ra	Rayleigh number
Se	volumetric source term (W/m^3)
T	temperature (K)
T_f	film temperature (K)
U	free stream velocity (m/s)
V	voltage (V)
V_{catalyst}	volume of the catalyst (m^3)

Subscripts:

cell	single cell
st	stack
Surf	surface of the layer
Core	core of the layer
Cin	coolant inlet
Cout	coolant outlet
Bin	cathode air inlet
Bout	cathode air outlet
r	reactants

Greek letters:

α_c	cathode charge transfer coefficient
λ	stoichiometric factor
ρ	density of the medium (kg/m^3)
ε	emissivity of the material

μ	dynamic viscosity of the medium (kg/m s)
ν	kinematic viscosity of the medium (m ² /s)
β	thermal expansion coefficient (1/K)
σ	Stefan-Boltzmann constant

Abbreviations

CCL	Cathode Catalyst Layer
CFF	Cathode Flow Filed
CFD	Computational Fluid Dynamics
CP	Cooling Plate
FPSC	Four Parallel Serpentine Channels
GDL	Gas Diffusion Layer
HT-PEMFC	High Temperature Polymer Electrolyte Membrane Fuel Cell
LT-PEMFC	Low Temperature Polymer Electrolyte Membrane Fuel Cell
PC	Parallel Channels
PEM	Polymer Electrolyte Membrane
MCFC	Molten Carbonate Fuel Cell
PAFC	Phosphoric Acid Fuel Cell
SOFC	Solid Oxide Fuel Cell

Contents

Declaration	ii
Approval sheet	iii
Acknowledgements	iv
Abstract	viii
Nomenclature	X
CHAPTER 1 INTRODUCTION	1
1.1 Overview of fuel cells	1
1.2 History of fuel cells	2
1.3 Fuel cell working principle	2
1.4 Fuel cell technologies	3
1.4.1 Low temperature PEM fuel cell (LT-PEMFC)	4
1.4.2 High temperature PEM fuel cell (HT-PEMFC)	4
1.4.3 Direct methanol fuel cell	6
1.4.4 Phosphoric acid fuel cell (PAFC)	6
1.4.5 Molten carbonate fuel cell (MCFC)	6
1.4.6 Solid oxide fuel cell (SOFC)	7
1.5 Choice of fuel cell system for study	7
1.6 Advantages of high temperature operation	8
1.6.1 Fuel cell performance as a function of temperature	8
1.6.2 Improved cathode kinetics	9
1.6.3 Improved tolerance of the catalyst to contaminants	9
1.6.4 Other benefits of high temperature operation	9
1.7 HT-PEMFC performance and losses	9
1.8 Thermal management - A critical issue	11
1.9 Motivation for the present study	13

CHAPTER 2	LITERATURE REVIEW	14
2.1	Fuel cell modeling	14
2.1.1	Catalyst layer modeling	15
2.1.2	Cell level modeling	18
2.1.3	Stack level modeling	23
2.2	Thermal management PEM fuel cell stack	36
2.2.1	LT-PEMFC cooling techniques	36
2.2.2	HT-PEMFC cooling techniques	30
2.3	Objectives and scope of the present work	32
CHAPTER 3	PROBLEM FORMULATION AND MODEL DESCRIPTION	34
3.1	Problem formulation	34
3.1.1	Statement of the thermal management problem	34
3.1.2	Description of the HT-PEMFC stack	35
3.1.3	Estimation of the thermal load	36
3.1.4	Estimation of heat losses from the stack	41
3.2	Physical description of thermal model for a 1 kWe HT-PEMFC stack	43
3.2.1	Integrated cathode air cooling	45
3.2.2	Additional heat removal through a coupled H ₂ storage system	46
3.2.3	External cooling with air-flow over stack	47
3.2.4	Cooling with a liquid coolant	49
3.3	Computational models	51
3.3.1	Governing equations	51
3.3.2	Boundary conditions	52
3.3.3	Grid independence	52
3.3.4	Numerical details	54

3.3.5	Validation	54
CHAPTER 4	EVALUATION OF DIFFERENT THERMAL MANAGEMENT OPTIONS	57
4.1	Integrated cathode air cooling	58
4.1.1	Heat removal primarily by cathode air	58
4.1.2	Taking account of current density variation with temperature	61
4.2	Additional heat removal through a coupled H ₂ storage system	65
4.2.1	Constant current density	66
4.2.2	Varying current density	69
4.3	Heat removal by forced air circulation over the stack	72
4.3.1	Heat removal assisted by forced convection	72
4.3.2	Heat removal by forced convection alone	75
4.4	Heat removed by liquid coolants	76
4.4.1	Coolant medium	76
4.4.2	Heat removed by heat transfer oil	76
4.5	Parametric studies	80
4.5.1	Cathode air stoichiometric factor	81
4.5.2	Operating voltage	82
4.5.3	Number of cooling plates	83
4.5.4	Cooling plate material	85
4.5.5	Specific power density and optimal configuration for a 1 kWe stack	85
4.6	Summary	87
4.6.1	Integrated air cooling	87
4.6.2	Coupling thermal management with H ₂ storage tank	88
4.6.3	External air flow over the stack	88

4.6.4	External cooling with heat transfer oil	89
CHAPTER 5 OPTIMIZATION OF THE STACK COOLING SYSTEM		90
5.1	Design of flow fields	91
5.2	Flow fields for the reactants	91
5.3	Flow fields for the coolant	99
5.4	Pressure drop estimation in manifolds	102
5.4.1	Type of manifolds	102
5.4.2	Methodology for pressure drop calculations	104
5.4.3	Pressure drop in the air manifold	106
5.4.4	Pressure drop in the fuel manifold	107
5.4.5	Pressure drop in the coolant manifold	108
5.5	Scale up for higher power	110
5.5.1	External air flow over the stack	110
5.5.2	Integrated cathode air cooling	111
5.5.3	Liquid coolant	112
5.5.4	Stack design	117
5.6	Summary	119
CHAPTER 6 CONCLUSIONS		120
REFERENCES		123
APPENDIX		132
LIST OF PUBLICATIONS BASED ON THESIS		136

CHAPTER-1

INTRODUCTION

1.1 Overview of fuel cells

A fuel cell (FC) is an electrochemical device which converts the chemical energy of a fuel and an oxidant, supplied continuously from external sources, directly into electrical energy without chemical combustion, with heat and water as by-products, and zero or very low harmful emissions (Figure 1.1). The fuel is typically an alcohol or a hydrocarbon or a substance derivable from it, e.g., hydrogen, which can be supplied continuously. A fuel cell shares many features with batteries. The principle of operation is similar to that of batteries but it gives energy continuously as long as the fuel and oxidant are supplied. A fuel cell consists of three basic components, anode, cathode and electrolyte. Fuel cells can be used in virtually any application requiring electrical power from a few milli-watts up to multi-kilowatt and megawatt sizes. They can be used in transport applications by replacing internal combustion engines or batteries and also in powering consumer devices such as laptops and cell phones. Efficiencies of present fuel cell plants are in the range of 40 to 60%, and hybrid fuel cell/gas reheat turbine cycles have demonstrated efficiencies greater than 70%. In addition, the efficiency is nearly independent of

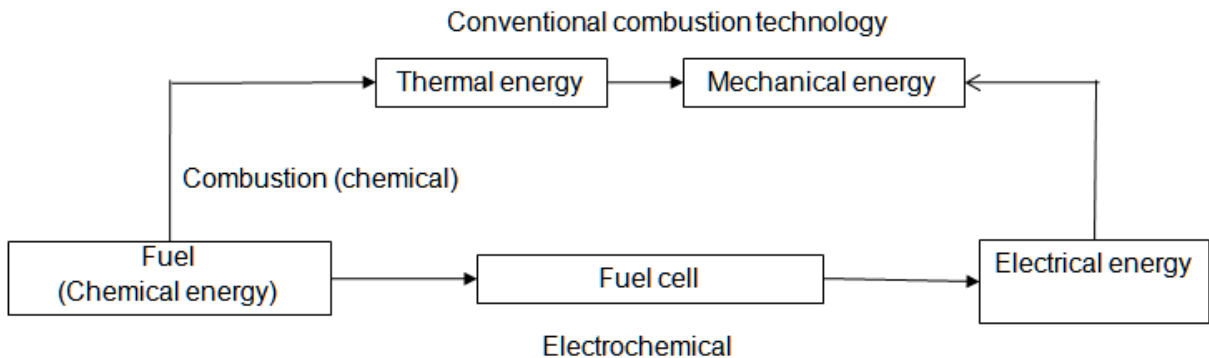


Figure 1.1: Fuel cell technology (direct energy conversion) in comparison with conventional technology (indirect energy conversion).

the electric load down to a small fraction of full load. They can also be used in stationary power applications such as to provide electricity for a home or a firm. Basically, a fuel cell can supply clean (low or no emissions), quiet, vibration-free electricity without the need to frequently

dispose of the fuel cell when its fuel is used up. The fuel cell also has cogeneration capability; the exothermic chemical and electrochemical reactions produce usable heat and water as by-products.

1.2 History of fuel cells

The fuel cell principle was discovered by Christian Friedrich Schonbein in 1839 and a working fuel cell was demonstrated by Sir William Grove shortly afterwards as an energy conversion system (Breiter, 1969). During and after the second World War, fuel cells were recognized as a potential energy source, with the development of solid electrolytes by Davtyan in 1946 for high temperature fuel cells with carbonaceous fuels. In 1932 Francis Thomas Bacon, and his coworkers started working on alkaline fuel cells and in the year of 1958 they demonstrated a working 5 kW alkaline fuel cell stack. The alkaline fuel cell technology was licensed to Pratt and Whitney where it was utilized for the Apollo spacecraft fuel cells. In the 1960s, NASA successfully demonstrated the potential applications of the fuel cell technology in space flights with high conversion efficiency and low pollutant emissions while providing power for its space flights. From then onwards, various developments have taken place as a result of continued and sustained research on all types of fuel cells. For phosphoric acid fuel cells, carbon diffusion electrodes with catalyst added for better performance were introduced by Kordesch(Kordesch, 1963). Ion exchange membranes with a thin layer of catalyst deposited on it were brought into operation by Grubb and Neidrach (Grubb and Niedrach, 1960; Niedrach and Alford, 1965) on a hydrogen-oxygen fuel cell at low temperatures. Over the recent past decades, the increase in the world's energy demands, uses and the need for more electrical energy and the increased concern over the environment engendered fresh interest and investment by many countries in the research and development of fuel cell technology. Despite significant breakthroughs that have been achieved, substantial improvement is still required in making the technology more efficient and economically viable.

1.3 Working principle of a fuel cell

The basic physical structure of a fuel cell consists of an electrolyte layer (ion conductor), sandwiched between an anode and a cathode. A schematic representation of a unit cell with the reactant/product gases and the ion conduction flow directions through the cell is shown in Figure

1.2. The electrolyte may be liquid or solid depending on the type of fuel cell. In a liquid electrolyte the gases diffuse through a thin electrolyte film (wet portion of the porous electrode) and react electrochemically on their respective electrode active surfaces. In solid electrolyte fuel cells, a large number of catalyst sites are created at the interfaces that are electrically and ionically connected to the electrode and the electrolyte respectively, and these catalyst sites are efficiently exposed to the reactant gases. In a typical fuel cell, the fuel is continuously fed to the anode and oxidant is fed to the cathode. The electrochemical reactions taking place at the cathode/anode produce ions which pass through the electrolyte and electrons (electrical current) which while passing through the external circuit produce electrical power output.

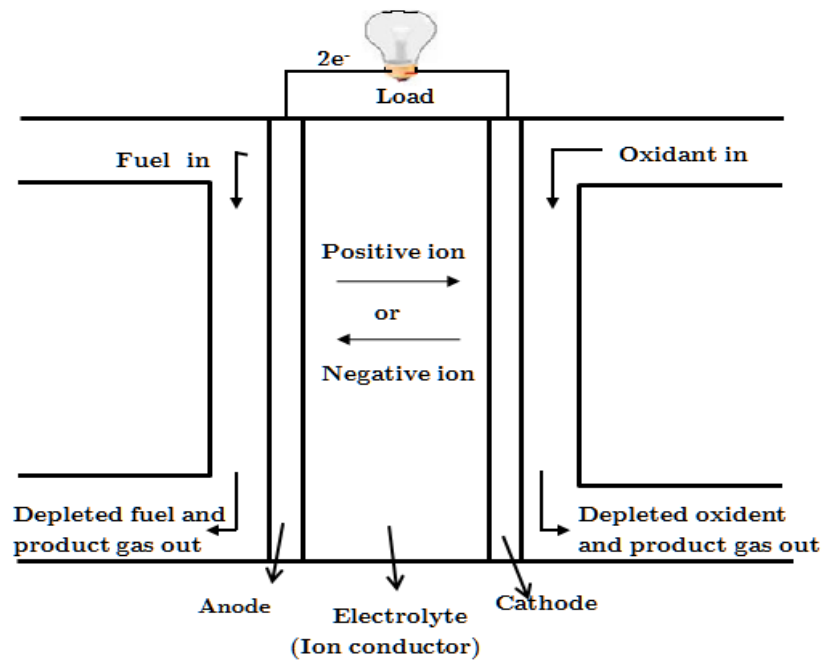


Figure 1.2: Schematic of an individual fuel cell

1.4 Fuel cell technologies

Fuel cells are typically classified based on their operating temperature range, type of electrolyte is used, type of fuel and oxidant. Several types of fuel cells are under development and a few of the promising types include:

- Low Temperature Polymer Electrolyte Membrane Fuel Cells (LT-PEMFC)
- High Temperature Polymer Electrolyte Membrane Fuel Cells (HT-PEMFC)

- Direct Methanol Fuel Cells (DMFC)
- Phosphoric Acid Fuel Cells (PAFC)
- Alkaline Fuel Cells (AFC)
- Molten Carbonate Fuel Cells (MCFC)
- Solid Oxide Fuel Cells (SOFC)

The choice of a fuel cell is determined by its application. A detailed comparison of the fuel cells is given in Table 1.1. Among these types, the DMFC uses liquid methanol as fuel. LT- and HT-PEMFCs are considered apt for transportation and portable applications because of their high power density and quick startup.

1.4.1 Low temperature PEM fuel cell (LT-PEMFC)

LT-PEMFCs use a polymer electrolyte membrane and have an operating temperature below 80°C. Nafion[®] is one such commercially used membrane, which is based on sulphonated polytetrafluoroethylene. Proton conductivity of the membrane depends on the liquid water content in the membrane, and limits the operating temperature of the LT-PEMFCs to below 80°C. As temperature increases, liquid water starts evaporating rapidly and the membrane gets dehydrated. LT-PEMFCs are a well established technology and have high cell voltages and high efficiencies but have disadvantages such as needing pure hydrogen as fuel (CO tolerance below 20 ppm) and needing continuous humidification of the reactants. Water management is difficult and it needs large active cooling areas to prevent overheating.

1.4.2 High temperature PEM fuel cell (HT-PEMFC)

Conventional PEMFCs use Nafion[®] and other polymer membranes which are restricted in their operation to the rather low temperature range of 60-100°C. Their performance is sensitive to the hydration state of the polymer membrane: too little humidification will lead to reduced proton conductivity and too much humidification will lead to flooding, resulting again in severe loss of performance (Li, 2006). In recent years, a number of alternative polymer membranes have been developed which enable operation in the range of 120-200°C. Higher temperature operation brings in certain advantages: higher tolerance to carbon monoxide (CO) of up to 3-5% by volume enabling a wider choice of fuel; less sensitivity of protonic conductivity

Table 1.1: Important features of different fuel cells classified based on the electrolyte (Carrette et al., 2001).

	AFC	DMFC	LT-PEMFC	HT-PEMFC	PAFC	MCFC	SOFC
Operating temperature	< 100°C	< 100°C	60°C - 80°C	100°C - 200°C	160°C - 220°C	600°C - 700°C	700°C - 1000°C
Electrolyte	KOH	Polymer membrane	Polymer membrane	Polymer membrane	≈100% phosphoric acid stabilized in an SiC based matrix	Li ₂ CO ₃ / K ₂ CO ₃ materials stabilized in an alumina based matrix	ZrO ₂ supported ceramic electrolytes
Fuel compatibility	H ₂ (external reformer)	Methanol (liquid fuel)	H ₂ , methanol or ethanol (external reformer)	H ₂ (< 5% CO), methanol or ethanol (on-board reformer)	H ₂ (external reformer)	H ₂ , CH ₄ (internal reformer)	H ₂ , CH ₄ , CO (internal reformer)
Anode reaction	$H_2 + 2OH^- \rightarrow 2H_2O + 2e^-$	$CH_3OH + H_2O \rightarrow 6H^+ + 6e^- + CO_2$	$H_2 \rightarrow 2H^+ + 2e^-$	$H_2 \rightarrow 2H^+ + 2e^-$	$H_2 \rightarrow 2H^+ + 2e^-$	$H_2 + CO_3^{2-} \rightarrow H_2O + CO_2 + 2e^-$	$H_2 + O^{2-} \rightarrow H_2O + 2e^-$
Cathode reaction	$1/2 O_2 + H_2O + 2e^- \rightarrow 2OH^-$	$3/2 O_2 + 6H^+ + 6e^- \rightarrow H_2O$	$1/2 O_2 + 2H^+ + 2e^- \rightarrow H_2O$	$1/2 O_2 + 2H^+ + 2e^- \rightarrow H_2O$	$1/2 O_2 + 2H^+ + 2e^- \rightarrow H_2O$	$1/2 O_2 + CO_2 + 2e^- \rightarrow CO_3^{2-}$	$1/2 O_2 + 2e^- \rightarrow O^{2-}$
Charge carrier in the electrolyte	OH ⁻	H ⁺	H ⁺	H ⁺	H ⁺	CO ₃ ²⁻	O ²⁻
Start-up time	min	Sec	sec-min	Min	Hours	hours	hours
Applications	Transportation, Space, Military, Energy storage system				Combined heat & power for decentralized stationary power	Combined heat & power for stationary decentralized systems & for transportation.	
Realized power	5-150 kW (modular)	100 mW-1 kW	5-250 kW (modular)		Small - medium sized plants 50 kW - 11 MW	Small power plants 100 kW - 2 MW	Small power plants 100 - 250 kW

to humidification leading to simplification of the water management system; enhanced kinetics; and the possibility of using the exhaust gases for on-board fuel reforming or for other thermal systems (Zhang et al., 2006).

1.4.3 Direct methanol fuel cell

The direct methanol fuel cell (DMFC) uses a polymer membrane as electrolyte. A mixture of liquid water and methanol is supplied to the anode side of the membrane and air is supplied to the cathode side. Due to liquid methanol supply at the anode, the cooling and humidification processes are simplified. Liquid fuel also makes these fuel cells a good choice for low power electronic applications like laptops and mobiles. One of the main problems with DMFC is the crossover of methanol to the cathode side of the fuel cell and the formation of CO₂ bubbles on the cathode flow field. The crossed-over methanol gets combusted catalytically on the cathode side and lowers the efficiency of the cell (Suresh and Jayanti, 2011).

1.4.4 Phosphoric acid fuel cell (PAFC)

PAFCs have typical operating temperatures of 150-200°C. Concentrated phosphoric acid is used as the electrolyte and platinum is the electrocatalyst on both the electrodes. PAFCs have been used for stationary power generators with a power output in the 100 - 400 kW range and they are also finding application in heavy vehicles. PAFC has a CO tolerance of up to 1.5% by volume. Some of the disadvantages of PAFCs include the corrosive nature of the electrolyte and relatively low power density.

1.4.5 Molten carbonate fuel cell (MCFC)

MCFCs are typically operated in the temperature range of 600-700°C. An electrolyte composed of a molten carbonate salt mixture is suspended in a porous, chemically inert ceramic matrix of beta-alumina solid electrolyte (BASE). Due to high temperature operation, non-precious metals can be used as catalyst on the both the anode and the cathode. MCFCs not require an external reformer to convert more energy-dense fuels to hydrogen; the anode act as a internal reformer and has a high CO tolerance. The high temperature operation of MCFCs and the corrosive nature of electrolyte accelerates component breakdown and corrosion, decreasing cell life.

1.4.6 Solid oxide fuel cell (SOFC)

SOFCs are operated typically above 700°C with nonporous metal oxides and ceramic materials are used in the membrane electrode assembly (MEA). Because of the very high temperatures, nickel can be used as a catalyst avoiding the expensive precious metal catalysts. These fuel cells are in the pre-commercial stage for stationary power generation. The solid oxide fuel cells can be either of planar or tubular shape. Tubular configurations do not suffer from sealing issues and fairly large units (~100kW) have been demonstrated successfully for combined heat and power applications without any performance degradation over two years. Other interesting features of SOFCs are that internal steam reforming is possible which also provides internal cooling of the cells (due to endothermal nature of the reforming reaction). CO can be used as a fuel for SOFCs. Due to high temperature operation, SOFCs require significant amounts of special alloys and/or special ceramics as well as thermal insulation. Another disadvantage of the SOFC systems is the slow start-up time which makes them less useful for mobile applications.

1.5 Choice of fuel cell system for study

The choice of fuel cell system is mainly based on the type of application and the power required. DMFC are well suited for small power applications and are also highly portable. Methanol can be used as liquid fuel for DMFC but it has lower efficiency than hydrogen powered fuel cells. Fuel cells like SOFC, MCFC also have high performance but the manufacturing costs are high and they need high volume of insulation (due to their high temperature operation). HT-PEMFCs have higher efficiencies and are more suitable for transport application compared to LT-PEMFCs. Fuel storage and distribution for portable systems depends on whether hydrogen or methanol is used. Due to high temperature operation, HT-PEMFCs, can be used with on-board fuel reformers by using waste heat from the fuel cell. The hydrogen, which is produced from the fuel reformer can be used as a direct fuel to the HT-PEMFC (with up to 5% CO). Hydrogen storage and distribution for portable applications can be simplified by coupling HT-PEMFCs with an H₂ storage tank. The thermal energy from the fuel cell can be used to release the H₂ from a metal hydride tank. Due to the above advantages HT-PEMFCs show a lot of promise, especially for transportation applications.

1.6 Advantages of high temperature operation

PBI membrane based HT-PEMFC have several advantages, due to their high operating temperature compared to LT-PEMFC. These are as follows:

1.6.1 Fuel cell performance as a function of temperature

Polarization curves obtained using PBI-based HT-PEMFC at different temperatures and ambient backpressure with zero humidification hydrogen and non-humidified air as reactant gases, are shown in Figure 1.3 (Zhang et al., 2007). It can be seen that fuel cell performance increases as the cell operating temperature increases. The improvement in performance (in the form of reduced voltage losses) is greater at high current density.

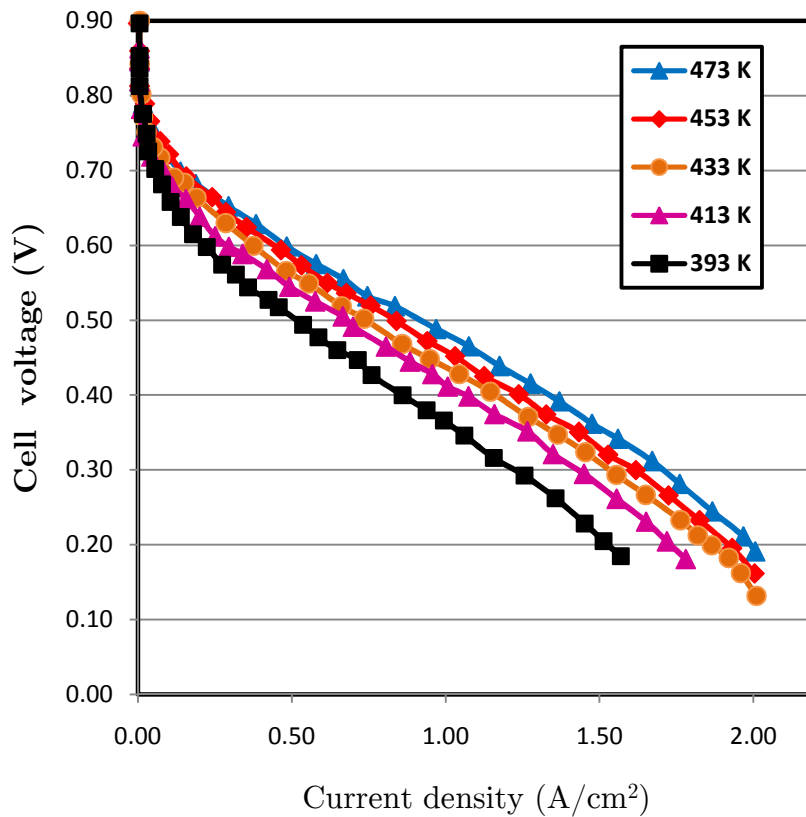


Figure 1.3 Polarization curves obtained at ambient back pressure, 0% RH and different temperatures (as marked) $\lambda_{H_2} = 1.5$ and $\lambda = 2.0$ (Zhang et al., 2007).

1.6.2 Improved cathode kinetics

The exchange current density for oxygen reduction reaction (ORR) is much smaller than that for the hydrogen reduction reaction. The overall electrochemical kinetics is thus primarily determined by the ORR, which can be expressed by a Tafel equation. Experimentally, the Tafel equation slope corresponding to the ORR increases with increase in temperature in the low current density region and it remains independent in the high current density region. The exchange current density is also dependent on the level of acid doping and the method of preparation of the anode and the cathode catalyst layers.

1.6.3 Improved tolerance of the catalyst to contaminants

The carbon monoxide (CO) concentration affects the performance of the fuel cell. The reformat gases generally contain CO and as the CO concentration increases, it will strongly adsorb on the surface of the platinum. The adsorption of CO on the Pt surface is associated with a high negative entropy and is less favourable at high temperatures. Therefore an increase in operating temperature implies lower CO coverage and a correspondingly higher CO tolerance. The high CO tolerances allows H₂ production from an on-board fuel reformer and it allows the direct feeding of the reformer output as a fuel to the cell.

1.6.4 Other benefits of high temperature operation

If a cell is operated at high temperatures, the waste heat can be used as thermal energy for applications such as fuel reforming, hydrogen desorption, direct indirect heating or for co-generation of power. This can lead to an increase in the overall efficiency of an HT-PEMFC based system.

1.7 HT-PEMFC performance and losses

The performance of a fuel cell is characterized by a current density vs. potential plot, which is also called as the polarization curve. The major voltage losses in the fuel cell are activation polarization, ohmic polarization and concentration polarization. The activation losses arise from the need to move electrons and to break and form chemical bonds in the anode and cathode. Part of the energy is lost in driving the chemical reaction that transfers the electrons to and from the

electrode. The activation polarization on the anode side is negligible because of fast reaction kinetics compared to that at the cathode reaction. The ohmic polarization is due to the resistance to the flow of H^+ ions in the membrane and of the electrons in the bipolar plate, GDL and rest of the circuit. It is mainly depends on the conductivity of electron in the electrolyte.

The mass transport or concentration polarization happens due to the lack of reactants at the reaction sites. The concentration polarization usually happens on the cathode side, because of the lower diffusivities of oxygen compared to hydrogen. At low current densities, the catalyst is connected via a pore network with the gas phase. Therefore the diffusion of oxygen is fast at low current densities. At higher current densities, the rate of consumption of reactants and production of water is greater. The water has to be removed at a faster rate; otherwise the increase in the liquid volume leads to the flooding of catalyst pores which reduces the effective diffusion coefficient of the oxygen. Figure 1.4 shows the polarization for different current densities at cell

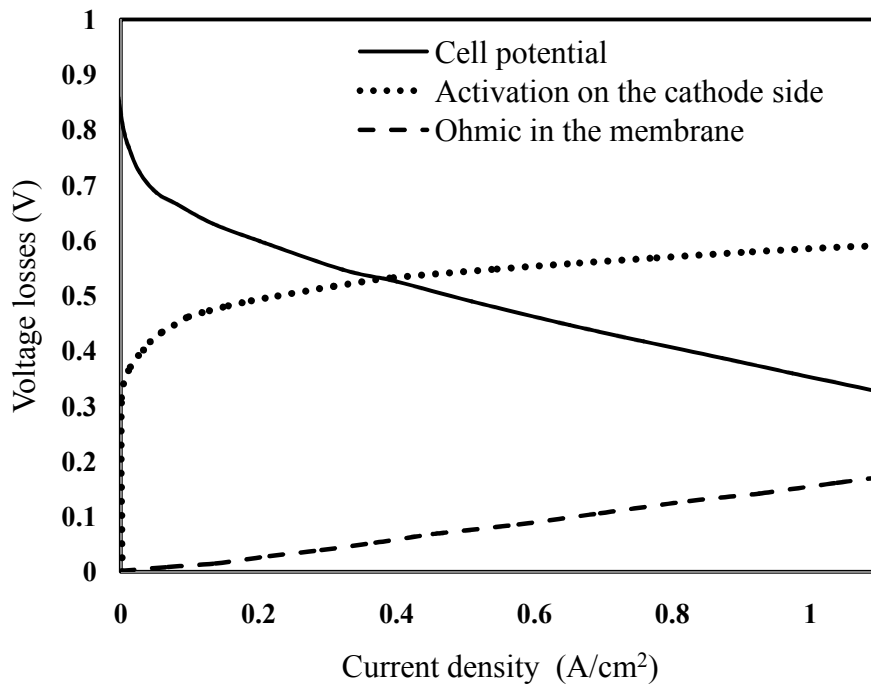


Figure 1.4 A typical polarization curve for an HT-PEMFC and its major voltage losses (Shamardina et al. 2010).

operating temperature of 433 K. It can be observed that the activation polarization is the dominant loss mechanism at low current densities on the cathode side up to about 0.5 A/cm^2 and

it is almost constant at high current densities. Ohmic polarization varies linearly with increase in the current density and becomes a significant contributor (amounting to a loss of 0.1 V) at current densities higher than 1.1 A/cm^2 . The largest part of the voltage loss is due to the cathode activation and membrane resistance. The cell efficiency can be improved if the exchange current density is increased or the cell resistance is decreased.

1.8 Thermal management - A critical issue

An important consideration in the operation of HT-PEMFCs is their thermal management which is needed to prevent the formation of hot spots and to maintain uniform temperature throughout. Despite the advantages of working at high temperatures, the performance of HT-PEMFCs is currently well below that of normal PEMFCs operating at about 80°C as shown in Figure 1.5. The heat generation rate in HT-PEMFC is higher compared to the LT-PEMFC and it exceeds the electrical power output as the current density increases as can be seen in the experimental data shown in Figure 1.5. The heat energy released by the fuel cell is the sum of the irreversible polarization losses and the reversible entropic heat generation (Ju et al, 2005a; 2005b). This heat generation rate imposes a great challenge at higher current densities. For example, if the HT-PEMFC is operated at a current density of 1.1 A/cm^2 the rate of heat generation is about 28% greater than that of the LT-PEMFC and the power density is about 32% lesser than the LT-PEMFC. Thus, during the operation of HT-PEMFCs, say, at a cell voltage of 0.6 V, more than half of the chemical energy of the reactants is converted to thermal energy. This heat is continuously generated as long as the cell is in operation and needs to be removed for the fuel cell to operate at a steady temperature. It is also necessary that, in the process of heat removal (which is primarily by conduction through the media involved), high temperature zones are not created within the cell. Non-uniform temperature distribution leads to variations in the rates of electro-chemical reactions. In addition, it may lead to the creation of local hotspots which may damage the cell. Although the thermal resistance of the PBI membrane, which is being studied extensively as a candidate for an HT-PEMFC, is high, temperatures higher than 473 K are not advisable because the proton conductivity of PBI depends on the doping level of the phosphoric acid. The degradation of the membranes is classified as chemical/electrochemical degradation and physical degradation. During the chemical/electrochemical process, the decomposition of hydrogen peroxide results in the formation of intermediate products (HO^* and HO_2^*) which

causes membrane degradation (Liu and Zuckerboard, 2005). There are two pathways for the generation of free radical species from hydrogen peroxide. Firstly, generation at the cathode due to the electrochemical two-electron reduction of oxygen (Guo et al., 2009), and secondly, generation at the anode owing to chemical combination of crossover oxygen and hydrogen at the anode (Buchi et al., 1995; Xie et al., 2005). Till date several approaches have been adopted to improve the membrane durability; the passive approach was to improve the polymer stability by synthesizing short side chain polymers (Zhou et al., 2007; Merlo et al., 2007), and adopting novel hydrocarbon polymer electrolytes (Trogadas and Ramani, 2007), and the active approach was to suppress free radicals attack by avoiding hydrogen peroxide formation or by destroying hydrogen peroxide (Aoki et al., 2006; Xu et al., 2007), and by scavenging free radicals (Trogadas et al., 2008). At high temperature, the membrane may dry up because of phosphoric acid evaporation. High temperatures have a great influence on the carbon support of the catalysts and degradation of other components. Therefore, proper thermal management is necessary in order to maintain good performance of HT-PEMFCs.

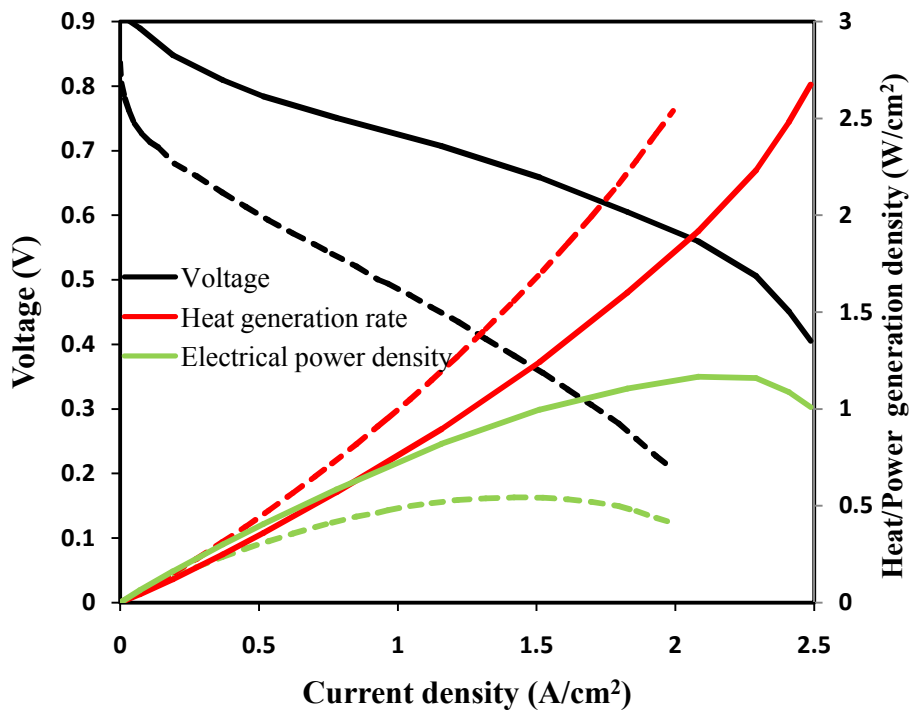


Figure 1.5 Heat and electrical power density at different current densities for HT-PEMFC (dashed lines) (Zhang et al., 2007), and LT-PEMFC (solid lines) (Lampinen and Fomino, 1993).

1.9 Motivation for the present study

The power requirement for transport applications varies from 1-100 kWe. In order to cater to accommodate this range of power requirements, either the cell active area or the number of cells in the stack has to be varied. The number of cells in the stack is restricted due to mechanical strength considerations of the stack. Increase in the cell active area/stack size poses challenges to the thermal management and temperature distribution across the individual cell layers in the stack. The temperature gradients inside the fuel cell impose thermal stresses on the respective materials and is a source of accelerated degradation or failure of the stack. The electrochemical reaction rate is sensitive to the temperature and an increase in the cell temperature gradients leads to a non-uniform current density distribution across the catalyst layer. In the present study, we study thermal management strategies for HT-PEMFC stacks of different sizes. Understanding the effect of various operational and design parameters on the net power output from the stack and the evaluation of different strategies for thermal management of HT-PEMFC stacks for transport applications are the main aims for this study.

CHAPTER-2

LITERATURE REVIEW

HT-PEMFCs are gaining increasing attention as the most promising energy converters due to their high CO tolerance, low operating temperatures and quick start-up compared SOFC, low operating cost and the possibility of on-board fuel reforming compared to the LT-PEMFCs and ultra low toxic emissions (zero toxic emission if pure hydrogen is used as fuel) compared to conventional energy systems. The major application of HT-PEMFCs can be found in the transportation sector like buses, ships, powered trains and aircrafts.

Presently, there are two major types of HT-PEMFCs studied in the literature. They are classified based on the operating temperature and the type of membrane is used. The polysulfonic acid (Nafion) based membrane HT-PEMFCs are typically operated in the temperature range of 110-120°C. The existing LT-PEMFCs models are useful for the Nafion based HT-PEMFCs and can be readily used. The cells with PBI-doped with phosphoric acid based membrane are typically operated in the temperature range of 100-200°C. A number of modeling and experimental studies on LT-PEM fuel cells have appeared in the literature; however, HT-PEMFC models are not abundant at present. The existing LT-PEMFCs, SOFC models can be easily adapted for HT-PEMFCs. The models for reformat fed HT-PEMFCs need further description and modification of the electrochemistry because of the presence of CO. The models of the flow fields etc. are simpler, because of water formation in gas phase. A brief review of the literature relevant to the present study is given below.

2.1 Fuel cell modeling

Fuel cell models can be categorized as analytical, semi-empirical or mechanistic. Mechanistic models can be further subcategorized based on the solution strategy as single-domain or multi-domain (Cheddie and Munroe, 2005). Analytical models may be useful if quick calculations are required for simple systems.

Semi-empirical modeling combines theoretically derived differential and algebraic equations with empirically determined relationships. Empirical relationships are employed when

the physical phenomena are difficult to model or the theory governing the phenomena is not well understood. Semi-empirical models are, however, limited to a narrow range of operating conditions. They cannot accurately predict performance outside of that range. They are very useful for making quick predictions for designs that already exists. Mechanistic modeling has received the most attention in the literature. In mechanistic modeling, differential and algebraic equations are derived based on the physics and electro-chemistry governing the phenomena internal to the cell. These equations are solved using some sort of computational method. Mechanistic modeling has received the most attention in the literature.

In mechanistic modeling, differential and algebraic equations are derived based on the physics and electro-chemistry governing the phenomena internal to the cell. These equations are solved using computational methods. Mechanistic modeling (single and multi-domain) has been utilized to study a wide range of phenomena including polarization effects (activation, ohmic and concentration overpotentials), water management, thermal management, CO kinetics, catalyst utilization and flow field geometry (Bernardi, 1990; Bernardi and Verbrugge,1992).

Multi-domain models involve the derivation of different sets of equations for each region of the fuel cell, namely the anode and the cathode gas diffusion regions, the anode and cathode gas flow channels, the membrane and the catalyst layers. These equations are solved separately and simultaneously. Single-domain models involve the derivation of different sets of equations for the entire domain of interest with source and sink terms accounting for species consumption and generation within cell (Wang et al., 1998; Zhou and Liu, 2001)

2.1.1 Catalyst layer modeling

Many of the HT-PEMFC models have limited use and fail to show the real effect of system variables on performance. The failure of the reported models to predict the mass transport limitations under air operation and therefore over estimating cell performance, particularly at high current densities, was caused by the assumption that mass transport solely occurred through the porous media. In reality, an electrolyte (PBI/Acid) thin film surrounding the catalyst particles is present and mass transport through this phase should be considered. In this film, reactants have to dissolve in the electrolyte media and diffuse through it to reach the catalytic sites (Siegel et al., 2010).

The PEM fuel cell catalyst layer can be modeled through different approaches; there are two principal approaches, namely, macroscopic models that consider the catalyst layer as a whole, and microscopic models that consider the transport phenomena at the pore level. The macroscopic model can further be classified into three categories.

Macroscopic models (Rao et al., 2007; Srinivasrao et al., 2010)

- Homogeneous (porous/non-porous)
- Film Model
- Agglomerate models
 - The flooded agglomerate model
 - Cylindrical agglomerate model
 - Spherical agglomerate model

Oxygen permeability through the thin electrolyte film varies based on the temperature, the current density and on the equilibrium vapour pressure of the product water above the thin film. Relatively thick catalyst layers with very low porosity have been used in attempts to compensate for not modeling the thin film explicitly and to try and match the experimental data (Cheddie and Munroe, 2006e; Mamlouk et al., 2011). Most models used a reaction order in the range of 0.5-2 and varied the transfer coefficient according to the doping level of the acid. A limited number of HT-PEMFC catalyst layer models are available in literature.

Mamlouk et al. (2011) developed a one-dimensional model of a PBI-membrane HT-PEMFC. This model considered mass transport through a thin film electrolyte covering the catalyst particles as well as through the porous media as shown in Figure 2.1a. The catalyst interface is represented by a macro-homogeneous model. The model also included the influence of the reformat gas (carbon monoxide, carbon dioxide, and methane) in terms of the effect on the anode polarization/kinetics behavior. It gave good predictions of the effect of oxygen and air pressures on cell behavior and also mass transport behavior within the cell. The model with reformat gas shows additional voltage losses associated with CO poisoning.

The most accepted model of the catalyst layer is the flooded agglomerate model. According to this model, carbon supported catalyst particles flood within the electrolyte and form agglomerates covered with a thin film of electrolyte (see Figure 2.1b). The catalyst layer

consists of macro-micro porous, interconnected, hydrophobic regions to allow the reactant gas to access surface of the agglomerate regions. The flooded agglomerate model is very successful in explaining oxygen diffusion in the hydrophobic pores and electrolyte thin films. The agglomerate model gives a better representation of the catalyst layer on the basis of the simulations and a structural study of the catalyst layer (Rao et al., 2007).

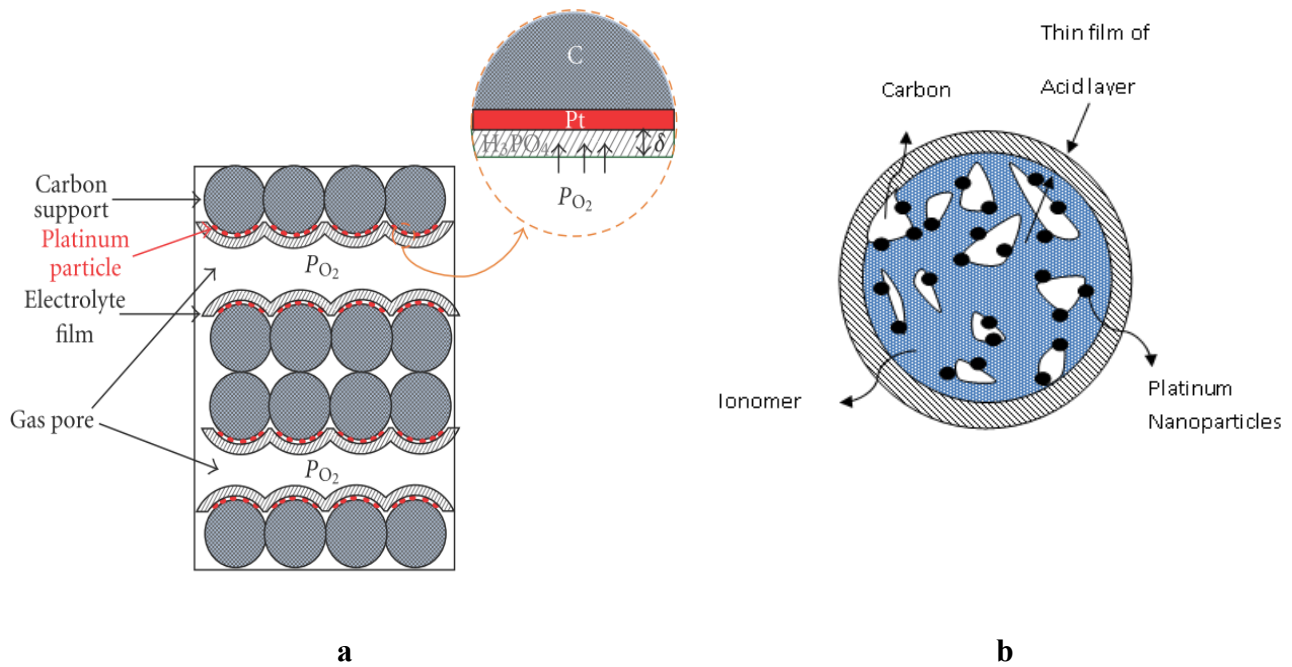


Figure 2.1: Schematic of catalyst layer using (a) the thin film model (Mamlouk et al., 2011) and (b) spherical agglomerate model.

Based on the earlier LT-PEMFC catalyst layer models, Siegel et al. (2010) developed a three-dimensional, steady-state, non-isothermal model for a phosphoric acid-doped Polybenzimidazole (PBI/H₃PO₄) sol-gel membrane of HT-PEMFC. Electrochemical reactions were modeled using an agglomerate approach and the effect of gas diffusivity and gas solubility were included. The conductivity of the membrane was modeled using the Arrhenius equation to describe the temperature dependence. It was observed that the Arrhenius approach was valid in a certain temperature range (150-160°C) and that the model overpredicted the PBI/H₃PO₄ sol-gel membrane conductivity at higher solid-phase temperatures.

2.1.2 Cell level modeling

All fuel cell models are parametric models in that they predict the output performance for various inputs, typically temperature, pressure and fuel composition. In most fuel cell models, the MEA is treated as a single layer and it is considered as a reactive boundary between the anode and the cathode. In other models, the MEA is treated as two separate catalyst layers, each layer is modeled in detail as discussed in Section 2.1.1. Most HT-PEMFC models treat the electrochemical reactions at electrodes using the Butler-Volmer or Tafel equation. Different types of HT-PEMFC models that are available in literature are discussed in detail in this section.

Cheddie and Munroe (2006a) developed a one-dimensional parametric model for HT-PEMFC considering the effect of temperature and porous media characteristics on polarization performance. This parametric model fails to predict the effect of mass transfer and could not explain limiting current observed under air operation. Later, they developed a one-dimensional, single phase, steady state analytical model to predict the polarization performance of a HT-PEMFC (Cheddie and Munroe, 2006c). The Tafel approximation was used to describe the electrode kinetics and polarization curve fitted using least-squares with a reaction order equal to 0.5. The model showed better fit with air than oxygen at low current densities but, it underestimates performance at high current densities. The same authors developed a two-dimensional model, which predicts the temperature and concentration profiles in the cell. This model accounts for rib effects and the variation of transport properties along the gas channels (Cheddie and Munroe, 2006d). Numerical results are compared with experimental results. This model does not take account of reactant gases dissolved in the catalyst layer which is assumed to be macro homogenous. The same authors later developed a three-dimensional model with the assumptions of transfer coefficient being equal to 2 and reaction order being equal to one. Once again the model failed to explain the observed difference between air and oxygen operation. The simulation data underestimated performance compared to the experimental data with oxygen and overestimated performance during air operation at high current densities (Cheddie and Munroe, 2006b). The same authors later developed a two-phase two-dimensional model by taking account of electrolyte conductivity and the solubility of hydrogen and oxygen as a function of temperature (Cheddie and Munroe, 2007). The model was also used to investigate the dependence of the fuel cell performance on membrane doping level, catalyst activity, and

transport properties of dissolved gases in the electrolytic membrane. This model concluded that only 1% of catalyst surface was utilized for the reaction and once again failed to predict the polarization curve in low current density regions.

Scott et al. (2007) proposed a one-dimensional model for HT-PEM PBI membrane based fuel cell. The electrode kinetics was described by the Butler-Volmer equation and the mass transport by the multicomponent Stefan Maxwell equations coupled with Darcy's law. It also considered the effect of partial pressure effect distribution on the cell voltage and the power density. The model had a good fit with the experimental data but failed to show limiting current behaviour under air operation.

Cheddie and Munroe(2008)developed a semi-analytical model based on the computational fluid dynamics (CFD) by using volumetric catalyst source terms as interfacial boundary condition on the MEA. These semi-analytical solutions matched very well with a full computational model in terms of the polarization results, hydrogen and oxygen concentration. These results showed that using analytical techniques did not compromise the accuracy of the model.

Hu et al. (2006) developed one dimensional degradation models to simulate the steady state polarization curves recorded at different times during aging tests. The model showed that the main reason for performance degradation was the decrease of electro chemical surface area (ESA) caused by catalyst agglomeration during high temperature sintering process. No obvious performance degradation was found on PBI-membrane. The models again failed to show any apparent mass transport limitations under air operation in limiting current region.

Scott et al. (2009) developed a simple semi-empirical zero-order model for estimating cell voltage and power performance as a function of current density. The model considered the influence of electrode kinetics using the Butler Volmer equation, over the complete voltage range, ohmic potential losses and the effect of mass transport through electrolyte films covering catalyst layers on kinetics and thermodynamics. The model failed to explain voltage curve at temperature above 120°C under the high current density region.

Sharamardina et al. (2010) developed a simple and quickly solvable pseudo steady-state isothermal model taking account of cross-over effects. The cross-over effects are only at low stoichiometric region near the limiting current density. It is unable to explain initial drop of cell voltage. Kulikovskiy et al. (2010) developed an analytical HT-PEMFC model and discussed the importance of basic kinetic and transport models. This model is limited to transportation losses of oxygen in the cathode catalyst layer and neglected the anode transportation losses and the anode overpotential.

Oono et al. (2010) investigated the relation between the HT-PEMFC operation temperature and cell durability in terms of the deterioration mechanism. They observed that the voltage increased by approximately 100 mV when the cell temperature was raised from 120 to 140°C. The thermodynamic open circuit voltage (OCV) decreases with increasing temperature, due to the increase of water partial pressure. When the cell temperature was subsequently raised from 140-200°C in increments of 10°C, the cell voltage increased at a rate of approximately 10 mV per 10°C. Higher cell temperatures were found to result in a higher cell voltage, but decreased cell life. The ohmic resistance drops slightly with increasing cell temperature and the mass transport resistance also decreases slightly as the cell temperature increases. The charge transfer resistance is reduced with increasing cell temperature and it is observed that the increase in catalyst activity, promoting electrode reactions lead to an increase in the cell voltage. The reduction in cell voltage of approximately 20 mV during the long-term tests was considered to be caused both by aggregation of the electrode catalyst particles in the early stage of power generation, in addition to the effects of crossover due to the depletion of phosphoric acid in the terminal stage, which occurs regardless of cell temperature. Further, Jalani et al. (2006) showed that the activation overpotential of the HT-PEMFC was reduced as cell temperature increased.

Sousa et al. (2010a) developed a two-dimensional isothermal model, in which the electrochemical reactions were described with the spherical agglomerate model. The model was validated with experimental data and it showed that the utilization of the catalyst particle was very low at high current densities. The results from the model and experimental results show that optimum performance fuel cell can be obtained when the volume fraction of phosphoric acid in the catalyst is in the range of 30–55%. The same authors used the finite element method to solve the non-isothermal model to study the influence of two different geometries (along the channel

direction and across the channel direction) on the performance. Predictions obtained by the channel geometry did not represent good performance trend, and therefore this geometry was not considered to be appropriate for fuel cells. The authors reported large temperature differences through the MEA which may happen if the catalyst layer was not efficiently used (Sousa et al., 2010b). They performed dynamic simulations and investigated the influence of the electrode double layer subjected to a step change in cell potential. A current overshoot could be found when a step change was performed and this overshoot was caused by the delayed change of local oxygen concentration behind the change in potential. The overshoot could be removed by increasing the double layer capacitance. The same model was modified to find the degradation of MEA over time and it was found that during the first period of 300 hr, the catalyst activity loss due to the change in mean particle/agglomerate size was the dominant effect compared to the phosphoric acid loss. The degradation mechanism showed very good agreement with the earlier study by Hu et al.(2006), in which a 500 hour aging test was performed.

Sousa et al. (2012) developed a 3-D isothermal model for an HT-PEMFC equipped with phosphoric acid doped PBI and tested it for different flow field topologies. The results proved that interdigitated flow field topology gives the highest power output. However, it was not suitable for the fuel cell system because hot points were generated due to heterogeneous current density distribution. In this study, a new geometry was suggested in order to homogenize the mass flux in the straight channels geometry with varying inlet and outlet manifold.

The influence of the CO poisoning at the anode of an HT-PEMFC was investigated by several researchers. The adsorption of CO on Pt is associated with high negative entropy, indicating that adsorption is disfavoured at high temperatures. Hydrogen adsorption on the platinum surface is less exothermic than CO and it requires two adsorption sites. An increase in the cell temperature leads to a beneficial shift towards higher H₂ coverage at the expense of CO coverage. CO tolerance is dramatically enhanced, from 10 to 20 ppm at 80°C to 1000 ppm at 130°C, and up to 30,000 ppm at 200°C (Mamlouk et al., 2011; Zhang et al., 2007; Bergmann et al., 2009). Recent HT-PEMFC catalyst and membranes have CO tolerance of up to 50,000 ppm and it is possible to use directly hydrogen produced from a simple reformer.

Bergmann et al. (2010) developed a dynamic, non-isothermal 2-D model of a PBI-based HT-PEMFC the results of which were validated by experimental data of in-house measurements. The anode catalyst layer is taken as a thin film in between the membrane and GDL. The temperature dependency of the fuel cell performance and CO poisoning of the anode is analysed with polarisation curves for different CO concentrations as well as the CO pulses. The analysis showed nonlinear behavior of the fuel cell performance under influence of CO.

Peng and Lee (2006) presented a single-phase, 3-D, non-isothermal numerical model which was implemented into a CFD code. The current density increases with increasing operating temperature and the maximum temperature was located on the catalyst layer. The model shows that the width and distribution of gas channel and the current collector land are key optimization parameters for fuel cell operation. This model was extended by Peng et al. (2008) to describe the transient behavior of the current density of the cell. The prediction shows transients in cell current density which overshoots (undershoots) the stabilized state value when cell voltage is abruptly decreased (increased). The peak of overshoot is related with cathode air stoichiometric instead of hydrogen stoichiometric. The maximum temperature is located in the cathode catalyst layer and both the fuel cell average temperature and the temperature deviation are increased with increasing current load.

Jaio and lee (2010) developed a 3-D, non-isothermal model to investigate the effects of operating temperature, phosphoric acid doping level of the PBI membrane, inlet relative humidity (RH), stoichiometry ratios of the feed gases, operating pressure and air/oxygen on the cell performance. The model shows that increasing both the operating temperature and the phosphoric acid doping level are favourable for improving the cell performance. Humidifying the feed gases has negligible improvement on the cell performance. Using oxygen instead of air has significant improvements on the cell performance and increasing the stoichiometric ratios only helps prevent concentration losses at high current densities.

Ubong et al. (2009) developed a non-isothermal, 3-D model and validated it with a single cell with a triple serpentine channel flow field. The results show that there is no drastic decrease in the cell voltage at high current density due to mass transfer limitations and it was also concluded that reactants need not be humidified.

Lobato et al. (2010a) developed a 3-D, full cell geometry model with a cell active area of 50 cm^2 . Using this CFD model, they show that the current density distribution is directly linked to the way reactants are spread over the electrode surface. The model predicts that parallel flow channels present a significantly lower performance serpentine and pin-type flow channels are found to perform very similarly, although slightly higher limiting current densities are predicted when using serpentine geometry.

Seigel et al. (2011) developed a 3-D, isothermal model, where the electrode chemical kinetics are modeled using the agglomerate approach and membrane conductivity by Arrhenius equations and validated it with a six-channel cell. Good agreement with experimental results was found in the temperature range $150\text{-}160^\circ\text{C}$. An artificial neural network approach was successfully applied to predict the polarization curve for HT-PEMFC (Lobato et al., 2010b). Tortuosity was used as model parameter to describe the influence of Polytetrafluoroethylene (PTFE) content in the GDL.

Kulikovsky et al. (2010) developed an analytical model which was based on a two step procedure to evaluate parameters like exchange current density, Tafel slope, and cell resistance from two sets of polarization curves for a HT-PEMFC and validated it with experimental data. Shamardina et al. (2010) developed an analytical model, 2-D pseudo, steady-state and isothermal model which accounts for the crossover of reactant gases through the membrane. The model results show that the crossover effect has a considerable influence only at low temperature. The same authors developed a model which takes into account transport losses in the cathode catalyst layer (CCL) (Shamardina et al., 2012). This model has a more accurate value of the exchange current density and provides useful data on the porosity and the effective oxygen diffusivity in the CCL. Most of the above models have in common a set of fundamental parameters which can be compared in order to check consistency.

2.1.3 Stack level modeling

The HT-PEMFC stack contains multiple cells connected in series to develop the required voltage. It consists of repeating units of fuel cells and cooling plates. The number of cooling plates in a stack varies depending on the coolant and as well as flow field. Stack models that are

available in the literature are on a higher abstraction level and they are mainly as one component of a complete fuel cell system (Stolten, 2012).

Several approaches can be used to construct a fuel cell stack model depending on the modeling requirement.

- The stack is described as zero-dimensional model without any spatial resolution.
- Part of stack is modeled.
- The single cells are modeled explicitly.

In the first type of approach, the information of the full stack is described as the stack is described as a zero-dimensional model without any spatial resolution. The model contains little information about the cell level and it is mainly focused on the overall performance of the stack. Korsgaard et al. (2006a, 2006b) developed a semi-empirical stack model and validated it with experimental data. The cell voltage was calculated as a function of temperature, current density and air stoichiometry. The CO content in the anode was varied from 0-5%, with CO₂ content ranging from 25-20% and remaining H₂ content and temperatures ranging from 160-200°C. It showed excellent agreement with the experimental data and the simplicity and accuracy of the model makes it ideal for system modeling and real-time applications. The experimental results of pure hydrogen data were used as test data to estimate the parameters by using a least squares optimization algorithm. Korsgaard et al. (2008a, 2008b) successfully applied this type of modeling approach based on their earlier models (Korsgaard et al., 2006a, 2006b) to find static system integration as well as dynamical control strategies of fuel cell stack based on PBI membranes. The HT-PEMFC stack consisted of combined heat and power (CHP) systems which was integrated with a steam-reforming reactor, burner, heat reservoir and other auxiliary equipments. Chrenko et al. (2010) developed a static and dynamic model for a diesel fuel processor fuel cell stack. The model was validated with experimental data.

Ahluwalia et al. (2003) developed a HT-PEMFC stack model which was based on the performance of a gasoline reformed, LT-PEMFC stack. A parametric study was conducted on the LT-PEMFC stack operating at a temperature of 80°C and the performance were compared

with HT-PEMFC stack operating in the temperature range of 150-200°C. The model concluded that the HT-PEMFC stacks have higher efficiency compared to LT-PEMFC stacks.

In the second approach, part of the stack constitutes the computational domain. This type of model reduces the overall computational domain to a small unit and substantially reduces the simulation time. The information of all cells is averaged, based on the computational domain and the overall stack information can be obtained by multiplying these individual cells or model domain with a number of repeating units. Most of models that are available in the literature have a repeat unit of one cell and one channel (Tao et al., 2006). This method was successfully applied to describe a 20 cell LT-PEMFC stack model to find the effect of reactant flows, two-phase effects and temperature distribution on the stack performance (Park and Choe, 2008). The volume averaging method was applied for SOFC stacks in which the effective cell was modeled in 2D (Roos et al., 2003).

Andreasen et al. (2009) developed an impedance HT-PEMFC stack model which is able to predict the stack impedance at different temperature profiles of the stack. Simple equivalent circuit models for each single fuel cell can be used to predict the HT-PEMFC stack impedance at different temperatures. The typical output of an EIS measurement on a fuel cell is a Nyquist plot, which shows the imaginary and real parts of the impedance of the measured system. The full stack impedance depends on the impedance of each of the single cells of the stack. Designing of such models, which are able to predict fuel cell behavior in steady-state as well as in dynamic operation, has an advantage in controlling of fuel cell systems. This model is very useful in fuel cell system performance prediction, where different electronic components introduce current harmonics.

In the third approach, single cells are modeled explicitly and they are coupled (e.g. by the stack manifolds for flow) to yield the full behavior of the stack. The types of models require more computational time when the full geometry is modeled. This approach is then successfully applied and demonstrated in a short stack of LT-PEMFCs (Chang et al., 2006; Cheng and Lin, 2009; Hawkes et al., 2009; Verda and Sciacovelli, 2011). Recently Kvesic et al. (2012a) reported a short stack model using an averaged volume approach.

2.2 Thermal management PEM fuel cell stack

The cooling of the fuel cell stack can be achieved through a number ways including:

- passive cooling with cooling fins and high thermal conductivity heat spreaders,
- active cooling with air or liquid coolants,
- evaporative cooling or cooling with phase change liquids and
- cooling with a separate air flow.

A summary of some of the important cooling strategies for PEMFC stacks (Zhang and Kandlikar, 2012) is given in Table 2.1. Passive cooling methods in which heat is removed using heat spreaders are also known as edge cooling methods. They have the limitation that they cannot be used alone, i.e., without using an air blower, when the stack size is greater than 50 W because of the limited surface area available within the cell and the low temperature difference between the PEMFC and the ambient. As a result, natural convection is not effective in maintaining a sufficiently uniform cell temperature. This can however be achieved by using forced air ventilation over the stack (Larminie and Dicks, 2000).

Active cooling methods, in which the coolant fluid (either air or water) is pumped through cooling passages within the stack, are capable of greater heat removal from the stack. LT-PEMFCs and flow field configurations have been developed to minimize pressure drop and to maximize temperature uniformity within the stack (Choi et al., 2008; Yu et al., 2009; Asghari et al., 2011; Baek et al., 2011). It is also possible to remove the heat through evaporation and condensation of water inside the LT-PEMFC stack; in such cases, the liquid saturation along the length of the coolant path influences the cell temperature gradient (Ju et al., 2008). The details of all these model are discussed in the following sections.

2.2.1 LT-PEMFC cooling techniques

Generally PEMFCs are cooled by air or water or heat spreaders or antifreeze or other types of coolant that circulates through dedicated cooling plates or bipolar plates (Faghri and Guo, 2005; Kandlikar and Lu, 2009; Zhang and Kandlikar, 2012). A nearly uniform temperature distribution can be obtained by using a large flow rate of coolant which circulates through cooling plate.

However, having a separate coolant adds to the complexity of the system, increases the operational cost and the high parasitic power consumption decreases the overall efficiency of the fuel cell (Kandlikar and Lu, 2009).

Zhang et al. (2004) developed a lumped thermal model and studied the effect of operating parameters (stack power output, cooling water flow rate, air flow rate, and environmental temperature) on the system thermal performance of an LT-PEMFC stack for transportation applications. The thermal model was validated with experimental results and predicted thus that the thermal efficiency increases with air flow rate, decreases with an increase in water flow rate, and decreases slightly with environmental temperature. This model is able to generate transient information such as stack cooling water outlet temperature as a function of time, under perturbation conditions (such as the stack initial start-up, shut-down, change in current density a large step in power output and the fan start-up). A similar model was developed by Yu and Jung (2005) in order to estimate parasitic losses with respect to the operating temperature of the LT-PEMFC stack for transportation applications. The model also included the stack physical conditions (like channel geometry, heat transfer coefficients, and operating current) and the model could provide information regarding the reaction products (i.e., water and heat), stack power, stack temperature, and system efficiency, thereby assisting the designer in achieving the best thermal and water management (Yu and Jung, 2005). Koh et al. (2005) investigated the influence of the current density on the average cell temperature for an air-cooled stack of a Nafion membrane-based fuel cell and demonstrated that air cooling by natural convection was not sufficiently effective in maintaining a uniform cell temperature. They concluded that the stack design variables such as active cell area and number of cells also have significant influence on self-controlled temperature; the design of stack size is important and at least one of the stack dimensions (area or number of cells) should be small for self-heating to be effective. The range of allowable current load increases with lower ohmic resistance materials, high current load applications of self-heating stack can be made possible by increasing the heat loss coefficient to the range of forced convection and it has a strong effect on self-heating effectiveness.

Shon et al. (2006) studied the behavior of an air-cooled LT-PEMFC for portable applications. The stack power is improved for 66% relative humidity compared with air cooling.

Table 2.1 Summary of some of the important cooling strategies for PEMFC stacks(Zhang and Kandlikar, 2012).

Cooling strategy	Techniques	Advantages	Disadvantages/Challenges
Heat Spreaders/Edge cooling	Using highly thermal conductive material as heat spreaders	-Simple system -No internal coolant -Small parasitic power -No leakage problems	-Limited heat transfer length -Non-availability of cost-effective material with very high thermal conductivity and good mechanical properties
	Using heat pipes as heat spreaders	-Simple system -Small parasitic power -Very high thermal conductivity	-Development of heat pipes with small thickness and low weight -Integration of heat pipes with bipolar plates
Cooling with separate air flow	Separate air channels for cooling	-Simple system -Small parasitic power	-Trade-off between cooling performance and parasitic power
Liquid cooling	Channels integrated in Bipolar plate (de-mineralized water/antifreeze coolant)	-Strong cooling capability -Flexible control of cooling capability	-Radiator size -Coolant degradation -Large parasitic power
Phase change cooling	Evaporative cooling(direct water injection, porous water transport plates, wicking lands/channels)	-Simultaneous cooling and internal humidification -Simplified system	-Dynamic control of water evaporation rate -Thermal mass of liquid water on cold startup
	Cooling through boiling	-Elimination of coolant pump -Simplified system	-Development of suitable working media -Two-phase flow instability

Results showed that the parasitic load associated with the forced axial cooling fan consumed less than 2% of the overall power output at the room temperature.

Adzakpa et al. (2008) developed a transient air cooling thermal modeling of an LT-PEMFC and investigated the effect of the non-uniformity of the cell temperature on the efficiency of the cell. The gas humidity was shown to have a great impact on membrane resistance, resulting in higher heat generation in the cell. The results also show that temperature non-uniformity in the stack increases with the load current and may be due to non-uniform cooling. Ju and Wang (2008) developed a numerical model for the evaporation and condensation of water inside the LT-PEMFCs and studied the influence of the cell temperature gradient, liquid saturation along the length of the coolant path. Choi et al. (2008) developed a numerical model in order to investigate the effect of parallel and serpentine flow field geometry on the maximum surface temperature and uniformity of temperature distribution in the LT-PEMFC stack. Yu et al. (2009) developed a model and studied the effect of cooling channel designs (several multi-pass serpentine flow field) on the performance and heat management. Baek et al. (2011) investigated different multi-pass serpentine flow field designs with large scale in order to achieve uniformity of temperature distribution in the LT-PEMFC stack. The results demonstrated that multi-pass serpentine flow fields (MPSFF) lead to better cooling performance and temperature uniformity compared with a conventional serpentine flow field. The best cooling performance LT-PEMFC is obtained with a better design MPSFF, which shows a 40–60% reduction in the uniformity indices compared with the conventional serpentine flow field (Yu et al., 2009). Matian et al. (2008) developed a simple thermal model to investigate the effect of bipolar plate material of construction and external forced convection on the LT-PEMFC stack temperature and validated their results with a fuel cell analog composed of an electrically heated plate. Asghari et al. (2011) developed a numerical model for a parallel serpentine flow field design in order to achieve minimum pressure drop and maximum temperature uniformity within the stack. The LT-PEMFC stack model is validated and the results are verified with experimentally measured temperature profiles along the vertical and horizontal edges of the bipolar plates. From this model, it is concluded that the inlet and outlet manifolds of reactant gases have an influence on the temperature distribution within the bipolar plates. Cozzolino et al. (2011) studied the behaviour of a water-cooled LT-PEMFC stack suitable for micro-

cogeneration systems application. Experiments were conducted in order to characterize the thermal and the electrical behavior of water-cooled PEMFC stacks under different gas feeding (pure/diluted hydrogen, air/oxygen).

2.2.2 HT-PEMFC cooling techniques

Some studies have been reported for the cooling of HT-PEMFCs. Andreasen et al. (2008a) developed a dynamic stack model for a hybrid electrical vehicle including HT-PEMFC and lead-acid batteries using air as coolant. Pre-heating of the fuel cell stack with electrical resistors was investigated and found to be an unrealistic approach for automotive applications. A simple and reliable approach to temperature management in the stack was using the un-pressurized, cathode air stream as coolant. The same authors later developed a model for heating strategies for a HT-PEMFC stack and concluded that the startup time can be reduced by sending pre-heated cathode air (Andreasen et al., 2008b). Direct electrical heating of the fuel cell can take up to 50 minutes during the start-up of the stack which can be reduced by sending pre-heated air to the cathode. The start-up time can be reduced from 1 hr to 6 min by introducing heating element with high current density. During start-up, sudden expansion of layers takes place so, better thermal contact with adhesive materials are needed with fast thermal expansion.

The experimental work suggested that the strategy of using preheated air (160°C) for heating a HT-PEMFC is a fast and efficient way of reaching the desired operating temperatures. Air heating strategy also gave a homogenous heat distribution in the entire stack volume, compared to the direct electrical heating strategies and the minimum heating time also reduces heat losses from stack to the surroundings. Other heating methods, such as heating elements embedded within each bipolar plate creates a much more uniform and efficient heating (Andreasen et al., 2008b).

Scholta et al. (2008) developed a 5-cell HT-PEMFC stack which was cooled using air or a liquid coolant. It was concluded that by using external cooling, it is possible to avoid two constraints. First, there is no liquid water in the cell active area avoiding sealing problems with respect to the electrodes. Second, the external positioning allows high temperature gradient between heat removal zone and the cell active area. This allows the cell operating temperature to be near to the appropriate reformate conversion temperature. It is further concluded that separate

design of channels in needed for water and air. The same authors developed another model for a 10-cell HT-PEMFC stack which was cooled using heat pipes (Scholta et al, 2009). In both cases, they did not consider the electrochemical reactions and assumed a constant heat source term. They reported that the temperature variation from the center to the edge was around 56°C for a cell operating temperature of 160°C and an inlet cooling oil temperature of 100°C. The experimental results of external cooling designs showed that the temperature gradients within the cell active area are below 15 K under typical operating conditions.

Song et al. (2011) developed a prototype model of a natural circulation-driven water cooling system for an HT-PEMFC stack operating at a exit temperature of 150°C. In this concept, water was used as the coolant and the buoyant force caused by the density difference between vapour and liquid was utilized to circulate the coolant between the stack and the cooling device. The phase-change latent heat of water acts as a driving force to circulate the coolant in the stack as well as in a heat exchanger. The coolant water circulated through the stack goes through the cooling device where the excess heat is transferred to a secondary cooling stream. The stack temperatures were found to be sensitive to the secondary coolant and it needed additional control attention. The results showed that the pump less cooling method provides more uniform temperature distribution within the stack, regardless of the direction of coolant flow.

None of the above HT-PEMFC stack models consider the effect of local current density on the variation of the cell temperature and the performance of the stack. Kvesic et al. (2012a) developed a multi-scale, 3-D model of an HT-PEMFC stack containing one cooling channel in each bipolar plate. The stack consisted of 5 cells with cooling arrangement system for each cell. In this model, the stack manifolds were considered separately from the body of the stack and a porous medium approach was used for the resolution of cell-level phenomena. The porous medium included the anode and the cathode flow fields, the land area of the channel and the gas diffusion layer (GDL); all these were combined to form a homogeneous porous domain. The membrane-electrode assembly (MEA) consisting of the anode catalyst layer, the membrane and the cathode layer, was treated as a separate volume in which the catalyst layers were modeled as two-dimensional planes. The anode and the cathode side volumes of the MEA were coupled through adjacent mesh sites and source and sink terms were defined by a Tafel equation for the

cell. The model was validated with experimental data of local temperature in the stack. The measured temperatures were within the experimental error and the model predicted higher current density near the inlet than near the outlet. The drawback of these kinds of models (effective porous volume approach) is that validation is very important because of the severe simplification of the mass transport. While their earlier work (Kvesic et al., 2012a) considered the case of a hydrogen-fed PEM fuel cell, their later work (Kvesic et al., 2012b) considered the case of a reformat gas using their earlier work (Kvesic et al., 2012a; Luke et al., 2012) to characterize the corresponding electrochemical performance of the cell. Their studies showed that, if the reactants and the coolant were preheated, then the cell temperature variations would be in the range of 3 to 6°C within the cell for a hydrogen-fed case and about 9 to 10°C for a reformat gas case. A significant variation of the local current density, in the range of 0.5 to 0.8 A/cm² for an average cell current density of 0.6 A/cm², was predicted and this was found to be in agreement with their own experimental results. In a recent paper, Supra et al. (2013) have reported measurement of cell temperatures in a 1 kWe, liquid-cooled HT-PEMFC stack with one cooling plate for every three cells. The fuel for the cell was reformat gas and the liquid coolant entered the stack at 433 K. The measured temperature variations in the cells in between the cooling plates showed a temperature variation of the order of 6 to 8 K with a maximum variation of 8.3 K. Data of local cell voltage obtained under constant current mode of operation showed that the voltage varied by about 5 to 10% and that the variation correlated well with that of the cell temperature. These experimental data are thus a confirmation of the effect of liquid coolant on the temperature variation within the stack and of the resulting effect on the electrochemistry of the cell.

2.3 Objectives and scope of the present work

There have thus been a number of thermal management studies for LT and HT-PEMFCs using numerical models based on CFD simulations. While air cooling has been studied, this has been limited to external (forced convective) cooling only. Plate cooling has been studied but with an external coolant loop using a liquid.

Against this background, the objective of the present work is to systematically study the thermal management of a HT-PEMFC stack and quantify the effect of various stack cooling

strategies on the overall performance of the stack using a computational fluid dynamics (CFD) model. The stack model is developed by coupling the electrochemistry with the flow and temperature fields to capture local current density a function of local temperature within the cathode catalyst layer.

Most of the heat is generated in the cathode catalyst layer of a HT-PEMFC. This heat generation is a nonlinear function of the local current generation, which in turn is highly dependent on the temperature and concentrations of the active chemical species. This two-way coupling and the wide range of length scales in a fuel cell make it computationally prohibitive to solve the fully coupled multiphysics in a HT-PEMFC. In this work, we use empirical equations derived from experimental data to capture local current density variations with respect to temperature and assume that the mass transfer and electrochemical losses are described sufficiently by these functions (Korsgaard et al., 2006a, 2006b). This allows us to avoid solving for the concentration fields in the channels and electrodes, and the electrical potential fields in the electrodes and electrolyte. The empirical functions are coupled to the solution of the fluid flow and heat transfer occurring inside a fuel cell stack using a commercial CFD program.

The thermal management techniques investigated in this work are: i) integrated cathode air cooling, ii) external air flow over the hot stack, iii) coupling a H₂ storage system to the cathode air cooling system, and iv) the use of liquid coolants in a separate cooling circuit. Details of the calculations and the results obtained are discussed in the following chapters.

CHAPTER-3

PROBLEM FORMULATION AND MODEL DESCRIPTION

3.1 Problem formulation

The heat generation rate in HT-PEMFC is high at high current densities where it can exceed the total electrical power output. At the same, the cell temperature has to be maintained as uniform as possible throughout the stack. This imposes challenges in the cooling of stack, especially in auto mobile applications which require high current density in order to maintain a high power density. The temperature within in the catalyst varies spatially and it strongly depends on the local current density and the amount of local heat generated. Non-uniform heat generation leads to generation of local hot spots within the catalyst layer of cell and may leads to local accelerated degradation. Proper thermal management is therefore needed in order to prevent the formation of local hotspots and to maintain the high performance and durability of the fuel cell. The cooling of fuel cell stack adds additional power required during the fuel cell operation and it affects the overall performance of the system.

3.1.1 Statement of the thermal management problem

The objective of the present work is to determine the temperature distribution in the various layers comprising the cell and the stack and optimize cooling system such that the temperature anywhere in the stack is kept below the maximum limit while maintaining as high a temperature as possible throughout. We determine the optimum cooling system for the HT-PEMFC stack by studying cooling strategies. In order to investigate the impact of these strategies and associated parameters, as well as to assess the advantages or penalties associated with each measure, a number of CFD simulations have been carried out.

The following strategies/parameters were studied in this work:

- Coolant medium: air, water or heat transfer oil (liquid coolant)
- Cathode air stoichiometric factor: 1, 2 or 3
- Operating voltage: 0.5 or 0.6 V
- Coupling integrated cathode air cooling system with a H₂ storage tank

- Number of coolants plates: one for every four or six cells
- Cooling plate material: copper, aluminum or graphite
- Coolant inlet temperature: 300-450 K
- Flow field designs: cooling plate and cathode flow field
- Stack size: 1-100 kWe

All the above parameters are studied for a 1 kWe HT-PEMFC stack with a parallel flow configuration in the cooling plate flow field as well as in the bipolar plate. Further simulations have been carried out for larger stack sizes with different flow field configurations in the cooling plate and bipolar plate in order to optimize the thermal management system and increase the overall performance of the stack. These are discussed in Chapter 5.

3.1.2 Description of the HT-PEMFC stack

The HT-PEMFC stack studied in the present work is based on a cell with a solid electrolyte made of the polybenzimidazole (PBI) membrane doped with phosphoric acid. An HT-PEMFC stack includes serially connected single unit cells to produce the designed output power as shown schematically in Figure 3.1. Each cell consists of a membrane for ion conduction, two catalyst layers for electrochemical reactions, two gas diffusion layers and two bipolar plates for the electron conduction and flow distribution. The gas diffusion layers and the bipolar plates are the same as those for an LT-PEMFC. The cell dimensions and thermal properties are given in Table 3.1. Typical platinum loadings for HT-PEMFCs are in the range of 0.2-0.4 mg/cm² which are slightly higher than these used for LT-PEMFCs. The HT-PEMFC membrane is entirely different from the LT-PEMFC membrane, because the LT-PEMFC generally feature a Nafion[®] membrane which is not suitable for temperature above 80°C. The HT-PEMFC membrane is made of PBI which has high proton conductivity even without humidification (it may depend on the acid doping level in the membrane) (Bose et al., 2011).

In the present study, we consider possible application in the transport sector. Two-wheelers like scooters require power in the range of 0.4-1 kWe while cars require 50-100 kWe.

Table 0.1: The cell dimensions and thermal properties of an HT-PEMFC stack.

Fuel cell layers		
Anode /cathode GDL thickness	2.0×10^{-4}	m
Anode catalyst layer thickness	1.3×10^{-5}	m
Membrane layer thickness	4.0×10^{-5}	m
Cathode catalyst layer thickness	1.3×10^{-5}	m
Monopolar plate thickness	1.5×10^{-3}	m
Bipolar plate thickness	3.0×10^{-3}	m
Cooling plate thickness	2.0×10^{-3}	m
Thermal conductivities of fuel cell layers		
Anode/cathode GDL	1.70	W/m K
Membrane	0.95	W/m K
Anode/cathode catalyst	0.30	W/m K
Bipolar/monopolar plate	20.0	W/m K
Cooling plate	20.0	W/m K
Bipolar plate channel dimensions		
Channel depth	1×10^{-3}	m
Channel width	1×10^{-3}	m
Channel and rib width	2×10^{-3}	m
Channel length	0.1	m
Cooling plate channel dimensions		
Channel depth	1×10^{-3}	m
Channel width	1×10^{-3}	m
Channel length	0.1	m

3.1.3 Estimation of the thermal load

The hydrogen gas ionizes at the anode catalyst layer and releases hydrogen ions and electrons. The electrons flow from the anode to the cathode by an external circuit while the hydrogen ions flow through the membrane. At the cathode catalyst layer, oxygen reacts with the electrons and hydrogen ions and produces water, electrical energy and thermal energy. Most of the heat

produced in the cell is generated in the cathode catalyst layer due to asymmetry of the entropy change and the overpotential on the cathode electrode (Ju et al., 2005a, 2005b). Ohmic heating is

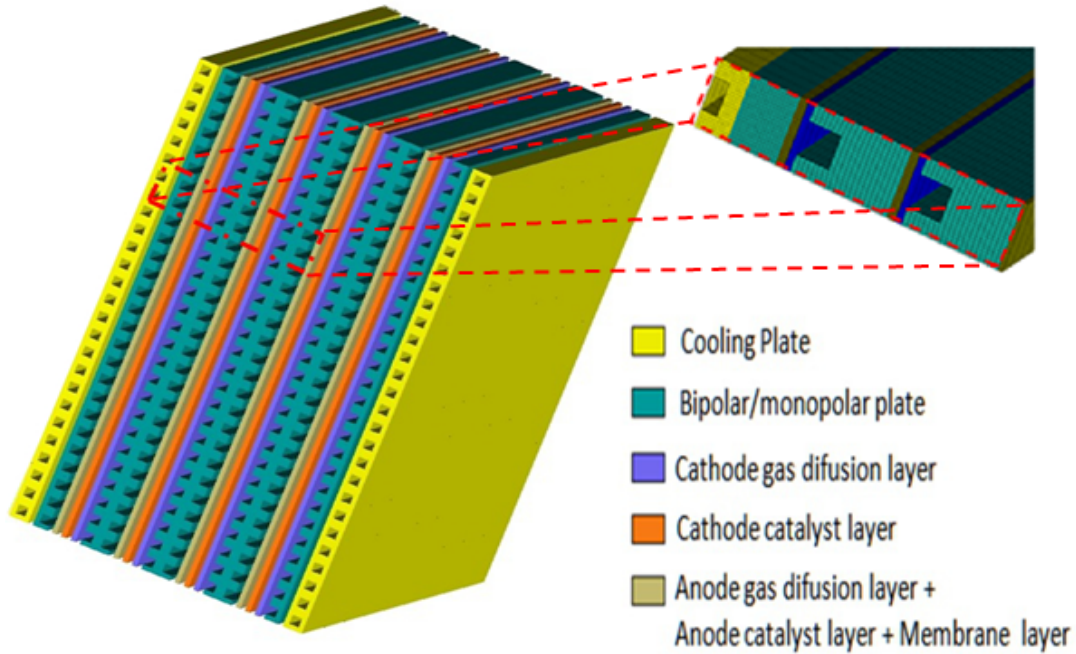


Figure 0.1: Schematic diagram of the HT-PEMFC stack with one cooling plate for every four cells. The figure on the right shows the portion modeled in the CFD simulations as Case A.

attributable to proton and electron conduction through the membrane and the GDL etc., it also contributes to the heat generation, although to a smaller extent. Since the anode overpotential is small, its contribution can be neglected (Shamardina et al., 2010). There are sources of heat removal from the cell. Firstly, due to the high operating temperature, all water produced at the cathode will be vapourized; the contribution of the latent heat of vapourization must be accounted for in estimating the heat load. Similarly, the heating up of hydrogen in the anode flow field from its feed temperature to the cell operating temperature also requires heat (preliminary calculations show that 3%-7% of the total heat generated goes into heating hydrogen for fuel stoichiometric ratio varying from 1-3). The same is true also for the heating up of the cathode air. Finally, heat may be lost by natural (or forced) convection and radiation to the surroundings. In the present study, we do not model the fuel side explicitly and lump the anode layers along with the membrane in the geometry used for the simulations (Figure 3.1). Thus, we neglect the

contribution of the (relatively minor) heat generation due to the anode activation and concentration overpotentials, and heat removal due to the heating up of the fuel. We take specific account of all the other factors in estimating the thermal load on the heat removal system. Total heat released from each cell in the stack can be estimated as follows.

The cell voltage variation can be expressed by the equation (Korsgaard et al. 2006a; Korsgaard et al. 2006 b):

$$V_{cell} = \frac{V_0 - RT_{cell}}{4\alpha_c F} \ln \left(\frac{i_{cell} + i_0}{i_0} \right) - \frac{R_{ohmic} i_{cell} - R_{con} i_{cell}}{\lambda - 1} \quad (3.1)$$

where α_c is the cathode transfer coefficient, i_0 is the exchange current density, R_{ohmic} and R_{con} are the ohmic and concentration losses (expressed as equivalent resistances) and λ is the stoichiometric factor. Korsgaard et al. (2006a) expressed these as linear functions of temperature:

$$\alpha_c = a_0 T_{cell} + b_0 \quad (3.2)$$

$$R_{ohmic} = a_1 T_{cell} + b_1 \quad (3.3)$$

$$R_{con} = a_2 T_{cell} + b_2 \quad (3.4)$$

$$i_0 = a_3 e^{-b_3 T_{cell}} \quad (3.5)$$

They obtained the constants using their own experimental data from a PBI-membrane-based HT-PEMFC; these are given in Table 0.2.

In order to reduce the complexity of the problem involving fluid flow, heat transfer, electrochemical reaction and ionic and electronic transfer, some simplifications have been made to make the problem more tractable:

The electrochemistry and the ionic and electronic transport have been treated algebraically using an empirically-derived polarization curve (validated with experimental data) appropriate for the HT-PEMFC given by equation 3.1. Therefore, the potential field is not calculated explicitly.

The coupling of the electrochemistry with the species concentrations is simplified by using mean concentrations of the species in the polarization curve. The composition and flow rate on the air side are assumed constant. This is a reasonable assumption as air is mostly nitrogen and the air side flow-rate is usually well above the required stoichiometric flow-rate. The calculation of the velocity field in the cathode flow fields thus reduces to one of calculating it for a gaseous mixture of fixed concentration. As the fuel side kinetic and concentration losses are negligible, the fuel side flow is not modeled.

Table 0.2: Values used for varying current density with temperature (Korsgaard et al., 2006a).

Charge transfer constant, a_0	2.761×10^{-3}	1/K
Charge transfer constant, b_0	-0.9453	-
Ohmic loss constant, a_1	-1.667×10^{-4}	Ω / K
Ohmic loss constant, b_1	0.2289	Ω
Diffusion limitation constant, a_2	-1.667×10^{-4}	Ω / K
Diffusion limitation constant, b_2	0.4306	Ω
Limiting current constant, a_3	33.3×10^3	A
Limiting current constant, b_3	-0.04368	-
Open circuit voltage, V_0	0.95	V

The coupling between the temperature field and the current density is enabled through the empirical polarization curve which relates the current density (i_{cell}), the potential (V_{cell}) and the temperature (T_{cell}). For a cathode side stoichiometric factor of 3 and an anode side stoichiometric factor of 2 (75% H_2 , 25% CO_2), the empirical curves (Korsgaard et al., 2006a, 2006b).have been used to obtain the following explicit expressions for the current density in terms of the temperature:

$$i_{cell} = 1.377 \times 10^{-7} T_{cell}^3 - 0.0001767 T_{cell}^2 + 0.078555 T_{cell} - 11.77 \text{ for } V_{cell} = 0.6 \text{ V} \quad (3.6)$$

$$i_{cell} = 4.75 \times 10^{-7} T_{cell}^3 - 0.0006153 T_{cell}^2 + 0.2738 T_{cell} - 41.22 \text{ for } V_{cell} = 0.5 \text{ V} \quad (3.7)$$

where T_{cell} is in K and i_{cell} is in A/cm^2

This is used to calculate the overpotential term and hence the heat generation term (as explained below) in the energy conservation equation in the cathode catalyst layer.

As far as the heat transfer is concerned, the model has an exact treatment to calculate the temperature distribution in each layer of the cell and the stack. In all the solid regions except the cathode catalyst layers, the heat conduction is calculated without a heat generation term. In the cathode catalyst layers, a local heat generation term is calculated in each control volume as discussed below.

The heat generation rate for each cell in the stack at any working temperature can be determined using thermodynamic relations. The total amount of heat released, Q_{cell} , from the each cell is the sum of the reversible heat generation, Q_{rev} , and the irreversible heat generation, Q_{irrev} (Ju et al., 2005). Thus,

$$Q_{\text{cell}} = Q_{\text{rev}} + Q_{\text{irrev}} \quad (3.8)$$

The current produced by the cell, I_{cell} , is given by

$$I_{\text{cell}} = i_{\text{cell}} A_{\text{cell}} \quad (3.9)$$

where i_{cell} is the cell current density and A_{cell} is the total active area of a single cell (all cells are assumed to be operating identically). The stack voltage, V_{st} , is given by

$$V_{\text{st}} = V_{\text{cell}} N_{\text{cell}} \quad (3.10)$$

where V_{cell} is the cell operating voltage and N_{cell} is the number of cells connected in series, which is determined from the power requirement for the stack, given by,

$$P_{\text{st}} = I_{\text{st}} V_{\text{st}} \quad (3.11)$$

The reversible heat release can be written as a function of the cell operating temperature (T_{cell}), the cell current (I_{cell}) and the entropy change of the overall reaction (ΔS_T):

$$Q_{\text{rev}} = (-T_{\text{cell}} \Delta S_T) \frac{I_{\text{cell}}}{nF} \quad (3.12)$$

where F is Faraday's constant, n is the number of electrons transferred, ΔS_T in J/K and T_{cell} in K.

The irreversible heat release can be evaluated as,

$$Q_{irrev} = \left(-\frac{\Delta G_T}{nF} - V_{cell} \right) I_{cell} \quad (3.13)$$

where ΔG_T is the Gibbs free energy change for the reaction. In the evaluation of ΔG_T , one can account for the fact that it is water vapour that is produced in HT-PEMFCs rather than liquid water. The thermodynamic data is evaluated using the NASA thermodynamic database (McBride et al., 2002).

The total heat released from each cell (Q_{cell}) is some of the reversible and irreversible heat of energy in the stack and it can be written as,

$$Q_{cell} = \left(-\frac{\Delta H_{g,T}}{nF} - V_{cell} \right) I_{cell} \quad (3.14)$$

The volumetric heat generation can be written as,

$$q_{catalyst} = Q_{cell} A_{cell} / V_{catalyst} \quad (3.15)$$

Where $q_{catalyst}$ is the volumetric heat produced from the cathode catalyst layer and $V_{catalyst}$ is volume of cathode catalyst layer. The resulting Poisson's equation for the thermal energy balance is solved in the cathode catalyst layer. This source term is introduced into the energy balance equation as a user defined function (UDF) at every grid node of the cathode catalyst layer. A listing of the computer program is given in Appendix A

The total amount of heat released from the stack can be written as,

$$Q_{st} = Q_{cell} N_{cell} \quad (3.16)$$

3.1.4 Estimation of heat losses from the stack

It is expected that some amount of the heat generated in the stack will be removed by natural convection and radiation. We estimate these by assuming that the four side edges, two of which are horizontal (the top and the bottom) and the other two (side edges) vertical, are free of encumbrances and are therefore free to remove heat by natural convection and radiation. Since

the cell cross-section is rectangular, all the four faces have rectangular areas. The amount of heat removed by natural convection can be calculated using appropriate correlations expressed in terms of Grashof and Rayleigh numbers (Holman, 1986) for natural convective heat transfer from vertical and horizontal plates.

$$Gr_j = (g \beta (T_{st} - T_0) L_j^3) / \nu^2 \quad (3.17)$$

where Gr_j is the Grashof number, g is the gravity, j is the index representing the vertical, horizontal top face and horizontal bottom faces, β is the thermal expansion coefficient of air, T_0 is the ambient air temperature, L is the characteristic length of the edge and ν is the kinematic viscosity of the medium.

$$T_f = (T_{st} - T_0)/2 \quad (3.18)$$

where T_f is film temperature and the thermal expansion coefficient can be calculated as

$$\beta = 1/T_f \quad (3.19)$$

The Rayleigh number depends on the Grashof number and Prandtl number and it can be written as

$$Ra_j = Gr_j Pr_j \quad (3.20)$$

The Nusslet number can be written as

$$Nu_j = C (Ra_j)^M \quad (3.21)$$

where C , M varies for vertical, horizontal position faces as given in Table 0.3.

The heat transfer coefficient for vertical face, horizontal face of the stack can be written as

$$h_{N,j} = Nu_j k / L_{ch,j} \quad (3.22)$$

k is the thermal conductivity. The convective heat transfer from the j^{th} face of the stack can be written as

$$Q_{N,j} = h_{N,j} A_j (T_{st} - T_0) \quad (3.23)$$

where A is the area of edge. The total amount of the heat transfer by natural convection through four edges of stack can be written as

$$Q_{N,Total} = \sum Q_{N,j} \quad (3.24)$$

Assuming that all the surfaces are at a temperature of 200°C and that ambient air temperature is 30°C, the heat removal rate by natural circulation comes about~5% of the total thermal load.

The radiative heat transfer rate from the stack can also be similarly estimated. The emissivity of the graphite is reported to be between 0.3 and 0.7 (Cunningham, 2007).

Table 0.3: Natural convection heat transfer equation constants.

Geometry type	Ra	C	M
Vertical face	10^4-10^9	0.59	1/4
	10^9-10^{13}	0.021	2/5
	10^9-10^{13}	1/3	2/5
Horizontal face: upper surface of the heated plates or lower surface of the cooled plates	$2 \times 10^4-8 \times 10^6$	0.54	1/4
	$8 \times 10^6-10^{11}$	0.15	1/3
Horizontal face: lower surface of the heated plates or upper surface of the cooled plates	10^5-10^{11}	0.58	1/5

The total amount of the heat transfer by radiative heat transfer can be calculated by following equation

$$Q_{rad} = \sigma \varepsilon A_{st} (T_{st}^4 - T_0^4) \quad (3.25)$$

Where σ is the Stefan–Boltzmann constant and that is equal to $5.67 \times 10^{-8} \text{ J/s m}^2 \text{ K}^4$, ε is the emissivity of the material. Taking a mean value of 0.5 for ε and taking the surface temperature of the plates to be 200°C, the total radiative heat transfer rate amounts to about ~6-7% of the total thermal load. The actual value may be less than this because not all the exposed surface of the plate is made of graphite.

3.2 Physical description of thermal model for a 1 kWe HT-PEMFC stack

Commercial scooters with a battery-powered engine with a maximum power of 400 W are already in the market. Given that their maximum speed is limited to about 40 kilometers per hour, we aim at an enhanced maximum engine power of 1 kWe. We therefore design an HT-

PEMFC stack capable of providing a power output of up to 1 kWe. Taking the active area of each cell to be 100 cm^2 , 24 to 40 such cells are connected in series to make up the stack which generates 1 kWe. The stack is assumed to be cooled by a cooling plate, one for every four cells, with an embedded flow field through which the coolant is circulated.

When the stack is operated at a voltage of 0.6 V per cell at an average current density of 0.42 A/cm^2 , the stack is made up of 40 cells connected in series and generates an overall voltage of 24 V. Each cell has an active area of 100 cm^2 and the bipolar plates have 50 parallel channels of a length of 100 mm and a cross-section of 1 mm x 1 mm. One cooling plate is provided for every four cells in order to remove the heat from the cells. The cooling plate also consists of 50 parallel channels of a length of 100 mm and a cross-section of 1 mm x 1 mm. The flow distribution through the parallel channels is assumed to be uniform on each plate. In order to investigate the effect of power density on the temperature distribution, calculations have also been done for a case where the cell is operated at a voltage of 0.5 V which allows a current density of 0.9 A/cm^2 . The corresponding power density is thus nearly twice as high as that in the standard case.

It can be seen from the calculations of section 3.1 that natural convection and radiative heat transfer together are expected to contribute to the removal of only ~12% of the total heat generated from a 1 kWe HT-PEMFC stack at the nominal operating temperature of 200°C . For steady operation, the rest of the heat, amounting to nearly 800 W, needs to be removed by other means. In the present study, we consider four possibilities to remove the excess heat:

using air which needs to be fed to the cathode to cool the stack by passing it through cooling plates prior to it being fed to the cathode side as air pre-heated air supply.

forced circulation of external air over the stack. It may be noted that, in a moving vehicle, this can be achieved by directing the ambient air over the stack; thus a blower may not be required for this purpose.

using air which needs to be fed to the cathode to cool the stack by passing it through cooling plates prior to it being fed to the hydrogen storage tank (hydrogen desorption is an endothermic reaction) in order supply thermal energy to the tank.

using liquid coolant which needs to be fed through cooling plates to cool the stack and pre heated air fed to the cathode.

In order to determine temperature variations, local current density variations and the non-uniform heat generations within the cell, the computational geometry is simplified to enable the equation of the four possible cases.

3.2.1 Integrated cathode air cooling

Case A is meant to simulate the following problem: heat generation in the cathode catalyst layer; its removal by conduction through the membrane on one side and the cathode side GDL on the other side; its further transfer by conduction to the other layers and removal by convection by the air flowing through the cathode flow fields and the cooling plate. To this end, a flow domain (Figure 0.2) of a length of 100 mm, width of 9.558 mm and thickness of 2 mm is considered. The model domain (which is not drawn to scale) represents one half of a four-cell unit with one cooling plate consisting of one-half of the cooling channel and the two cathode air channels on one side along with the composite solid media in-between. The heat transfer through the solid layers within the cell is assumed to be purely by conduction and the fluid flow through the flow channels is assumed to be laminar and incompressible, which is typically the case in fuel cells. While temperature variations are expected, the thermophysical properties of the media (materials and the fluids) have been assumed to be constant. The model domain has the following dimensions: thickness, in the y-direction, of 9.558 mm, height, in the x-direction, of 2 mm and length, in the flow (z) direction, of 100 mm. The extent of 2 mm in the x-direction represents a repeating unit of the parallel flow channel in the stack. The extent of 100 mm in the z-direction represents the full active length of the cell. The extent of 9.558 mm in the y-direction represents (see Figure 0.2) the total width of two cells and one half of the coolant channel (consisting of two anode and two cathode catalyst layers (each of 0.013 mm thickness), two anode and two cathode flow fields (each of 2 mm thickness with a flow channel depth of 1 mm), two membranes (each of 0.040 mm thickness) and four gas diffusion layers (each of 0.2 mm thickness) and one half of the coolant channel, which has the same dimensions as the flow field. Since the primary interest of the calculations is one of temperature and current distribution, only those flow and heat transfer features that affect these have been individually resolved. Since heat

generation occurs primarily in the cathode catalyst layers, these have been physically resolved. Since most of the heat is carried away by convection in the cathode side flow field and in the coolant channel, the geometries of these have been distinctly modeled. By the same token, the anode side flow field has not been resolved. All the other layers, namely, the membranes, the anode catalyst layers, all the gas diffusion layers and the anode flow fields have been merged into two solid layers of distinctly different thermal conductivities, namely, the membrane and the anode catalyst and the anode side GDL as a single layer having an effective thermal conductivity of 1.7 W/m K, and the GDL and the mono-polar or bi-polar plate, as appropriate, having an thermal conductivity of 20 W/m K. Thus, with reference to Figure 0.2, in the unit cell of the calculation domain, there are three fluid domains, namely, two cathode air flow fields and one coolant flow field, and seven solid domains, the details of which are given in Table 3.1. It is assumed that there is no contact resistance at the interfaces of these layers. The model is such that the air meant for the cathode side flow fields of two cells is first made to go through one-half of the cooling plate (where it picks up heat) and is then redistributed to the two channels. It may be noted that the extent of 9.588 mm in the y-direction corresponds to 1/20th of the width of the stack; thus, 20 such segments in the width direction will equal the 40 cells (with 10 cooling plates) of the stack. The thermophysical properties and thicknesses of the various materials used in the study are given in Table 3.1.

3.2.2 Additional heat removal through a coupled H₂ storage system

Case B computational domain is the same as case A and a heat sink term is applied on the channel connecting the cooling plate and the individual cathode flow channels on the cells. Air enters the cooling plate at a temperature of 30°C at a stoichiometric factor to be determined. It gets heated as it flows through the cooling plate, thus extracting heat from the hot cells surrounding the cooling plate. At the exit of the cooling plate, the hot air would go through the desorption section of the metal hydrate unit and would give up heat to the metal hydride.

The cooler exit gas from the metal hydride would then be fed through the cathode side of the fuel cells where they supply oxygen and in the process get also heated, again extracting heat from the cells. The objective is to see if in this process sufficient heat is given to the desorption unit to generate the required amount of hydrogen while keeping the cells (including the catalyst

layers and the membranes) sufficiently warm so that the electrochemical performance does not differ but not so hot that the materials themselves degrade. The hydrogen desorption unit is mode

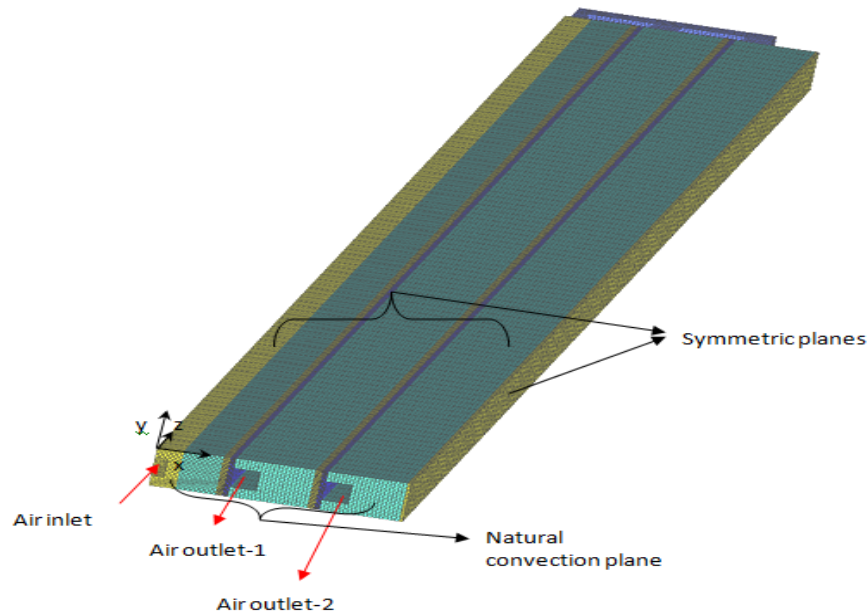


Figure 0.2: Schematic diagram of the computational domain showing one half-channel of the cooling plate and cathode flow channels in two cells.

-eled as a heat sink term applied on the channel connecting the cooling plate and the individual cathode flow channels on the cells. This connecting channel is thus located outside of the stack area. The flow domain consists of one air flow inlet (into the coolant plate) and two air flow outlets, one each in the cathode flow fields. Figure 0.3 shows schematic diagram of a portion of the fuel cell stack showing the arrangement of one cooling plate for every four cells with combination of metal hydride tank.

3.2.3 External cooling with air-flow over stack

Case C is meant to simulate the heat generation within the catalyst layers and its subsequent removal by forced convection from the edges of the stack. This requires consideration of the entire width, i.e., all the 50 channels, of each bipolar plate. This makes the computations too cumbersome. Therefore the heat loss to the cathode air is not explicitly modeled; the strength of

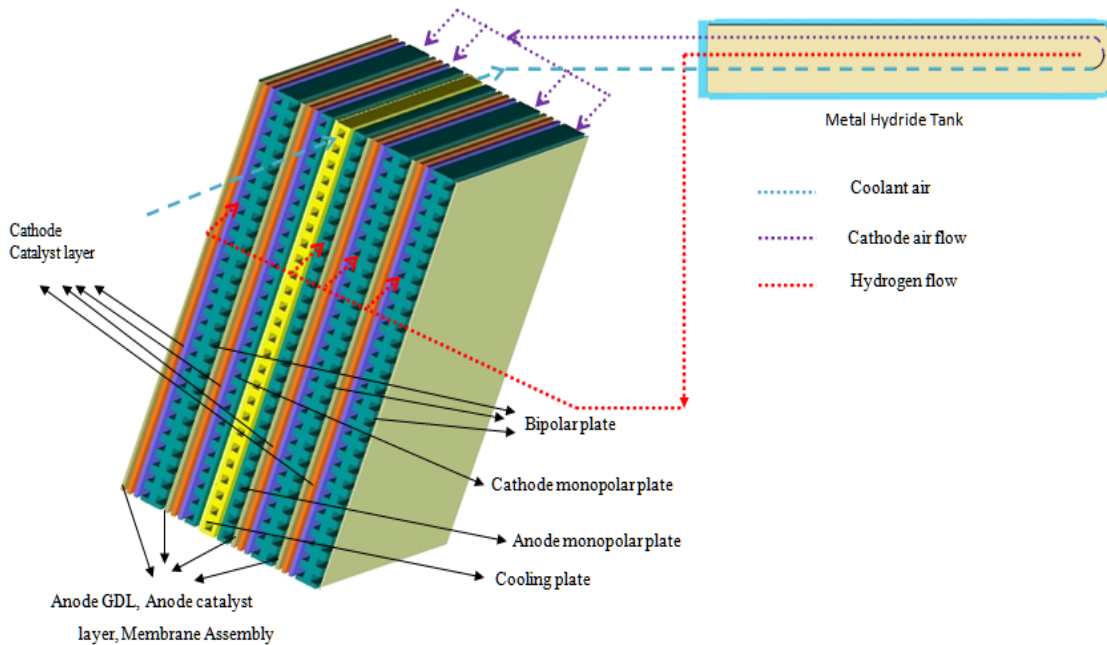


Figure 0.3: Schematic diagram of a portion of the fuel cell stack showing the arrangement of one cooling plate for every four cells with combination of metal hydride tank.

the heat generation term in the membrane electrode assembly (MEA) is reduced to account for the heat loss (which is equal to $m^*C_p(T_{out}-T_{in})$ where m^* is the mass flow rate, c_p is the specific heat, T_{out} and T_{in} are the temperature at the outlet and inlet of the cathode air respectively). Thus, a domain (Figure 0.4) of length of 100 mm, width of 100 mm and thickness of 15.864 mm is modeled. The computational domain contains solid layer and MEA is taken as heat source term (heat sink is varied with a amount of cathode air flow). It may be noted that the thermal conductivities of the GDL, the membrane and the catalyst layer are very nearly the same while that of the graphite plate is an order of magnitude higher. Therefore, the calculation domain is divided into two parts: that belonging to the MEA with a thermal conductivity of 1.23 W/m K and that belonging to the graphite with a thermal conductivity of 20 W/m K. A distributed and equivalent constant volumetric heat generation term is specified in the MEA while only conduction takes place in the graphite region. Convective heat transfer from the sides is modeled by specifying a convective heat transfer boundary condition. Since the heat loss to the cathode air is not explicitly modeled, it is not necessary to solve for the velocity field and the

problem reduces to one of conduction through a composite domain with convective thermal boundary conditions. Thermal and physical properties of air used to estimate the natural convective heat transfer coefficient are given in Table 3.4.

Table 0.4: Properties of air.

	At 303 K (Bulk Temperature)	388 K (film average temperature)	
Density, ρ	1.255	0.922	Kg/m ³
Specific heat, C_p	1006	1011	J/kg K
Thermal conductivity, K	0.0242	0.032	W/m K
Thermal expansion coefficient, β	3.2×10^{-3}	2.615×10^{-3}	1/K
Kinematic viscosity, ν	1.4604×10^{-5}	2.4131×10^{-5}	m ² /s
Prandtl number, Pr	0.712	0.702	

3.2.4 Cooling with a liquid coolant

Case D computational domain is the same as that for case A except that heat transfer oil is used as a liquid coolant in the coolant and cathode flow channels in each cell have separate inlets. Schematic diagram of the liquid cooling is shown in the Figure 0.4. In the fluid domains, the treatment of the coolant flow is exact; the treatment of the cathode side fluid flow is approximate in the sense that the variation of the gas composition (due to the consumption of oxygen and the generation of water vapour due to the electrochemical reaction) is neglected. Since the focus of the problem is on the thermal management of the stack, this simplified model is thought to be adequate.

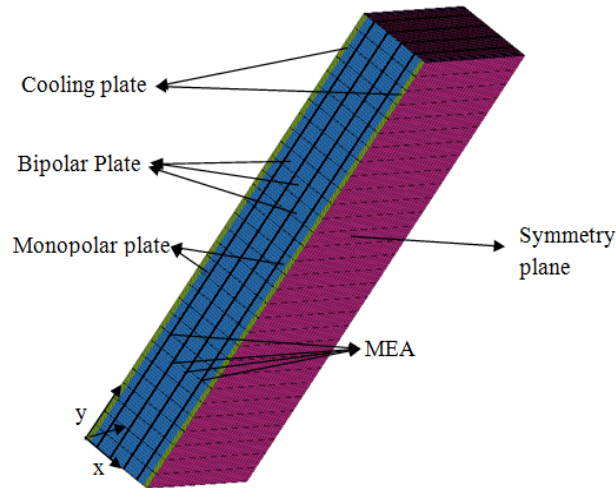


Figure 0.4: Schematic diagram of the computational domain for external cooling with air-flow over stack with four fuel cell units placed sandwiched between two half-cooling plates.

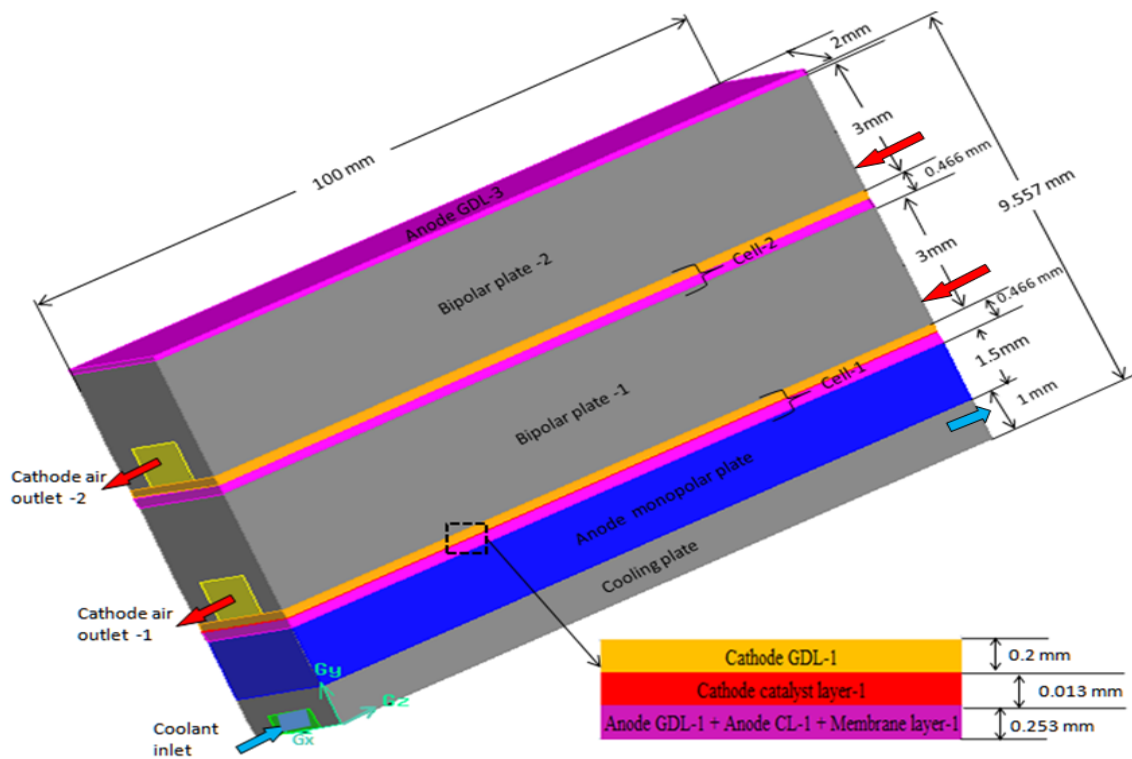


Figure 0.5: Schematic diagram of the computational domain showing one half-channel of the cooling plate, and cathode flow channels in two cells. The figure on the bottom shows the cell with components.

3.3 Computational models

3.3.1 Governing equations

The present calculation methodology is based on CFD simulations in which the fundamental equations governing the flow, namely, conservation of mass (equation 3.20) and conservation of momentum (equation 3.21) and conservation of energy are solved numerically.

For steady flow, neglecting buoyancy effects, these are given by mass balance equation:

$$\nabla \cdot \vec{v} = 0 \quad (3.26)$$

where \vec{v} is the velocity vector.

Momentum balance equation:

$$\rho(\vec{v} \cdot \nabla \vec{v}) = -\nabla p + \mu \nabla^2 \vec{v} \quad (3.27)$$

where μ is its dynamic viscosity medium and p is the static pressure.

Energy balance equation:

$$\rho C_p (\vec{v} \cdot \nabla T) = k \nabla^2 T + S_e \quad (3.28)$$

where C_p is the specific heat of the medium, T is temperature, K thermal conductivity of material and S_e is a volumetric source term.

The varying local current density, volumetric heat source values with respect to local temperature equations are included by using user defined functions (UDF) in the simulation. The CFD simulations have been carried out using the commercial finite volume CFD software ANSYS-FLUENT, version 6.3.26. The discretization is formally second-order accurate and grid independence of the results has been verified by comparing predictions of temperature contours on the catalyst surface for a range of grid sizes; this is discussed further in the section 3.3.3.

3.3.2 Boundary conditions

The computational domain and the boundary conditions applied for the three cases are shown schematically in Figure 0.3 for Case A, Case B and Case D. The following boundary conditions have been imposed on the computational domain of a Case A, Case B and Case D. Since the x and the y-directions are repeating units, symmetric boundary conditions (i.e., zero normal gradients) have been specified on the boundaries in these two directions. Natural convective heat transfer boundary condition, with a heat transfer coefficient of $9 \text{ W/m}^2 \text{ K}$ and a bulk temperature of 30°C , have been applied as the thermal boundary condition on the two z-direction boundaries of the computational domain. In the fluid domains on these boundaries, uniform velocity and temperature conditions have been specified at the inlets (at $z = 0$) while an outflow boundary condition has been specified at the other z-face located at $z = 0.1 \text{ m}$.

The following boundary conditions have been imposed on the computational domain of a Case C. The convective heat transfer from the sides is modeled by specifying a convective heat transfer boundary condition on the four edges of the stack as shown in Figure 0.4. Since the x-direction is a repeating unit, symmetric boundary conditions have been specified on the boundaries in these two edges of x-direction.

3.3.3 Grid independence

Grid independence of the results has been verified by comparing predictions of temperature contours in Case A on the catalyst surfaces for 0.83×10^5 cells, 1.77×10^5 cells, 6.97×10^5 cells and 10.49×10^5 cells which is shown in Figure 3.1. Marginal differences (of the order of 0.3 K in the predicted volumetric maximum temperature in the cathode catalyst layer-2) were found between the predictions with the last three grids, the variation are shown in Figure 0.6. The temperature contours of cathode catalyst layer-1 are shown in Figure 0.7 and it showing those temperature profile variation is very less. The results obtained with 1.77×10^5 cells are used in the flowing calculations (10 cm parallel channel).

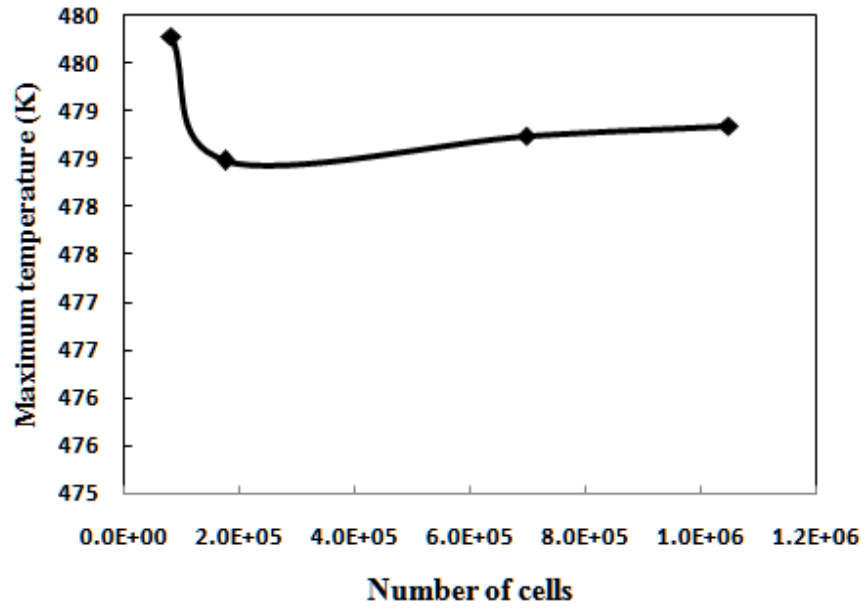


Figure 0.6: Grid independence test for Case A computational domain with a constant heat source value and constant inlet velocity.

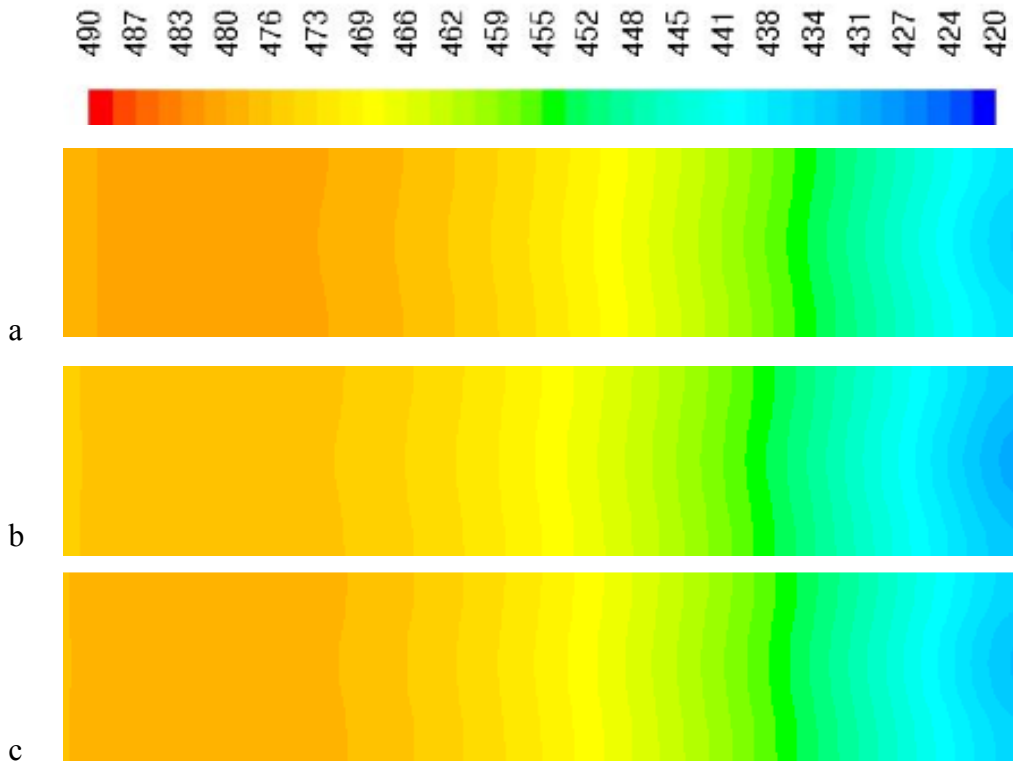




Figure 0.7: Temperature (K) contours in the cathode catalyst layer-1 varying grid sizes (a) for 0.83×10^5 cells, (b) 1.77×10^5 cells, (c) 6.97×10^5 cells and (d) 10.49×10^5 cells.

3.3.4 Numerical details

Similarly the grid independence is verified for the 20 cm, 30 cm parallel channel and geometry extension with 10 cm, 20 cm and 30 cm four parallel serpentine channel. The corresponding number of cells used are given in the Table 0.5.

Table 0.5: Numerical details of the computational domain.

	Domain dimensions (Length \times Width \times Thickness mm ³)	Number of Cells $\times 10^{-5}$	Number of Faces $\times 10^{-5}$	Number of Nodes $\times 10^{-5}$
Parallel channel (PC)	100 \times 2 \times 9.558	1.77	5.72	2.15
	200 \times 2 \times 9.558	8.85	27.91	10.16
	300 \times 2 \times 9.558	13.28	41.84	15.23
Four parallel serpentine channels (FPSC)	100 \times 24 \times 9.558	13.16	41.60	15.15
	200 \times 24 \times 9.558	24.48	77.27	28.07
	300 \times 24 \times 9.558	35.23	111.27	40.45

3.3.5 Validation

Validation of the calculation methodology has been carried out by comparing the numerical solution with an analytical solution to the one-dimensional case. This is shown below in Figure 0.8 where the computed solution is compared with the analytical solution for the same thickness of the various layers, the same thermophysical properties, heat generation term in the cathode catalyst layer and the same boundary conditions. It can be seen that excellent agreement is obtained between the CFD solution and the analytical solution.

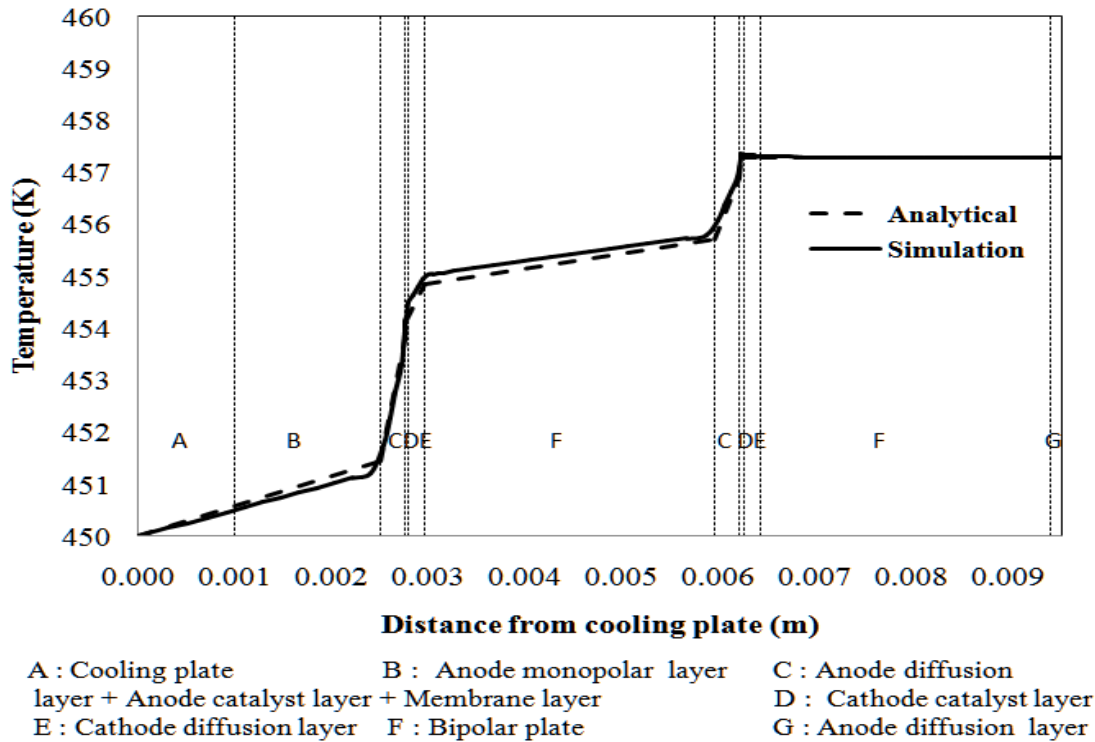


Figure 0.8: Comparison of the computed temperature profile along the stack thickness of two cells and one cooling plate with the analytical solution for a one-dimensional case.

Further validation is provided by comparison with the experiments results of Supra et al.(2013) who have reported measurement of cell. temperatures in a 1 kWe, liquid-cooled HT-PEMFC stack with one cooling plate for every three cells. The fuel for the cell was reformat gas and the liquid coolant entered the stack at 433 K which was also the operating temperature of the stack. The measured temperature variations in the cells in between the cooling plates showed a temperature variation of ~6 to 8 K with a maximum variation of 8.3 K. These variations are consistent with those shown in Figure 0.8. Supra et al. (2013) present data of local temperature obtained under constant current mode of operation which show (Figure 0.9) that the temperature variation along the stack thickness by about ~7 K (one half-channel of the cooling plate with two cells)and that the variation correlates well with that of the cell voltage. As will be seen similar variations are predicted by the present 3-D model when the liquid coolant temperature at entry is close to the operating temperature of the cell, Figure 0.10 shows that the temperature variation along the stack thickness by about ~8 K (one half-channel of the cooling plate with two cells).

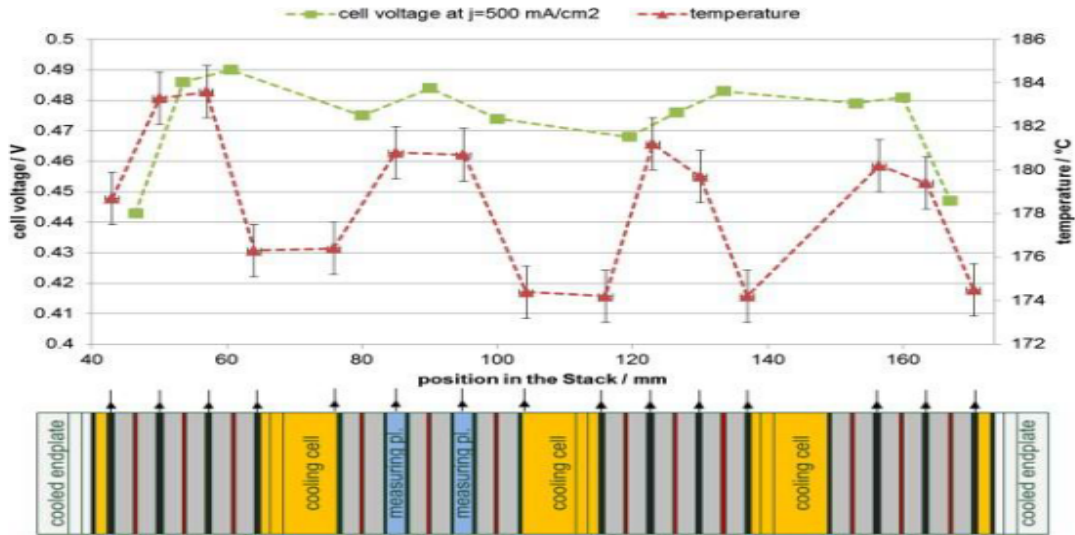


Figure 0.9: Temperature profile along the stack thickness for a 1 kWe HT-PEMFC stack operated in a constant current mode (Supra et al., 2013).

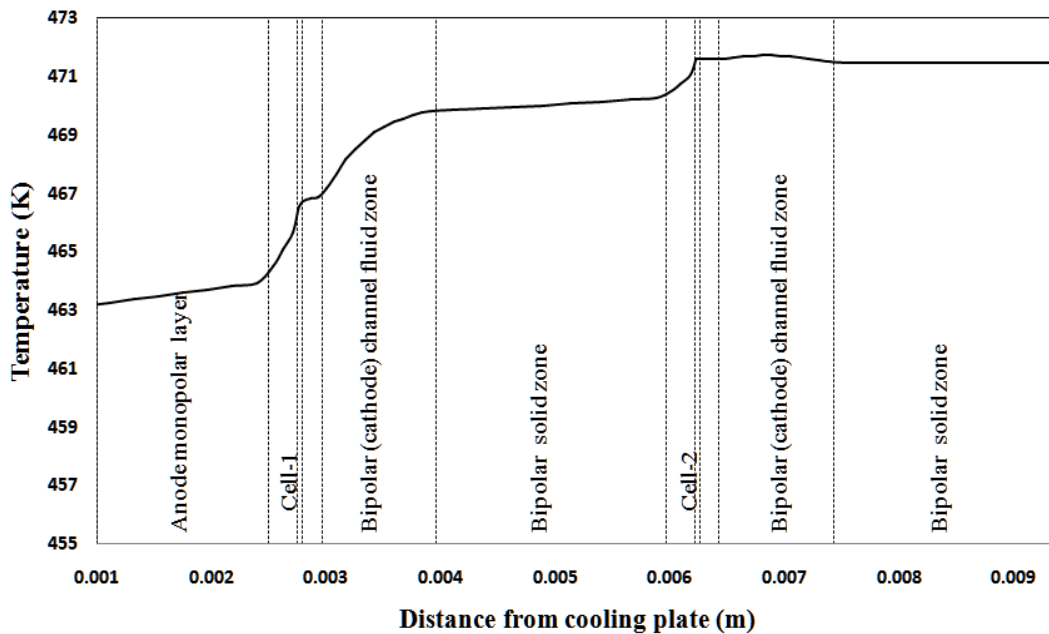


Figure 0.10: Computed temperature profile along the stack thickness (one half-channel of the cooling plate with two cells).

Although a one-to-one correspondence cannot be made, these results are consistent with the predictions of the present work and thus serve to validate it to some extent.

CHAPTER-4

EVALUATION OF DIFFERENT THERMAL MANAGEMENT OPTIONS

One of the important challenges in thermal management is to maintain as high and as uniform a cell temperature as possible. The cell current density increases with an increase in the cell temperature due to enhanced reaction kinetics or lower activation losses and a higher ionic conductivity at elevated temperatures. Higher current density implies not only higher electrical output but also higher thermal output. It is necessary to minimize temperature gradients within the cell so as to operate it at as high an average cell temperatures possible without exceeding the maximum temperature limits set by material considerations. In the present study, we take the permissible temperature limit to be 473 K (which is perhaps at the higher limit of the operational range of PBI membranes) in the catalyst layer (the limit applies to the membrane; in the present model, the MEA is treated as a single unit and the condition is therefore applied on the catalyst layer) and study the effect of various operational and design parameters on the net power output from the stack. The variables of specific interest therefore are the temperature and current distributions in the various layers of the stack, the pressure drop in the coolant which defines the parasitic power required by the coolant circulation system, and the weight of the coolant plates which will increase the overall weight of the stack. The principal variables considered are the inlet temperature and the flow rate of the coolant, the number of coolant flow fields, the thermal conductivity of the plate material and the stoichiometric factor on the cathode side. It is shown that through an optimal combination of these parameters, temperature variations within the cell can be made as small as 10 K in an HT-PEMFC stack nominally rated at 1 kWe. The calculations have been carried out for air, water and Duratherm heat transfer oil as the coolant. The use of the heat transfer oil enables a higher coolant temperature and it is clearly the most superior of the three coolants. Therefore, the results obtained only with Duratherm oil as the coolant are further studied for the optimal design of a 1 kWe stack. Since heat transfer by natural convection, where the convective heat transfer coefficient is typically of the order $9 \text{ W/m}^2 \text{ K}$, is not effective and contributes to only about 10% of the heat removal; its effect is neglected in the present study.

The organization of the rest of the chapter is as follows. Thermal management strategies for a 1 kWe stack (a 40 cell stack produces a nominal power of 1 kWe at cell voltage of 0.6 V and current density of 0.42 A/cm²). In section 4.1, the possibility of using cathode air is considered. If sufficient heat transfer flux is available then the coolant system is considerably simplified. In section 4.2, the possibility of using the preheated cathode air for hydrogen desorption from a storage tank is considered. In section 4.3, the effectiveness of external stack cooling is investigated. In section 4.4, the characterization of a liquid coolant system is studied. A detailed study of the effect of a number of parameters on the efficiency of a 1 kWe stack is presented in section 4.5.

4.1 Integrated cathode air cooling

In integrated cathode air cooling a high air flow-rate is forced through cooling channels before it is introduced into the bipolar plate air channels. These higher than normal air flow-rates are possible only because the phosphoric acid doped PBI membrane does not dry out at these flow-rates as a liquid water based proton conducting Nafion[®] membrane would.

4.1.1 Heat removal primarily by cathode air

In order to study heat removal by cathode air alone, the flow domain shown in Case A is used with external cooling restricted to that by natural convection, which is represented by specifying a convective heat transfer coefficient of 9 W/m² K, and an ambient air temperature of 303 K. Air, at a flow rate equal to a specified stoichiometric factor and at an inlet temperature of 303 K, enters the cooling plate. As it flows through, it picks up heat at a rate determined by the temperature distribution in the cooling plate. At the exit, it splits into parts and flows through the cathode side flow channels of two cells (the geometry modeled here has one half of the cooling plate only; in the real case, the flow from the cooling plates splits into four parts and enters the four adjacent channels). Depending on the air temperature and the surrounding bipolar plate temperature, it may pick up heat or it may even lose heat to the bipolar plate. A zero-gauge pressure boundary condition is employed at the exit from the cathode flow fields so that the flow distribution in the two adjacent cells may be different. Each of the two adjacent HT-PEMFCs has a cathode catalyst layer. A volumetric heat generation term, representing the net heat to be removed, amounting to 913 W for the entire stack, is specified in each of the catalyst layers.

Typical results from these calculations are shown in Figure 4.1 where the temperature contours are compared for different air flow-rates, expressed in terms of stoichiometric factor. The temperature contours in a z-x plane passing through the mid-flow field height (see 3.2.1 for the geometrical details) are shown here. This enables one to see the air temperature in the cathode side flow fields and in the cooling plate as well as the temperature in the surrounding membranes, GDLs and bipolar plates. It can be seen that for a stoichiometric factor of 3, the temperature in the cell is of the order of 700 to 800 K, which is well above the limit for the safe operation of the PBI membrane. As the stoichiometric factor is increased, the temperature in the cells decreases. At a stoichiometric factor of 10, the cell temperature varies in the more acceptable range of 400 to 500 K. The results from these calculations are summarized in Table 4.1 which shows the air flow-rate, the amount (percent) of heat removal by air and by free convection, and the maximum temperature within the cell. It can be seen that when the air flow rate is twice that required to supply the oxygen necessary to maintain a current density of 0.42 A/cm^2 , i.e., for a stoichiometric factor of two, the air flow rate is so low that it heats up considerably; the cell temperature is also very high even though a significant amount of heat is removed by free convection. It is only when the stoichiometric factor is increased to 10, i.e., only when ten times more oxygen than what is electrochemically required is supplied, do we see the maximum cell temperature within acceptable limits.

The above results have been shown for a current density of 0.42 A/cm^2 , which is fairly small compared to that for LT-PEMFC. Studies have indicated (Korsgaard et al., 2006) that it can be as much as 0.90 A/cm^2 at a cell voltage of 0.5 V. The higher current density implies higher heat generation rate and therefore a requirement for a higher heat removal rate. In order to see the effect of this higher current density on the temperature distribution, calculations have been repeated for the same computational domain as in case A with a higher volumetric heat generation rate corresponding to an average current density of 0.90 A/cm^2 . The results, in terms of the variation of the maximum material temperature (GDLs, catalyst layers, bipolar plates, membranes; note that the temperature variation is not very large in the different media) in the cell with the stoichiometric factor, are shown in Figure 4.2.

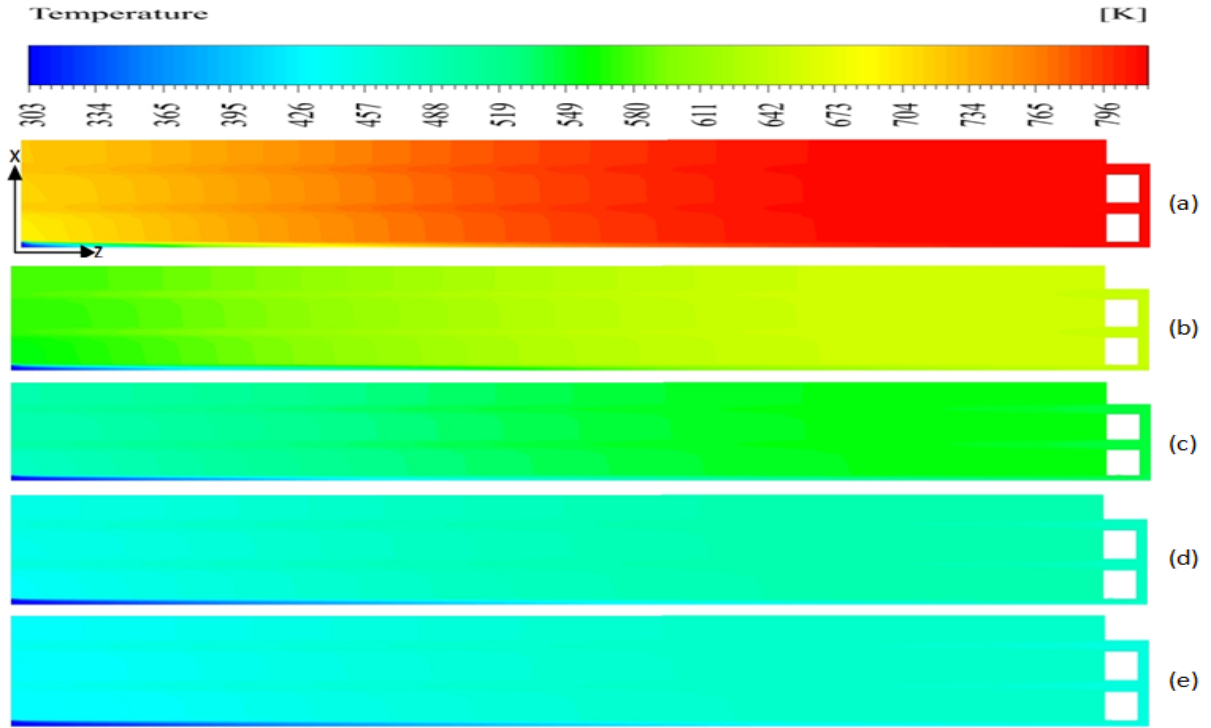


Figure 4.1: Temperature (K) contours of cell layers for stoichiometric factor of cathode air of (a) 3, (b) 5, (c) 7, (d) 9 and, (e) 10.

Table 4.1: Variation in the amount of heat removed with stoichiometric ratio of air in Case A.

λ	Velocity (m/s)	Heat removed out by coolant (%)	Heat removed by free convection (%)	Maximum temperature in the stack (K)
2	1.96	79.43	20.57	983
3	2.94	84.84	15.16	814
4	3.93	88.03	11.97	714
5	4.91	90.16	9.84	646
6	5.89	91.69	8.31	595
7	6.87	92.81	7.19	577
8	7.85	93.71	6.29	526
9	8.83	94.43	5.57	501
10	9.81	95.02	4.98	481
11	10.79	95.50	4.50	464

It can be seen that while there is a significant increase in the maximum stack temperature at low stoichiometric factors, the effect is not so large at high stoichiometric factors. It may be noted that the air flow rate in the two cases (low and high current density) is different for the same stoichiometric factor because the oxygen requirement is directly proportional to the current density. Thus, it appears that a stoichiometric factor of about ten is required to maintain the temperature of the materials to within 473 K over a range of current densities.

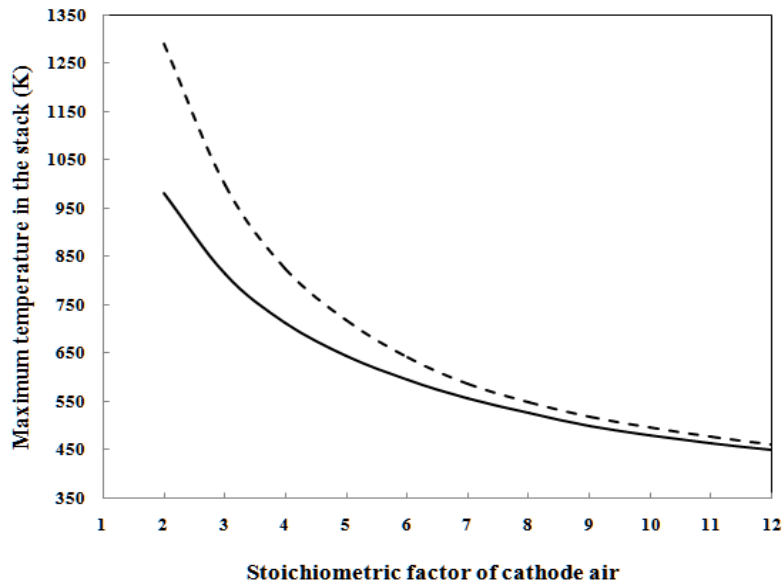


Figure 4.2: Variation of the maximum temperature in the stack with the stoichiometric factor of air at current density of 0.42 A/cm^2 (solid line) and 0.90 A/cm^2 (dashed line).

4.1.2 Taking account of current density variation with temperature

The above results show that there is a temperature variation across the cell. It is well known that, at a constant voltage, the current density varies with temperature. For HT-PEMFCs, this relation among the three variables is captured using an empirical formula by Korsgaard et al., (2006a, 2006b). They obtained the constants using their own experimental data from a PBI-membrane-based HT-PEMFC and the resulting equation is given by equation (3.6). Section 3.1.3 enables one to take account of current density variations arising out of temperature variations if the voltage is known. Equation (3.6) is expressed in terms of current density as the dependent variable and temperature as the independent variable in the following way for a constant voltage

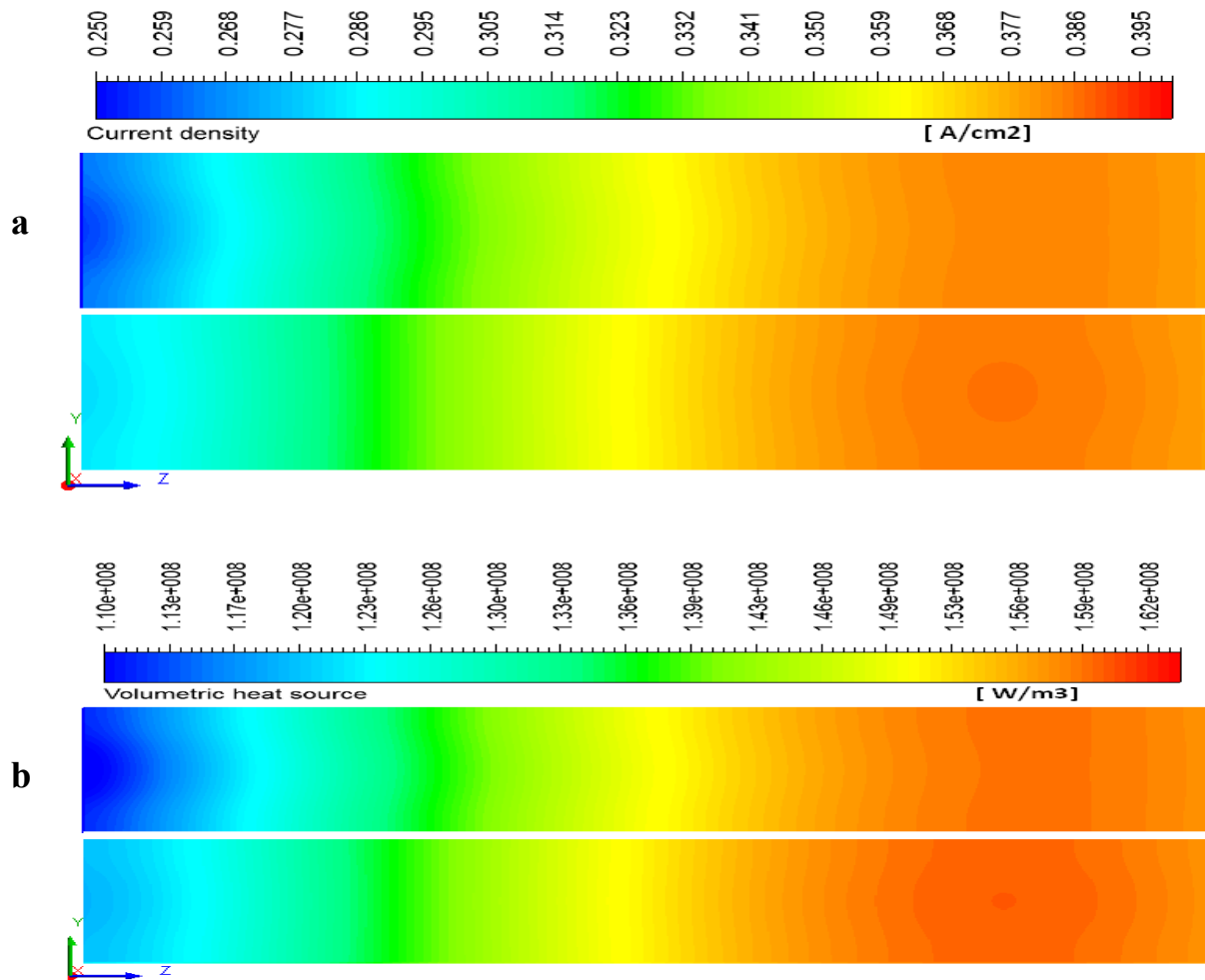
of 0.6 V. Using equation (3.6), it is possible to calculate the local current density (which will then define the equivalent heat source term through equation (3.18) for a local temperature on the catalyst surface calculated through the CFD calculations of the mass, momentum and energy balance equations.

We have introduced equations into the CFD calculations in the form of a user defined function (UDF) within FLUENT and calculated the temperature field again. Since the current density decreases with temperature, the heat source decreases as per equation (3.18) in areas of low temperature. Since the design criterion is that the temperature on the catalyst surface should not exceed 473 K, this results in a lesser current density and thus lesser power output as compared to the case of assumed constant current density which then led to a decrease in the maximum temperature. This gave rise to the possibility of decreasing the cathode air flow rate. Eventually, through an iterative calculation, it was found that a reduced cathode stoichiometric factor of 9.6 gave a maximum catalyst temperature of 463 K. This means the stoichiometric factor (λ) can be lower than 9.6 if $T_{\max}=473$ K.

The spatial variation of the current density, the heat source and the temperature on the surface of the catalyst layers and in the bipolar plates predicted under this condition, namely, stoichiometric factor of 9.6 and constant voltage of 0.6 V, are shown in Figure 4.3. It may be noted that in order to bring out the contours clearly, a scale factor of 10 is used in the y-direction in Figure 4.3. It can be seen from Figure 4.3a that there is nearly $\pm 20\%$ variation in the current density over the mean value which itself is reduced by about 17% compared to the nominal value. As a result, the heat source also varies considerably (Figure 4.3b). The predicted temperature in the catalyst layers (Figure 4.3c) varies between 423 K and 463 K with a relatively cold spot forming on the catalyst layer closest to the cooling plate and a hot spot forming on the other catalyst layer. Under these conditions, the temperature variation over the cell and across the different layers in the stack is confined to about ± 25 K around the mean value. The temperature variation in the catalyst layer leads to the aforementioned reduction in mean current density. The temperature profiles at various z-positions, i.e., in the air flow direction in the cooling plate, at mid-channel height, are shown in Figure 4.4. for an air flow rate corresponding to a stoichiometric factor of 9.6. Here, the position $z = 0$ corresponds to the entry of the air into the cooling channel. It can be seen the temperature variation in the z-direction, i.e., along the flow

direction, is rather small except in the flow fields where flow effects can be seen. However, in the x-direction, i.e., across the GDLs, the catalyst layers and the bipolar plates, there is rather considerable temperature difference, amounting to about 45 K between the maximum and the minimum values. As expected, the temperature gradients within the cooling channel are rather high; these can be attributed to the fact that the cathode air enters the cooling plate at a temperature of 303 K and gets heated, rather fairly uniformly, to about 435 K at the exit.

These calculations show that cooling of the stack by cathode air alone is possible but at a high stoichiometric factor of 9.6. Under these conditions, the temperature variation over the cell and across the different layers in the stack is confined to about ± 25 K around the mean value. As shown in Figure 4.3, this leads to a variation of about $\pm 20\%$ in the current density about the mean value. The power generated is also reduced by about 15% from its nominal value.



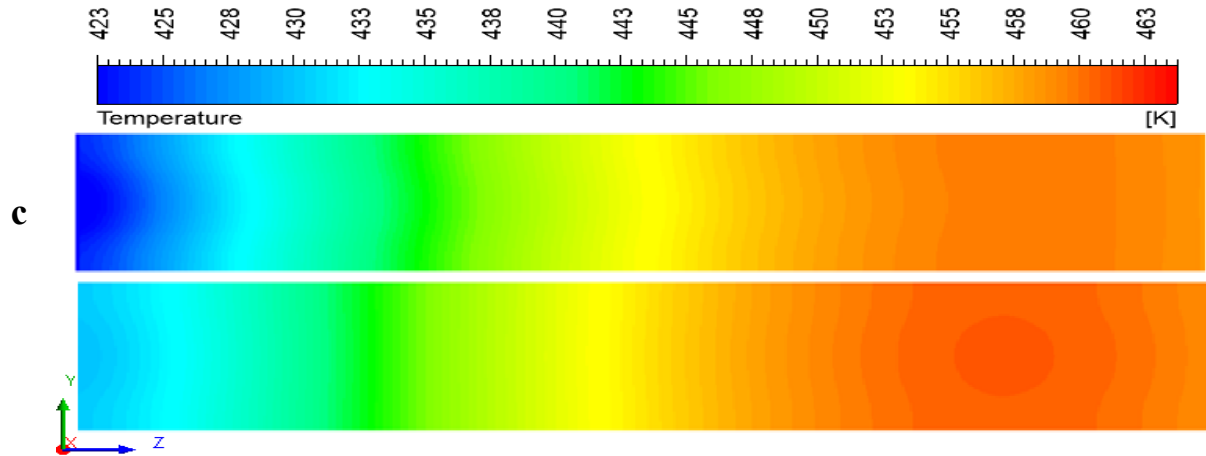


Figure 4.3: The spatial variation of the (a) current density, (b) the volumetric heat source and (c) the temperature in the catalyst layers.

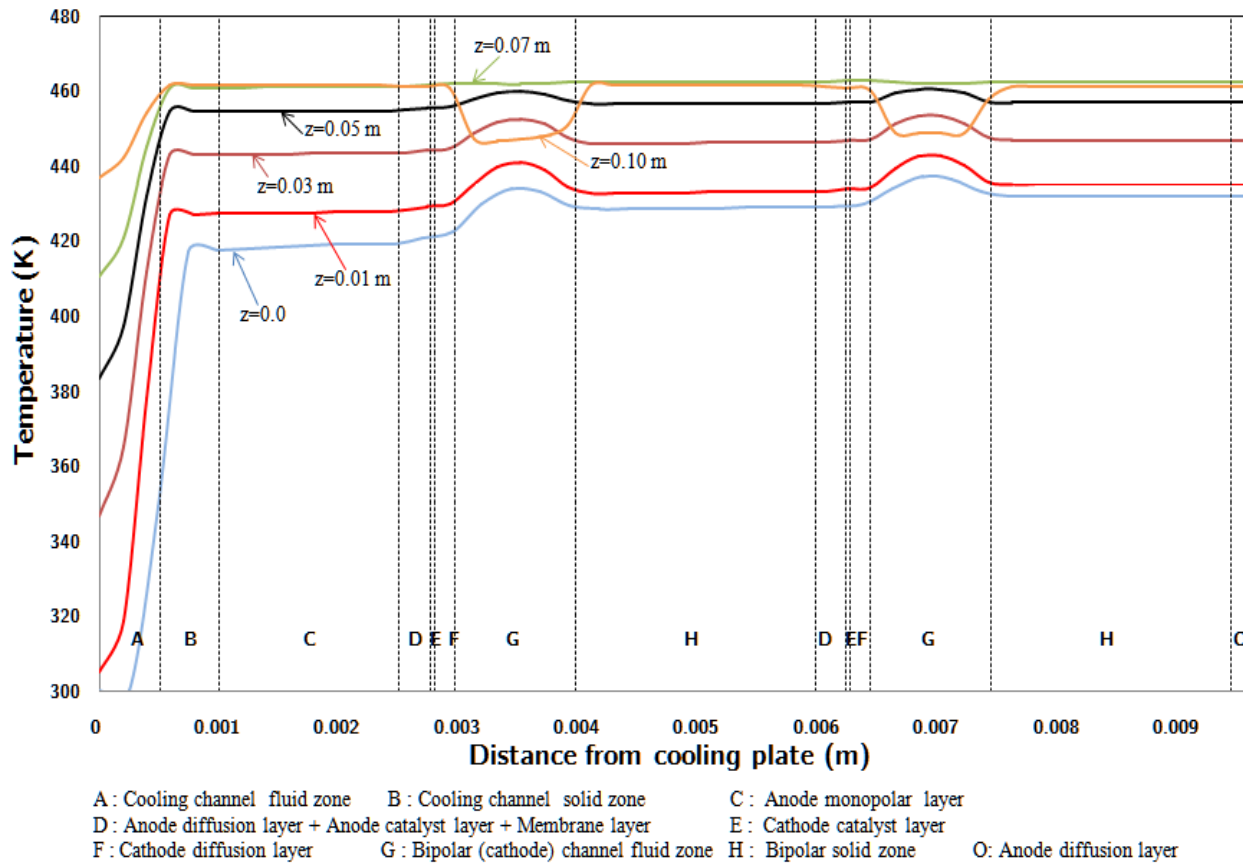
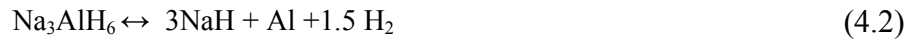


Figure 4.4: Temperature profiles along the stack repeat unit: two cells and one cooling plate (Integrated air cooling; $i_{\text{avg}} = 0.366 \text{ A/cm}^2$; $V_{\text{cell}} = 0.6 \text{ V}$ and $\lambda = 9.6$).

4.2 Additional heat removal through a coupled H₂ storage system

The thermal energy produced from HT-PEMFCs can be coupled with processes such as on-board fuel reforming and hydrogen storage. The two possible methods of supplying fuel for PEMFCs in automobiles are either stored hydrogen or hydrogen produced from an on-board fuel reformer. Hydrogen storage in the form of metal hydrides is one of the best options among storage methods, due to their high volumetric capacity and high safety during storage. Typically, hydrogen is stored in a metal hydrate such as sodium alanate (NaAlH₄) with a doped catalyst such as cerium. Sodium alanate (NaAlH₄) doped with cerium catalyst has fast hydrogen absorption and desorption kinetics and the primary reactions are shown below.



The first two reactions take place at a pressure of 100 bar and in the temperature range of 423-453 K. These reactions require 37-47 kJ/mol-H₂ (Pfeifer et al., 2009; Forde et al., 2009; Ahluwalia et al., 2011). The third reaction however occurs at temperatures of the order of 673 K and cannot be carried out with HT-PEMFCs which operate in the temperature range of 150-200°C.

In the present section, the possibility of using the heat released by the HT-PEMFC for the desorption of sodium alanate in order to extract the hydrogen required to run the cell is investigated. The thermal energy extraction from the HT-PEMFC stack can be done using a separate coolant like thermal oil which gets heated as it passes through the fuel cell and exchanges its heat with the H₂ storage system as it passes through a heat exchanger/ special jacket arrangement of the metal hydride. This requires a separate coolant circuit. In view of this, in the present study, we consider the possibility of using cathode air itself to serve the triple purpose of delivering oxygen to the fuel cell, cooling the stack and supplying the heat required for the desorption of the metal hydride. This has been done using a computational fluid dynamics (CFD)-based simulation of the flow and heat transfer within the various constituents of the stack.

The simulation was carried at a cell voltage of 0.6 V while assuming in turn a constant current density and current density as a function of temperature. The operating and design parameters for the 1 kWe HT-PEMFC stack are shown in Table 4.2. The calculations leading to the evaluation of the minimum and the maximum amount of energy needed for the metal hydride tank to release one stoichiometric ratio of hydrogen are shown in Table 4.3 (H_2 utilization factor is equal to 100%). A volumetric heat sink term was applied in the connector between the exit of the air coolant channel and the entrance of the cathode air channel to simulate the heat removal to release the hydrogen from the metal hydride.

4.2.1 Constant current density

In this case we have taken the cell voltage as 0.6 V and the (constant) current density as 0.42 A/cm². Table 4.5 shows that for a given heat sink, the maximum temperature occurs in the catalyst layer and it decreases as the stoichiometric ratio of air increases. A stoichiometric ratio of air 5.90 is needed in order to cool the stack at a heat sink value of 0.32 W and a stoichiometric ratio of air 4.92 is needed for a heat sink value of energy 0.41 W.

Table 4.2: Properties and design parameters of a 1 kWe HT-PEMFC stack with a metal hydride tank.

Desired power output, P_{st}	1000	watts
Cell active area, A_{cell}	0.01	m ²
Cell voltage, V_{cell}	0.60	v
Cell current density, i_{cell}	4200	A/m ²
Cell operating temperature, T_{st}	473	K
Maximum temperature form cooling plate out, T_{Cout}	461	K
Inlet temperature coolant, T_{Cin}	300	K
Stack current, I	42	A
Stack Voltage, V_{st}	24	V
Number of cell, N_{cell}	40	
Heat produced by stack	913	W
Minimum amount of energy required for hydrogen desorption from NaAlH ₄	36700	J/mol
Maximum amount of energy required for hydrogen desorption from NaAlH ₄	46600	J/mol

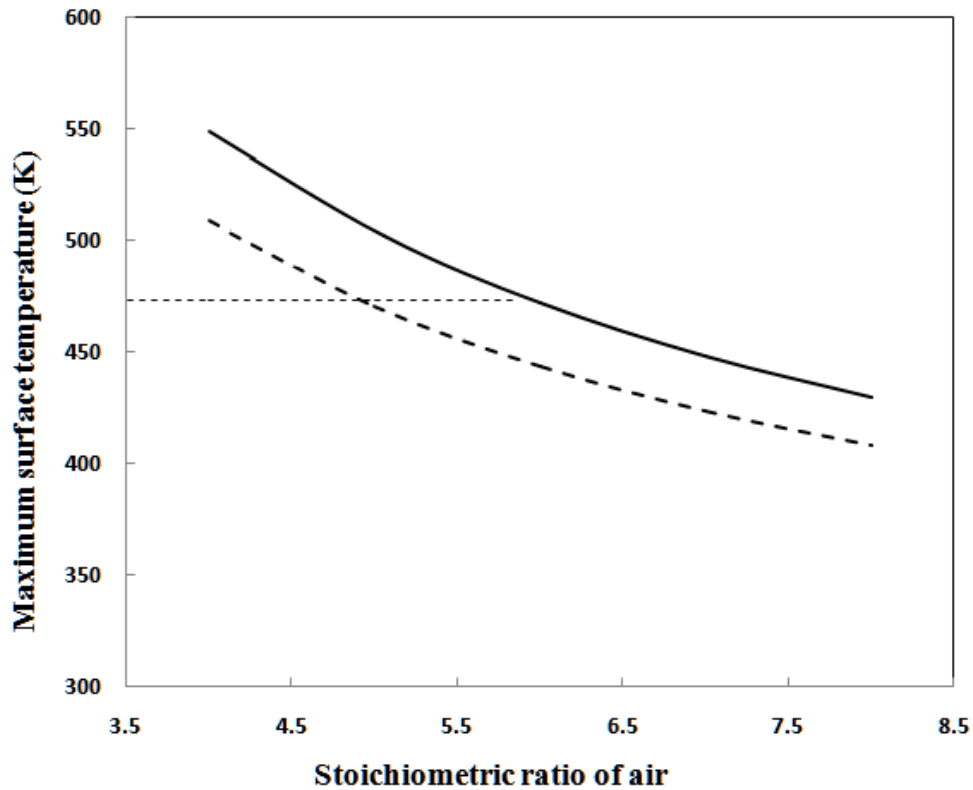


Figure 4.5: Variation of the maximum catalyst surface temperature with the stoichiometric factor for energy required to release hydrogen from metal hydride: minimum energy (solid line) and maximum energy (dashed line) at current density of 0.42 A/cm^2 .

Table 4.3: Mass and energy balances of a 1kWe HT-PEMFC stack with a metal hydride tank.

	Stoichiometric factor H_2 is equal 1		
	Simulated slice	Single cell	Stack
H_2 required (mol/sec)	8.71×10^{-06}	2.18×10^{-04}	8.71×10^{-03}
Minimum heat required (W)	0.32	7.99	320
Maximum heat required (W)	0.41	10.14	406
Amount of heat produced (W)	0.91	22.93	913

When there is no heat sink (that is when no heat is used for hydrogen desorption), a stoichiometric factor of 10 was needed (Section 4.1.1) and the temperature variation over the catalyst layer was higher. The coolant coming out from the cooling plate is partially cooled in the hydrogen desorber (modeled here as a heat sink term) and it is then sent through the cathode air

flow channels. As the cathode air flows through the channel, it absorbs heat from the solid surface and thus reduces the difference between maximum to minimum surface temperature ($\Delta T_{cat1}, \Delta T_{cat2}$) of the catalyst layers. The $\Delta T_{cat1}, \Delta T_{cat2}$ decreases as the stoichiometric factor of air increases as shown in Table 4.4 and

Table 4.5. As expected, $\Delta T_{cat1}, \Delta T_{cat2}$ values are higher when the heat sink value is higher and the inlet temperature of the cathode air channel is lower.

Table 4.4: Temperature variations in the stack when minimum amount of energy condition applied as a heat sink.

λ	Inlet temperature of the cathode air (K)		Outlet temperature of the air (K)			Maximum to minimum surface temperature of the catalyst layers (K)		Average temperature of the catalyst (K)
	T_{Bch1}	T_{Bch2}	T_{Cout}	T_{Bch1}	T_{Bch2}	ΔT_{cat1}	ΔT_{cat2}	
10.2*	458	458	461	446	449	45	36	463
4	436	412	536	524	527	38	30	538
5	405	393	489	480	483	33	25	492
6	384	379	459	453	456	28	21	464
7	368	367	435	432	434	24	21	441
8	355	357	416	415	417	21	21	423

* Without thermal coupling with metal hydride (heat sink value is zero).

Table 4.5: Temperature variations in the stack when maximum amount of energy condition applied as a heat sink.

λ	Inlet temperature of the cathode air (K)		Outlet temperature of the air (K)			Maximum to minimum surface temperature of the catalyst layers (K)		Average temperature of the catalyst (K)
	T_{Bch1}	T_{Bch2}	T_{Cout}	T_{Bch1}	T_{Bch2}	ΔT_{cat1}	ΔT_{cat2}	
4	361	331	488	488	490	30	35	499
5	343	328	451	452	455	28	33	462
6	330	323	425	428	430	27	31	435
7	320	319	405	410	412	26	30	416
8	312	315	389	396	397	26	29	401

4.2.2 Varying current density

The current density highly influenced by temperature and it is varying along the length of the channel. The varying current density, volumetric heat source values with temperature are calculated by using equations (Korsgaard et al., 2006, 2006a; Førde et al., 2009; Scott and Mamlouk, 2009). The maximum current density of 0.42 A/cm^2 is obtained at cell temperature of 473 K and it decreases as a function of the cell temperature. The spatial variations in the heat source and local current density of the catalyst layers are shown in Figure 4.6, Figure 4.7 and Figure 4.8 and the corresponding variations in the temperature of the catalyst layer, bipolar plate channel and cooling plate channel are shown in Figure 4.9 at a stoichiometric factor of 4.84 (with a heat sink value of 0.32 W). It may be noted that Figure 4.6, Figure 4.7 and Figure 4.8 have been scaled in the z-direction by a factor of 10 in order to improve clarity. The catalyst layer-1 which is near to the cooling plate has lower surface temperature as compared to the catalyst layer-2 which is farther. The solid temperature in the middle portion of the stack is high compared to the edges of the stack because the cooling plate air, bipolar plate air are flowing in opposite direction to each other within the stack. At a stoichiometric factor of 4.84, $\Delta T_{\text{cat1}}=25 \text{ K}$, $\Delta T_{\text{cat2}}=26 \text{ K}$ and corresponding current density, heat source and the temperature variations are shown in Figure 4.9. At the entrance of the bipolar plate channel, the inlet temperature are very low due to the thermal energy taken away for the desorption of hydrogen. As the air flows through the bipolar plate from the inlet to the outlet of the channel, it gains temperature continuously up to a length of $z=0.07 \text{ m}$ (which is at a distance of 0.03 m from the edge of the cathode channel entrance) and after that the temperature in the bipolar plate channel decreases. The temperatures in the solid layers are varying by about 28 K along the flow path.

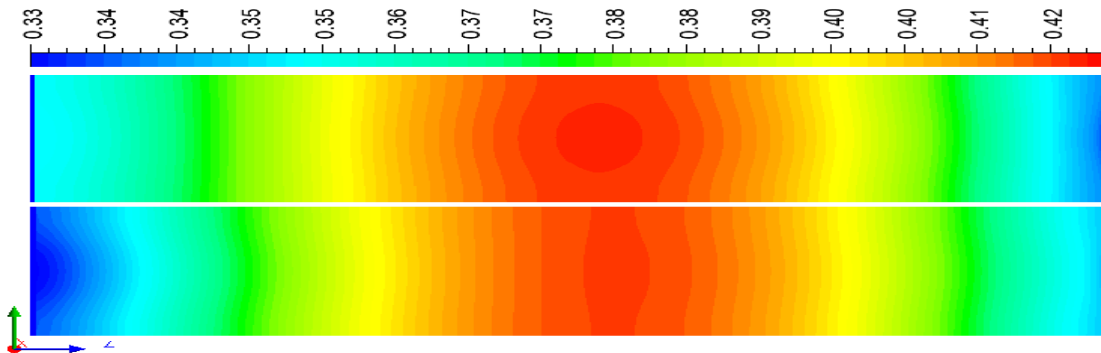


Figure 4.6: Spatial variation of the current density (A/cm^2) in the catalyst layers.

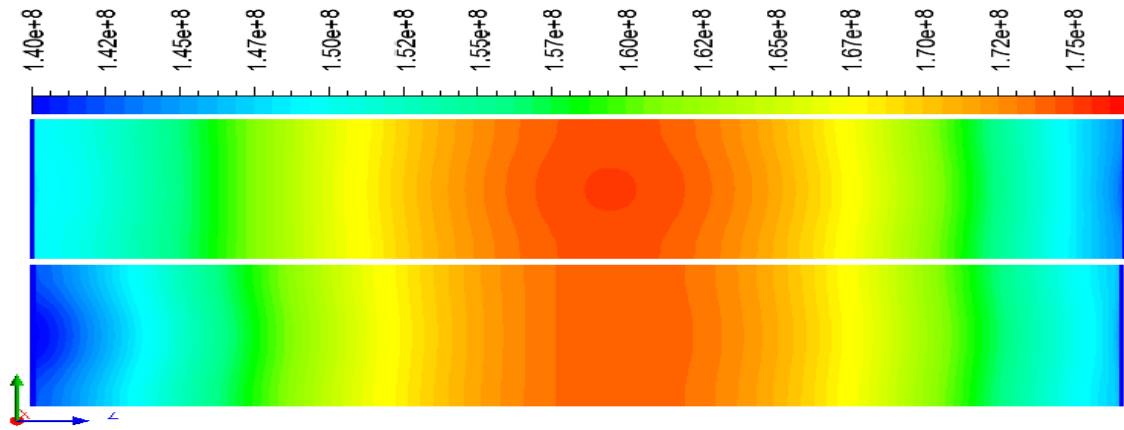
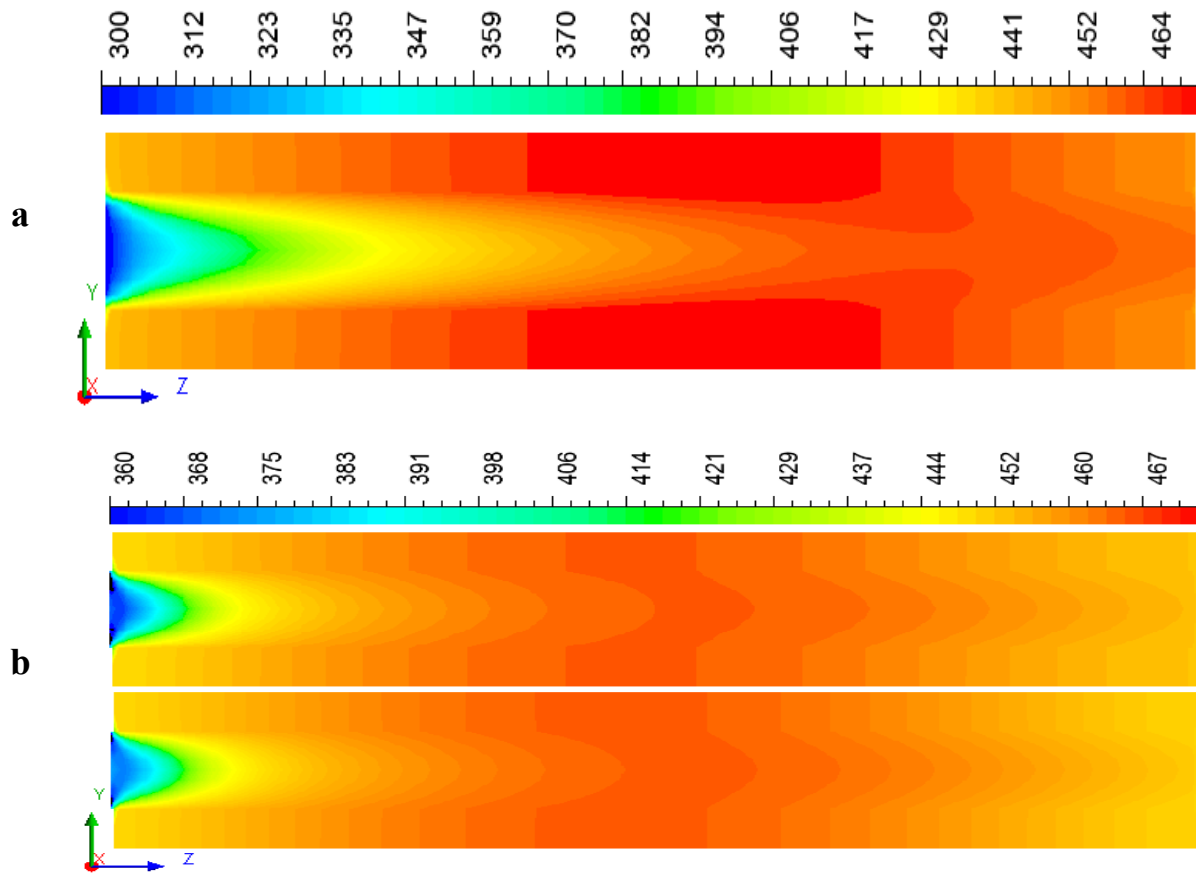


Figure 4.7: Spatial variation of heat source (W/m^3) in the catalyst layers.



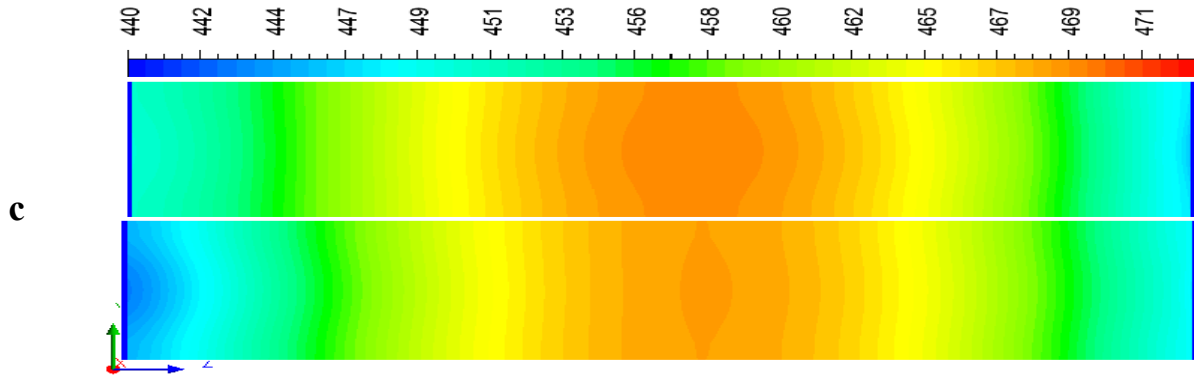


Figure 4.8: Spatial variation of the temperature (K) in the (a) cooling plate channel, (b) bipolar plate channels and (c) catalyst layers.

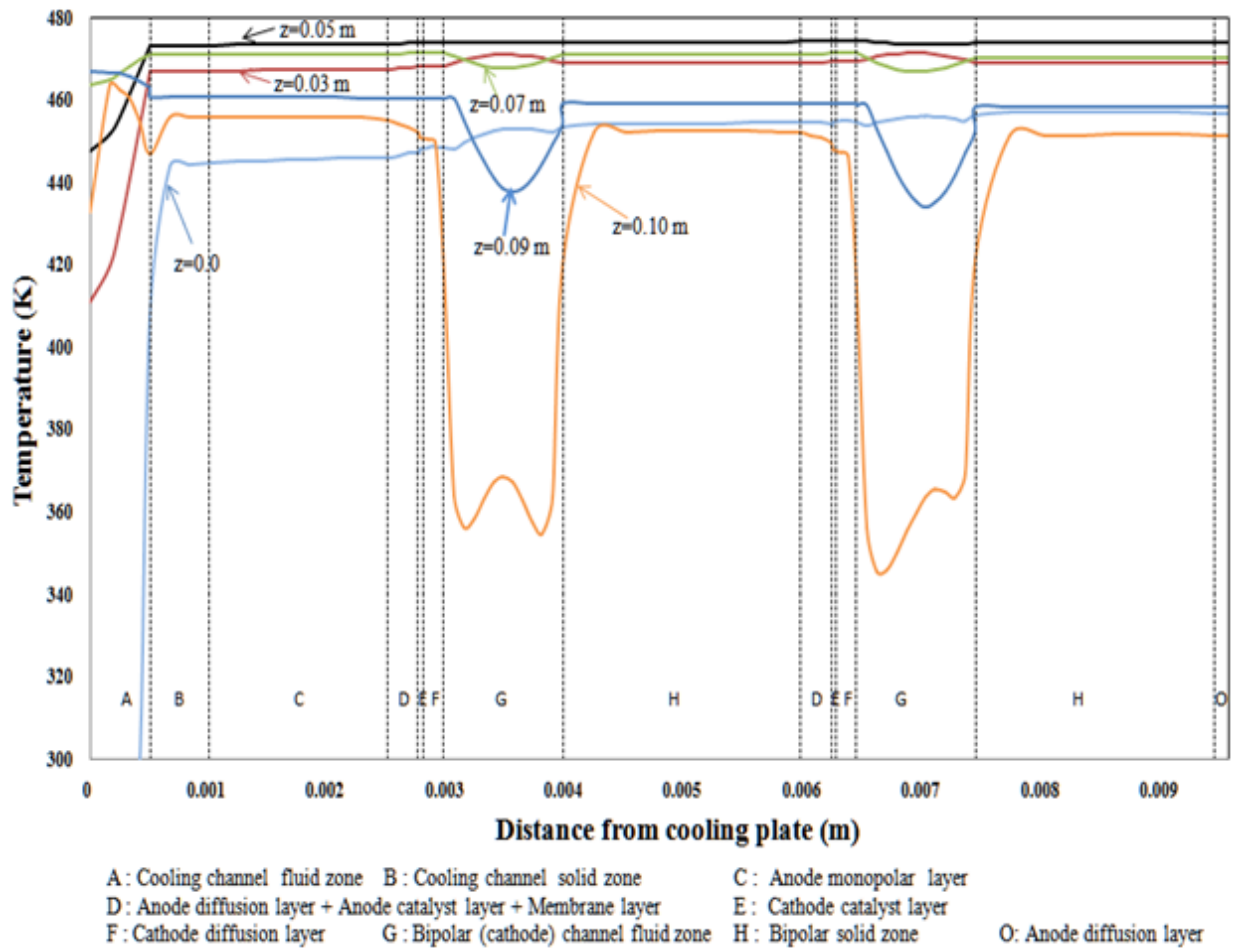


Figure 4.9: Temperature variation along the stack thickness (one half-channel cooling plate with two cells) at a $\lambda = 4.84$. Additional heat removal using coupled metal hydride storage.

The predicted temperature within the catalyst layers is in the range of 440-471 K forming a relatively hot spot in the middle of the catalyst and while the edges of the catalyst layer have a cold region. The current density on the catalyst layer is varying from the 0.33 A/cm² to 0.42 A/cm² with an average of 0.39 A/cm². The local current density value is varying by about $\pm 15\%$ from the average current density value. Thus, the extractable power decreases by about 7% from the case of uniform current density due to temperature variation over the cell.

4.3 Heat removal by forced air circulation over the stack

4.3.1 Heat removal assisted by forced convection

Since there is no liquid water formation in HT-PEMFCs, there is no pronounced mass transport-limited drop in the polarization curves at high current densities. Experimental data show that the stoichiometric factor does not have any effect on the polarization curve for current densities of up to 1 A/cm². In view of this, it is not necessary to use high stoichiometric factors and increase thereby the parasitic cost of pumping air. Thus, if stack cooling can be assisted by having a forced convection (natural circulation alone is not enough as shown in Section 3.1.4), the stack can be operated at lower stoichiometric factors. This can be readily induced in a transport application by directing the ambient air to flow over the cell when the vehicle is moving. In order to study this possibility, the computational domain shown in Case C (Figure 3.4) is used. As noted earlier, forced circulation may introduce large temperature variations within the cell and the objective of these simulations is to estimate how much external air cooling is required. Noting that the temperature gradients within the cell are very small if cooling is achieved by passing air through the cooling plate and the cathode flow fields (Figure 3.1), the effect of cathode air cooling is represented in Case C simulations by reducing the heat generation rate appropriately. This enables the computational domain to be divided into two regions, one of high thermal conductivity (20 W/m K corresponding to the region occupied by the bipolar plates and the cooling plate and the other having low thermal conductivity (1.5 W/m K) consisting of the membrane, the catalyst layers and the GDLs. The total heat generation rate (which is now reduced by an amount equal to sensible heating of the cathode air) is distributed uniformly over the MEA. The temperature distribution over this composite material plate is calculated subject to a specified convective heat transfer coefficient and with an ambient temperature of 303 K.

Typical results obtained from these calculations are shown in Figure 4.10 for two convective heat transfer coefficients, namely, 37 and 50 W/m² K for an air stoichiometric factor of 3. It can be seen immediately that the temperature in the core region is higher, by about 20 to 30 K, than the sides through which heat is being removed. The results from such calculations, performed for a range of stoichiometric factors, are summarized in Table 4.6 which shows the maximum and the minimum surface temperatures as a function of the stoichiometric factor and the convective heat transfer coefficient. Also shown in the table is the estimated air velocity required to achieve the specified heat transfer coefficient. This is obtained by modeling the stack as a rectangular block and using the following correlation for heat transfer in cross-flow of air over it (Holman, 1986):

$$\text{Nu} = 0.14 \text{Re}^{0.66} \quad (4.4)$$

Here Nu is the Nusselt number defined as hD/k where h is the convective heat transfer coefficient, D is the hydraulic mean diameter and k is the thermal conductivity and Re is the Reynolds number defined as UD/ν where U is the free stream velocity and ν is the kinematic viscosity. It can be seen from the table that for a given stoichiometric factor, as the convective heat transfer coefficient increases, the maximum temperature (T_{core}) decreases. Also, the difference between the core temperature (T_{core}) and the surface temperature (T_{surf}) decreases. Both these effects are as expected; what is perhaps surprising is that in spite of the relatively high thermal conductivity of graphite, the temperature difference can be as much as ~30 K. The table also shows that as the stoichiometric factor increases, the core temperature as well as the temperature difference between the core and the surface decreases. However, it may be noted that the simulation in Case C does not consider the temperature variations caused by the cooling air entering at 303 K which is shown to induce up to 50 K variation in the cell temperature.

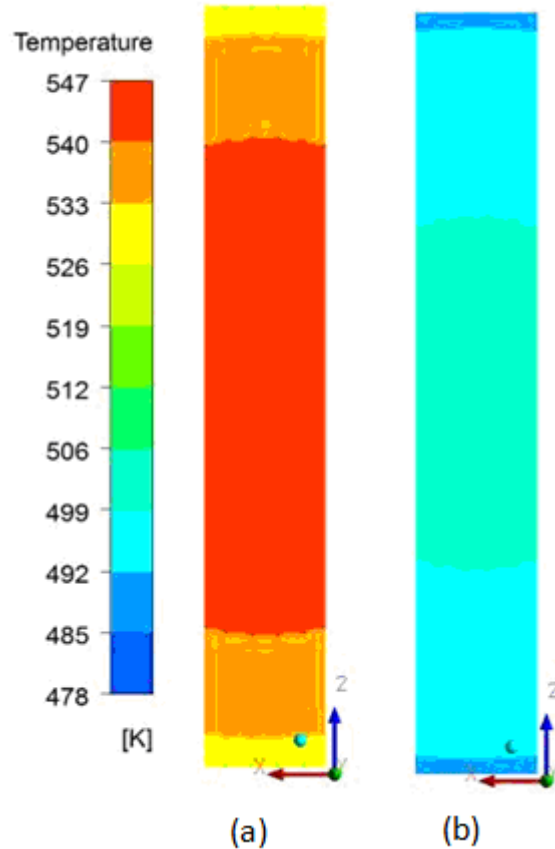


Figure 4.10: Temperature (K) contours for external flow and coolant flow in channel with a convective heat transfer coefficient of (a) $37 \text{ W/m}^2 \text{ K}$ and (b) $50 \text{ W/m}^2 \text{ K}$

The implications of these results on the operation of the stack are as follows. In the external convection-assisted case, the designer will have the option of running the cell at a high stoichiometric factor or with a high convective heat transfer coefficient to maintain the cell temperature within reasonable limits. In a transport application, the estimated free stream air velocity required to provide the heat transfer coefficient listed in Table 4.6, may be related to the speed of the moving vehicle. The present study shows that when the vehicle is stationary, it may be necessary to use a high stoichiometric factor to keep the engine cool while at high speeds, say, of the order of 60 km/h (i.e., 16.7 m/s) which corresponds to an h value of $75 \text{ W/m}^2 \text{ K}$ in Table 4.6, a stoichiometric factor of two is sufficient to maintain cell temperatures to within 200°C .

Table 4.6: Minimum and maximum temperature of the stack in Case C.

λ	h=25 W/m ² K (U=3.1 m/s)		h=37 W/m ² K (U=5.6 m/s)		h=50 W/m ² K (U=8.9 m/s)		h=75 W/m ² K (U=16.4 m/s)		h=100 W/m ² K (U=25.4 m/s)	
	T _{surf} (K)	T _{core} (K)	T _{surf} (K)	T _{core} (K)	T _{surf} (K)	T _{core} (K)	T _{surf} (K)	T _{core} (K)	T _{surf} (K)	T _{core} (K)
1	795	837	630	672	541	583	456	498	414	455
2	732	769	588	625	510	547	436	473	400	435
3	670	701	547	578	480	511	417	448	386	416
4	607	634	505	532	450	476	398	423	371	397
5	545	566	464	485	420	441	378	398	358	378
6	482	497	422	438	389	405	359	374	343	358

4.3.2 Heat removal by forced convection alone

It can be seen from the results of Sections 4.1.1 and 4.1.2 that fairly large temperature differences, of the order of 50 K, are created within the cell due to the feeding of the air into the cooling plate at 303 K. Results from Section 4.3.1 show that forced convection at an air velocity in the range of 16 to 25 m/s introduces a temperature variation of only ~20 K in the cell. Thus, one way of reducing temperature variations within the cell would be not to use cathode air for cooling at all; forced convection alone could be used to effect the cooling. This case is simulated by performing the calculations for the computational domain shown in Figure 3.4 with a heat generation term corresponding to a stoichiometric factor of zero, i.e., without considering the cooling coming from the preheating of air from 303 K to 473 K. The results of calculations for different convective heat transfer boundary conditions are shown in the first row of Table 4.6. It can be seen here that the core temperature is at an acceptable value of 474 K only at a convective heat transfer coefficient of 100 W/m² K corresponding to an air velocity of 25 m/s. However, at this condition, the minimum temperature in the cell is 428 K, i.e., again a temperature difference to 46 K. Increasing the heat transfer coefficient further to 150 W/m² K reduces this temperature slightly to 45 K but also reduces the core temperature to 427 K which is well below the target cell operating temperature of 473 K. Thus, it appears that temperature differences of the order of 50 K over the entire cell are inevitable with any of the three strategies considered here. However, over most of the region, the variation may be only of the order of 20 K.

4.4 Heat removed by liquid coolants

4.4.1 Coolant medium

Liquid coolants have much higher heat capacity than gas coolants, which makes them more efficient for cooling applications. At the same, it also requires an additional pumping system and additional pre-heating of the cathode air and fuel needed. A liquid cooled stack has high start-up times compared to the air-cooled system (Andreasen et al., 2008). Water as a coolant has the disadvantage that its use can be restricted to a maximum of 373 K. Calculations already presented in Figure 4.12, for example, showed that at such low coolant temperatures, the average current density is significantly less than the nominal value obtained assuming a cell operating temperature of 473 K. Indeed, this was confirmed by calculations which showed 10 to 15% drop in the power output compared to the case of thermal coil. Therefore, a coolant medium capable of being heated up to stack temperature without inducing phase change should be used as the coolant. Therefore, the results obtained only with Duratherm oil as the coolant its thermal physical properties are given in Table 4.7 are discussed here.

Table 4.7: Properties of Heat transfer oil (Duratherm).

	Duratherm heat transfer oil (at 303 K)	units
Density, ρ	850	kg/m ³
Specific Heat, C_p	2135	J/kg K
Thermal conductivity, k	0.14	W/m K
Kinematic viscosity, ν	0.045	m ² /s

4.4.2 Heat removed by heat transfer oil

Typical variation of the predicted temperature in a y-z plane (see Figure 3.5) passing through the mid-channel height is shown in Figure 4.11 for the case of a stack operating at a cell voltage of 0.6 V and with the coolant entering at 400 K. The length in the y-direction has been magnified in the figure to show the variation clearly. The coolant oil enters, at a temperature of 400 K in this case, the flow domain through the (half-) channel on the bottom right hand corner of the figure and leaves at the top right hand corner. Cathode air enters from the top at temperature of 300 K

through two channels and leaves the domain at the bottom. The temperature distribution in the plane is affected primarily by the heat generated in the two catalyst layers and its removal by the two air streams and the coolant. It can be seen that although the cathode air enters at 300 K, it gets heated up very quickly and its subsequent role in further heat removal is minimal. The bulk of the cooling is carried out by the coolant; the principal temperature gradients in the cell occur as a result of the coolant getting heated up. These observations can be clearly seen in Figure 4.12 where the temperature profiles across different layers (such as those belonging to the resolved layers of the two cells and one half of the cooling channel) are shown at different distances in the coolant flow (z -) direction. It can be seen that at any given value of z , except near the coolant entry and near the cathode air entry, the temperature variation is fairly uniform. A large temperature variation, amounting up to about 145K is present within the two cathode air entry channels, corresponding to the profile at $z = 0.10$ m. However, the temperature variation within the adjacent catalyst layers and the graphite plates is very small. Also, the variation for $z = 0.07$ m is also very little. Much of the variation, amounting up to nearly 45 K within the catalyst layers, occurs due to the variation of the temperature of the coolant. However, increase in the coolant inlet temperature 450 K may reduce the temperature variation within the cell (but not in the coolant or cathode air channels) at any z , is within 11 to 14 K.

The above observations are reinforced by an examination of Figure 4.13 which shows the predicted temperature distribution in the mid-thickness of the catalyst layer of the second cell (which is furthest from the cooling channel) for a cell operating at a voltage of 0.6 V. Here, the predicted temperature contours are shown for three coolant inlet temperatures, viz., 300, 400 and 450 K. It can be seen that the temperature varies primarily in the coolant flow direction, i.e., from the left to the right in the figures; there is some but fairly little variation in the catalyst layer the y -direction that is attributable to the cathode air entry at 300 K. Thus, as shown in Figure 4.11 and Figure 4.12, the temperature variation attributable to the cathode air is small and localized in HT-PEMFCs. The z -directional temperature change is primarily due to the change in the coolant temperature; the higher the coolant temperature (as in Figure 4.13c), the lesser is the temperature variation.

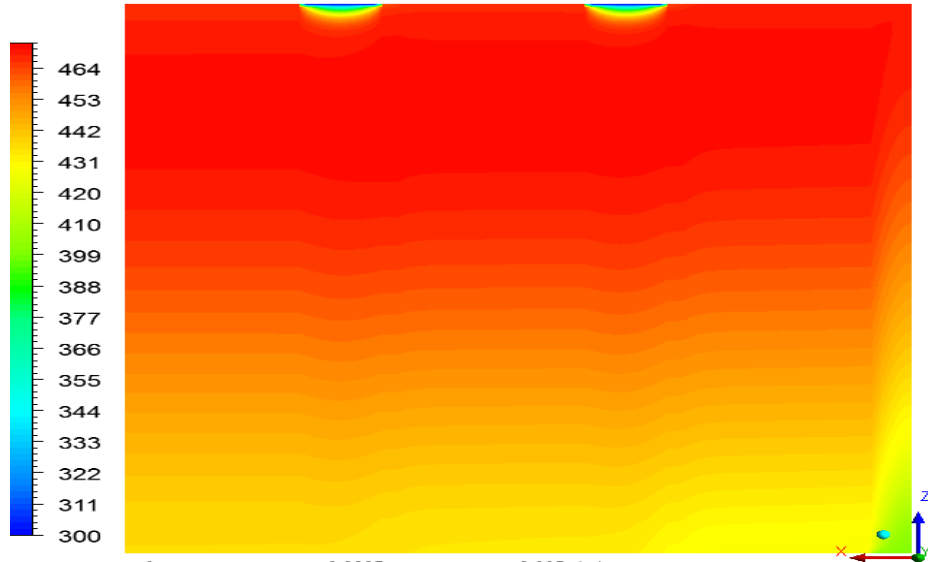


Figure 4.11: Temperature contours of cell layers in two cells and one half-channel of the cooling plate ($T_{Cin} = 400 \text{ K}$; $i_{avg} = 0.374 \text{ A/cm}^2$; $V_{cell} = 0.6 \text{ V}$ and $\lambda = 1$).

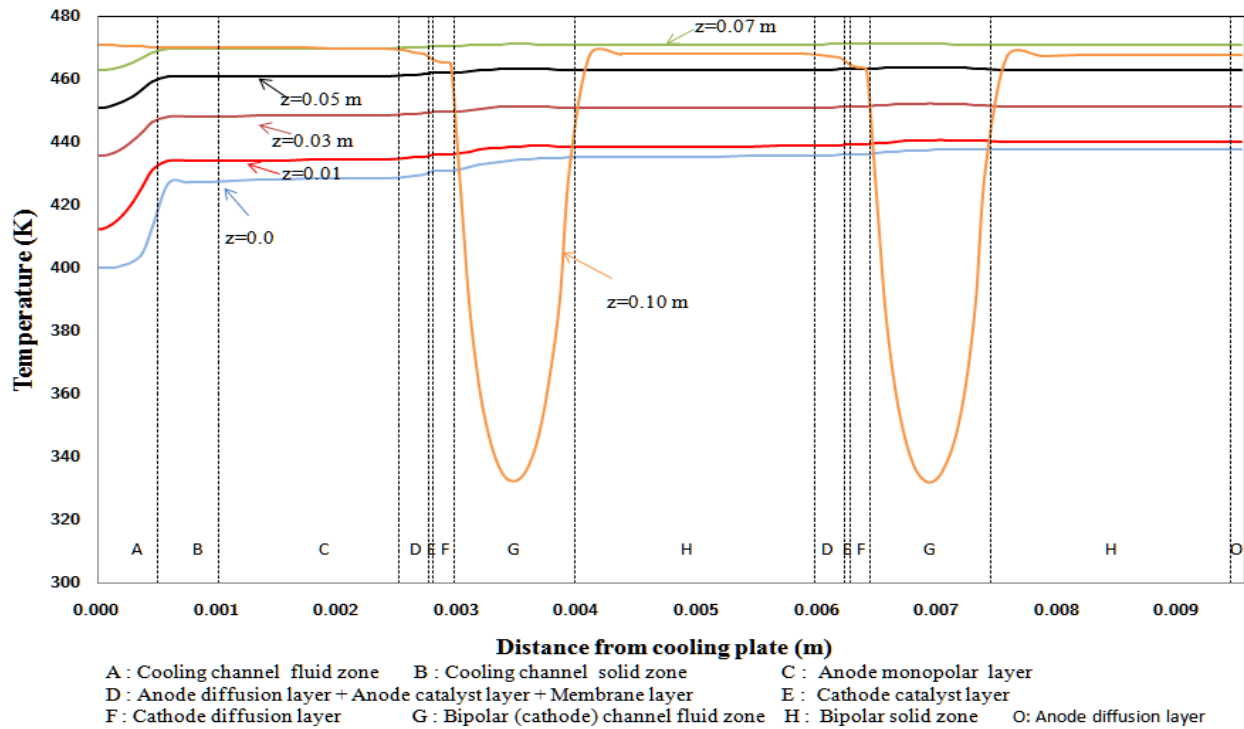


Figure 4.12: Temperature profiles along the stack thickness of two cells and one half-channel of a graphite cooling plate material ($T_{Cin} = 400 \text{ K}$; $i_{avg} = 0.374 \text{ A/cm}^2$; $V_{cell} = 0.6 \text{ V}$ and $\lambda = 1$).

The effect of the temperature distribution on the local current density is illustrated in Figure 4.14 which shows the computed local current density on the catalyst layer for the three cases. Considerable variation in the local current density can be observed when the coolant enters at temperatures much less than the operating temperature of the cell. The cell-averaged current density is significantly reduced when the coolant enters at low temperatures.

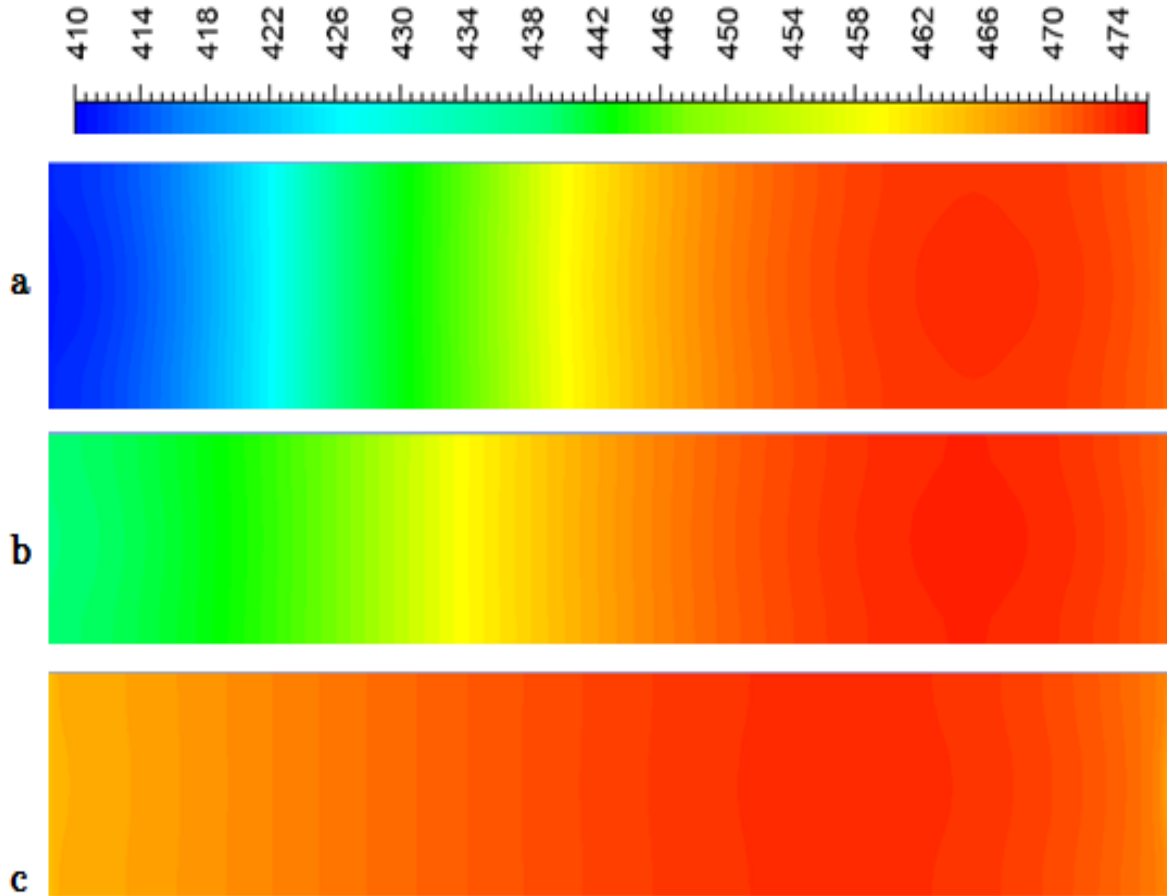


Figure 4.13: Spatial variation of the temperature (K) in the CCL-2 at a coolant inlet temperature of (a) 300 K, (b) 400 K and (c) 450 K ($V_{\text{cell}} = 0.6 \text{ V}$; $\lambda = 1$ and graphite as a cooling plate material).

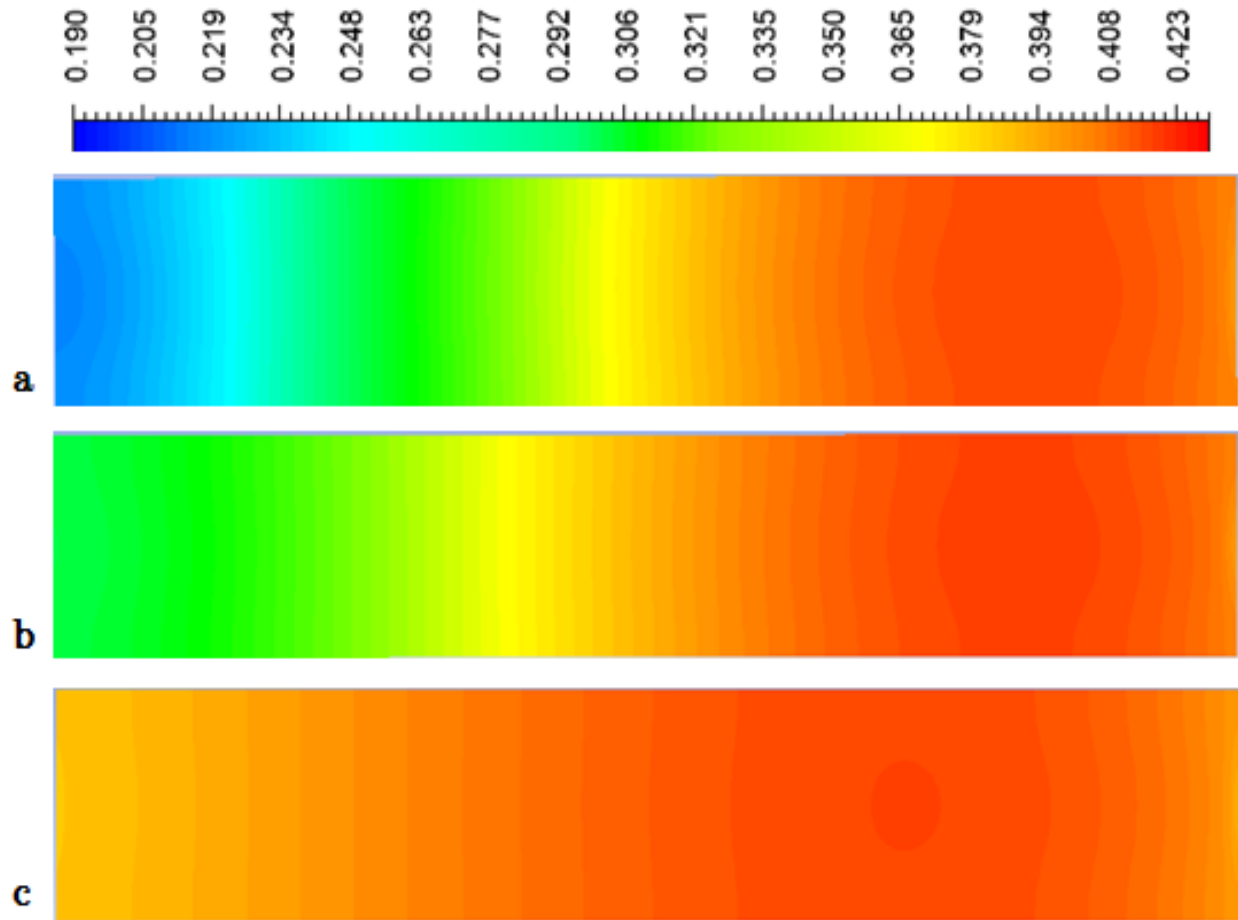


Figure 4.14: Spatial variation of the current density (A/cm^2) in the CCL-2 at a coolant inlet temperature of (a) 300 K, (b) 400 K and (c) 450 K ($V_{cell} = 0.6$ V; $\lambda = 1$ and graphite as a cooling plate material).

4.5 Parametric studies

A number of considerations arise in designing an effective thermal management system for the stack. In addition to meeting requirement of not exceeding the permissible upper limit on the temperature from a materials point of view, it is also necessary to maintain a high average temperature in order not to have a penalty on the power output. If, in order to increase the average temperature, the coolant inlet temperature is increased, then the coolant flow rate through the stack will have to be increased resulting in increased pressure losses. The thermal conductivity of the cooling plate itself is a parameter. Use of copper or aluminum plates may prove to be advantageous due to their higher thermal conductivity. On the other hand, a graphite

cooling plate may allow the cooling channels to be embedded into the flow field and may thus avoid contact thermal resistances. Finally, the number of coolant plates per stack is also a possible parameter as the coolant plates will add to the weight of the stack. In order to investigate these possibilities and assess the advantages or penalties associated with each measure, a number of CFD simulations have been carried out to investigate the following cases:

- Cathode air stoichiometric factor : 1, 2 or 3
- Operating voltage : 0.5 or 0.6 V
- Number of coolants plates: one for every four or six cells
- Cooling plate material: copper, aluminum or graphite
- Coolant inlet temperature : 300 to 450 K
- Coolant inlet flow rate

The results from these calculations are summarized in flowing sections.

4.5.1 Cathode air stoichiometric factor

It is usual to operate the cathode at a stoichiometric factor greater than unity, i.e., the air flow rate is higher than what is required, as per stoichiometry, for the oxygen consumption in the electrochemical reaction at the operating current. As far as thermal management is concerned, a higher stoichiometric factor enables more amount of heat to be taken away by the cathode air and therefore the load on the coolant system will become less. In the present calculations, this is reflected in reduced mass flow rates of the coolant and as a result the coolant heats up quickly. This has a beneficial effect because it is the heating up of the coolant that is the main cause of the temperature variation on the catalyst layers as demonstrated in Figure 4.12. A higher stoichiometric factor and a lower coolant flow rate would tend to increase the average cell temperature. There is a secondary and opposite effect of high stoichiometric factor: since air enters the cell without any preheating (as assumed in the present study), higher air flow rate would require higher amount of heat pick-up from the cell to bring it up to the cell temperature. This has the tendency to reduce the average cell temperature. For a given case, the net effect of these two factors defines the overall effect on the current density. This is reflected in Table 4.8 which shows the relevant parameters gleaned from the simulations for two stoichiometric factors

and three coolant entry temperatures for a cell operating at 0.5 V. In all cases, the cathode air is assumed to enter at a temperature of 300 K. The tables lists the predicted outlet temperatures of the coolant and the air through the cathode flow fields as well as the minimum and the maximum temperature (which is set at 473 K) and the volume-averaged temperature of the two cathode catalyst surfaces, the mass flow rate through one-half of the coolant channel and finally the average current density. It can be seen that when the coolant enters at ambient temperature, there is an appreciable increase in the volume-averaged catalyst (cell) temperature resulting in a higher current density when the stoichiometric factor is higher. When the coolant enters at close to the cell operating temperature, then the coolant temperature rise is so small (5 to 6 K) that it hardly makes a difference to the current density (and therefore the power output). However, as can be seen from the table, the mass flow rate of the coolant is reduced by about 30% when the stoichiometric factor is increased from 1 to 3 which should result in less pressure drops in pumping the coolant.

Table 4.8: The temperatures variations in the stack at $V_{\text{cell}} = 0.5$ V and heat transfer oil as a coolant for different stoichiometric factors of the cathode air.

Coolant temperature (K)		Cathode air			Maximum surface temperature of CCL (K)		Minimum surface temperature of CCL (K)		Volume average temperature of CCL (K)		$m_c \times 10^6$ (kg/s)	i_{avg} (A/cm ²)
		λ	Outlet temperature (K)									
T_{Cin}	T_{Cout}	Inlet	T_{Beh1}	T_{Beh2}	ccl-1	ccl-2	ccl-1	ccl-2	ccl-1	ccl-2		
300	469	1	374	380	472	473	366	377	432	435	3.4	0.56
300	465	3	387	395	472	472	377	390	442	444	3.3	0.63
400	462	1	429	434	471	473	425	432	454	457	13.0	0.73
400	457	3	440	445	471	473	432	442	458	461	11.1	0.76
450	456	1	462	465	469	472	458	458	465	469	246	0.83
450	455	3	464	467	470	473	447	441	465	467	170	0.83

4.5.2 Operating voltage

The operating voltage has a significant effect on the power density. As per the empirical V-I curve of the cell, the current density is 0.42 A/cm² when the operating voltage is 0.6 V and it is 0.90 A/cm² when it is operated at 0.5 V, giving an increase of 42% in the power density when the

voltage is decreased from 0.6 to 0.5 V. Steady state simulations have been carried out for both operating conditions over a range of coolant inlet temperatures and stoichiometric factors and the results are summarized in Table 4.9. Here, the difference between the maximum and the minimum temperature on the first and the second cathode catalyst layers, the average cell current density and the temperature rise in the coolant are given. The mass flow rate of the coolant is varied to meet the different power, and hence, the thermal, output in the two cases. It can be seen that higher temperature variations are found over the catalyst layers for higher operating power. As a result, the average current density deviation from the nominal current density is higher resulting in more losses when the cell is operated at the higher power density. When the coolant inlet temperature is increased to 450 K, the drop in the power from the nominal value is about 4% for cell operation at 0.6 V and 8% for cell operation at 0.5 V. As far as the coolant is concerned, the outlet temperatures are not very different in the two cases; however, much higher coolant flow rates are required for the latter case as the thermal load on the coolant is high.

Table 4.9: The temperatures variations in the stack at cell voltage of 0.6 V and 0.5 V, heat transfer oil as a coolant and graphite as a cooling plate.

T_{Cin} (K)	λ	$V_{Cell} = 0.6 \text{ V}$				$V_{Cell} = 0.5 \text{ V}$			
		ΔT_{Cat1} (K)	ΔT_{Cat2} (K)	i_{avg} (A/cm ²)	ΔT_{oil} (K)	ΔT_{Cat1} (K)	ΔT_{Cat2} (K)	i_{avg} (A/cm ²)	ΔT_{oil} (K)
300	1	71	60	0.351	170	107	96	0.555	168
300	2	64	52	0.363	166	95	82	0.627	165
300	3	51	39	0.378	159	82	67	0.682	158
400	1	42	37	0.374	70	46	41	0.726	61
400	2	38	32	0.383	68	42	36	0.752	60
400	3	35	28	0.386	63	38	31	0.763	57
450	1	11	13	0.404	16	11	14	0.837	6
450	2	12	15	0.405	16	17	24	0.829	6
450	3	17	21	0.405	14	22	32	0.825	5

4.5.3 Number of cooling plates

The presence of a cooling plate increases the weight of the stack. If one cooling plate is used for each cell, then the cooling plates themselves may weigh as much as the flow fields, which

themselves contribute to nearly 80% of the weight of the stack. In view of this, we have considered two possibilities in the present study: one cooling plate for every four cells and one for every six cells. Since the computational domain consists of one-half of the coolant channel and one half of the number of cells per coolant channel, in the first case, the computational domain contains of two cells (and hence two cathode catalyst layers, which is where most of the heat is produced), while in the second case, there will be three cells per coolant channel. This has the effect of increasing the distance between the last cell and the coolant channel which will have a tendency to increase the temperature drop resulting in a lesser cell temperature. There is also the counter-effect of increased mass flow rate of the coolant (because each coolant channel must remove the heat produced in six cells), which should help in more effective heat removal as far as the first two channels are concerned. At the same time, the net heat flux passing through these cells is higher. The net result of all these considerations is that the temperature variations over the catalyst layers (the difference between the maximum and the minimum temperature on each catalyst layer) are higher when there are six cells for every coolant channel than when there are four cells for every coolant channel. Specifically, for the case when the coolant enters at 400 K, the temperature variations in the first and second catalyst layers is 39 and 31 K respectively for four-cells per coolant plate case and 31 and 43 K, respectively for the six-cell per coolant channel case. The third catalyst layer, the one farthest from the coolant channel in the latter case, has a temperature variation of 51 K over its surface. The volume-averaged current density at the operating voltage of 0.5 V is less by about 2% in the six-cells per coolant channel case. In this sense, it appears that the difference between the two cases is not much. However, it is found that it would not be possible to operate the six-cells case with a higher coolant inlet temperature. Thus, the maximum current density possible with six-cells case would be 0.75 A/cm² corresponding to a coolant inlet temperature of 400 K while a four-cells per coolant channel could be operated at a coolant inlet temperature of 450 K resulting in an average current density of 0.83 A/cm²(see Table 4.9), resulting in an effective reduced power density of nearly 10%. The pressure drop in the coolant channel would also be higher due to the higher mass flow rate.

4.5.4 Cooling plate material

From the thermal management point of view, the material of the coolant plate should have high thermal conductivity to reduce the temperature gradients while being light-weight at the same time so that the additional weight of the cooling plates can be minimized. In order to evaluate these effects, calculations have been done for three materials, namely, copper, aluminum and graphite. It may be noted that the thermal conductivity of copper is 350 W/m K while that of graphite is 20 W/m K. The thermal conductivity of aluminum is about half of that of copper but its density is about one-third. In the calculations, it is assumed that one coolant channel is placed for every four cells and that the cells are operated at a voltage of 0.5 V. The results obtained from these are summarized in Figure 4.15 where the average current density is plotted as a function of the coolant inlet temperature and the stoichiometric factor for copper and graphite. It can be seen that for low coolant inlet temperatures, there is a considerable difference in the computed average current density indicating that there would be a significant power density advantage in using copper as the coolant plate material. However, when the coolant inlet temperature is 450 K, the power density penalty is only about 2%, enough perhaps to rule out copper based on weight considerations.

4.5.5 Specific power density and optimal configuration for a 1 kWe stack

The results from the above sections are summarized in Table 4.10 for a 24-cell HT-PEMFC stack operating at a cell voltage of 0.5 V with one coolant channel for every four cells and with cathode air entering at 300 K. The volume-averaged current density is used to calculate the power for cooling plates made of copper, aluminum and graphite. The cathode air stoichiometry and the coolant (thermal oil) inlet temperature are kept as variables. The power density is computed by dividing the power produced by the stack by the weight of the flow fields, the cooling plates, the MEA and two end plates. Thus, the calculation is based only on the “active” volume of the stack from a heat transfer and electrochemistry point of view and does not include the essential supplementary volume (and weight) needed for ducting manifolds for the various streams, thermal and electrical insulation etc. It can be seen that when significantly lower power output is obtained due to cell temperature (and the consequent current density) variations when the coolant temperature is low. At these conditions, the stack with copper plates produces signif

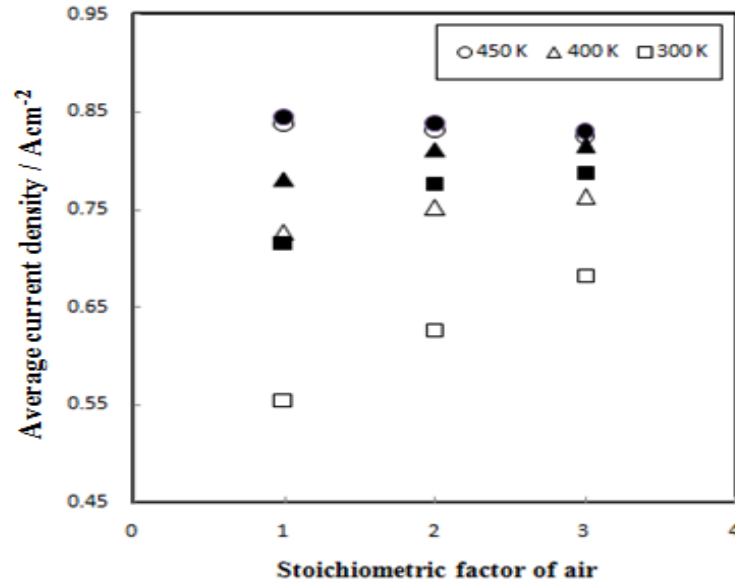


Figure 4.15: The average current density as a function of T_{cin} , λ and the material of the cooling plate (solid symbols for copper, and hollow symbols for graphite) at a $V_{\text{cell}}=0.5$ V.

significantly higher power. However, when the coolant inlet temperature is 450 K, the power output is close to 1 kWe in all the three cases. However, due to the significantly higher density of copper, the power density, expressed in W/kg, is lower for the copper coolant-plated stack by about 30% compared to that of graphite cooling plates in which case a specific power density of 690 W/kg is obtained. Similar calculations for operating voltage of 0.6 V confirm that if the coolant inlet temperature is maintained sufficiently high, then a stack with graphite coolant plates will produce nearly the same power as that with copper but enjoys a 30% higher specific power density.

Stack-level simulation of temperature distribution has been made using a small unit the HT-PEMFC stack as the computational unit. The simulation focuses primarily on the cell-to-coolant plate heat transfer and therefore simplifies many of the details that are not relevant to heat transfer. A coupling with the electrochemistry is made through a simple, empirical polarization curve. The following specific conclusions can be drawn from the large number of CFD simulations of the heat transfer for the case of the externally-cooled HT-PEMFC stack:

Table 4.10: Specific power density variations for different coolant inlet temperatures in the stack at cell voltage of 0.5 V (for 24 cells).

T _{Cin} (K)	λ	Specific power density (W/kg)			Electrical power from stack (W)		
		Graphite	Aluminum	Copper	Graphite	Aluminum	Copper
300	1	463	534	406	666	806	860
300	3	570	613	447	819	926	946
400	1	607	605	443	872	912	938
400	3	637	629	463	916	950	979
450	1	699	669	479	1002	1006	1011
450	3	689	658	471	990	994	996

4.6 Summary

Stack-level simulation of temperature distribution has been made using a small unit the HT-PEMFC stack as the computational unit. The simulation focuses primarily on the cell-to-coolant plate heat transfer and therefore simplifies many of the details that are not relevant to heat transfer. A coupling with the electrochemistry is made through a simple, empirical polarization curve. The present CFD simulations of the flow and the temperature field within the stack of a 1 kWe HT-PEMFC have given a temperature mapping over a cell under various operational strategies. The following conclusions can be drawn from this study: The calculations have been carried out for air, water and Duratherm heat transfer oil as the coolant.

4.6.1 Integrated air cooling

- It is possible to use the cathode air supply to also serve as a coolant to keep the cell temperatures low. However, a large stoichiometric factor, of the order of 10, is required to maintain cell temperatures of $\sim 200^{\circ}\text{C}$ without forced convective cooling. For transport applications, where the stack is mounted on a moving vehicle, the required external cooling can be achieved by directing the ambient air to flow over the stack. In such a case, the stack can be operated at a reduced stoichiometric factor.
- There can be about 15% deviation in the local current density from its mean value due to the variation in the temperature across the catalyst layer. This has the effect of reducing the maximum power that can be drawn from a given fuel cell. Achieving more uniformity

in the temperature, through proper thermal management, is therefore necessary to extract the maximum power from an HT-PEMFC.

4.6.2 Coupling thermal management with H₂ storage tank

- The amount of heat produced from the 1 kWe stack at a voltage 0.6 V is approximately three times higher than the amount heat required for NaAlH₄ to desorb hydrogen from the metal hydride.
- The calculations shows that, with a cathode air flow rate seven times in excess of the stoichiometric requirement, it is possible to meet the triple requirement of supplying preheated cathode air if stack is assumed running at constant current and constant voltage.
- When the local current density variation across the catalyst layer is considered, the stoichiometric factor of air gets reduced to 4.84. The combination of thermal management HT-PEMFC, metal hydride with using air thus appears viable.

4.6.3 External air flow over the stack

- Too high an air draft may reduce the cell temperatures significantly to well below the desired operating temperature of the cell; a combination of cathode air cooling and induced draft may be the right choice in a transport application.
- With proper cooling strategy, the temperature variations within the cell may be reduced to about 20 K over most of the cell and to about 50 K in isolated spots.

4.6.4 External cooling with heat transfer oil

- HT-PEMFCs require external cooling flow cell temperature variation is to be maintained. Operating with (Duratherm heat transfer oil) as an external coolant enables a higher coolant temperature and it is clearly the most superior of the three coolants (air, water, heat transfer oil).
- Temperature variations within the cell may be restricted to about 10 K by sending a liquid coolant (such as the thermal oil) with an inlet temperature close to the stack operating temperature.

- Significant variations of the local current density may arise if a near-uniform cell temperature is not maintained. Since there is an upper limit on the permissible temperature within in the cell, this may result in significant reduction (in the range of 10 to 25%) in the average current in the stack.
- While copper coolant plates do give advantage in terms of higher average current density, the difference becomes negligible in a thermally well-managed stack with coolant plates made of graphite.

CHAPTER-5

OPTIMIZATION OF THE STACK COOLING SYSTEM

5.

The HT-PEMFCs are well suited for transport applications such as scooters, cars and heavy trucks due to their zero emission exhaust and the possibility of auto-thermal on-board fuel reforming which allows a wider choice of fuel (Ahluwalia, 2007; Ahluwalia et al., 2011). Scooters require in the power range of 0.3-1 kWe while cars required 7-100 kWe (Barbir, 2005). The electrical power output from a stack can be increased either by increasing the number of cells, or by increasing the active area of each cell, or by using a modular construction of stacks of small size. Having a large number of cells may demand more mechanical strength from the cell materials as more compression is required to ensure leak proofing, the tie rods become longer and weight of the other accessories will also increase. Increasing the active cell area poses thermal management problem; the uniform distribution of reactants may also become an appreciable problem. Due to the wide range of power needs in transportation applications, fuel cells need to be redesigned and optimized for each power range and driving demands.

In the present chapter, we focus on the thermal management of HT-PEMFC stacks with varying stack sizes, specifically on the effect of fuel cell stack size on the temperature distribution within the stack as well as in the cell layers. The effect of various operational and design parameters on the net power output from the stack is studied based on the thermal models described in earlier chapters. The very practical question of how to supply the reactants to the cells and the parasitic power consumed, i.e., the design of the flow fields, is also addressed. To this end, a large number of computational fluid dynamics simulations have been carried out for various flow and cell operating conditions and stack sizes to look for optimal conditions in which maximum output from the stack can be obtained without the local temperature exceeding 473 K in the cathode catalyst layer.

The organization of the present chapter is as follows. The calculations in Chapter 4 have focused on the temperature and current density assuming uniform distribution of the reactants. In Section 5.1 and Section 5.2, the design of flow fields on the bipolar plates is considered in order to achieve uniform reactant distribution without excessive parasitic pressure losses. The calculations in Chapter 4 also bring out the importance of the cooling plates in maintaining high

average current densities. In Section 5.3, the design of flow fields for the cooling plates is considered. This is followed in Section 5.4 with an estimate of the pressure losses in the upstream and downstream manifolds for the reactants, products and the coolants. The implications of increasing the cell area for increased power from the stack is considered in Section 5.5 and a design is proposed for individual stacks units delivering up to 10-15 kWe with an active cell area of 30 cm × 30 cm. A summary of the chapter is given in Section 5.6.

5.1 Design of flow fields

The prime concern about flow fields is the pressure drop exerted by flow field which should not be high compared to electrical power output. Careful design of the cooling plate and the bipolar plates is needed in order to reduce the parasitic pumping powers. Uniform distribution of the reactants throughout the gas distributor plate is another essential feature of the reactant flow field. Non-uniform distribution of coolant/reactants may lead non-uniform temperature distribution across the cooling plate and also within the cell layers leading to the creation of local hot or cold spots which are also undesirable from the point of durability of the stack. The flow distribution in the bipolar plate depends on the number of factor such as the inlet and the exhaust header dimensions, channel geometry and cell dimensions. The temperature distribution in the stack also depends on the cooling plate, bipolar plate, flow rates, type of coolant and inlet temperature of coolant/reactants etc. These aspects are addressed below with specific focus on the flow fields for the bipolar plates.

5.2 Flow fields for the reactants

The performance of a fuel cell is sensitive to the flow rate of the reactants and each cell active area in a stack has to receive uniform amount of reactant gases. The flow field are may be square, rectangular, circular, hexagonal, octagonal or irregular, the most common shapes being square or rectangular. The flow field orientation may be either vertical or horizontal. The orientation of flow filed may have some effect on the liquid water removal during the shutdown of the stack. There are many configurations of reactant channels that have been investigated for LT-PEMFCs (Barbir, 2005). The most common type of flow field designs are shown in Figure 5.1.

The straight channel design with small manifolds has the shortcoming of inherent maldistribution of reactant gases, because the channels immediately below or above the manifold receive most of the flows while the others are starved of reactants, as a result of which the cell exhibits low and unstable cell voltages. The straight/parallel channel with large manifolds appears to provide uniform distribution, but the velocity in the channel would not be sufficient to push the water droplets out. Crisscross flow configuration eliminate the shortcomings of the straight channel flow field by introducing traversal channels allowing the gas to bypass any trouble spot of coalescing water droplets. However, the configuration suffers from low velocities and uneven flow distribution due to positioning of the inlet and outlet manifolds. Single-channel serpentine channels have large velocities which are typically high enough to push out the condensed water droplet in the channels. It is the most common flow field for small active areas. The concentration of reactants decreases along the channels, and the pressure drop in the channels increases with the number of turns within the cell active area leading to large pressure drops. Multichannel serpentine designs have a lower pressure drop and share the advantages of a serpentine channel such as allowing mixing at every turn and minimizing channel blocking. The flow fields based on interdigitated concept such as biomimetic, fractal and mesh type flow fields, are different from other flow fields because the channels are disconnected and they do not connect inlet to the outlet manifold. These typically suffer from high pressure drops.

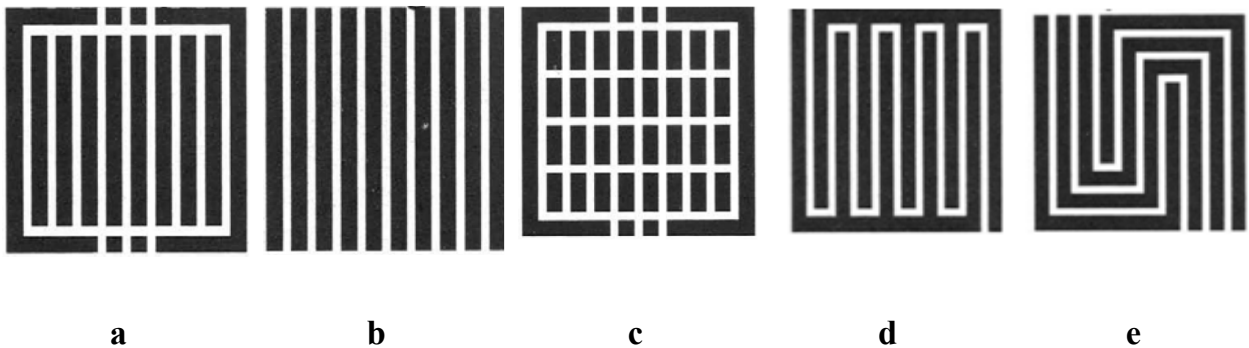


Figure 5.1: Flow field configurations (a) straight channels with small manifolds, (b) straight channels with large manifolds, (c) criss-cross configuration, (d) single-channel serpentine and (e) multichannel serpentine.

Among all the above flow fields, the multichannel serpentine flow field offers low pressure drop and good flow distribution. Since a multichannel serpentine flow field consists of parallel channels with multiple turns, there may be a possibility of channel blockage by water

droplets. However, in HT-PEMFCs, this is not a problem (except perhaps during start-up and shutdown) because, due to the high operating temperature, water is formed in the vapour phase rather than in liquid phase. The typical channel dimensions used in fuel cells are around 1 mm, but may vary from 0.4-4 mm. Flow channels that are too wide will not support the MEA. While wider ribs are good for the conduction of electrical current and heat, this reduces the effective active cell area and may also lead to high pressure losses. The four parallel serpentine channel (FPSC) chosen in the present study therefore has a flow channel width of 1 mm and a land width, also, of 1 mm. The channel depth is taken to be 1 mm while the bipolar plate is taken to have a thickness of 3 mm. Calculations of the flow and temperature fields have been carried out replacing the parallel flow channels in the computational model A (Figure 3.2) with FPSC (as shown in Figure 5.2) in the cathode air flow fields. Due to the symmetry boundary condition, the computational domain for the FPSC is extended to be 12 times wider than the domain for the parallel channels geometry. Thus the geometry in Figure 3.5 is extended in the x-direction to a total length of 24 mm. Other geometric and material properties have been kept the same as those for the cases discussed in Chapter 4.

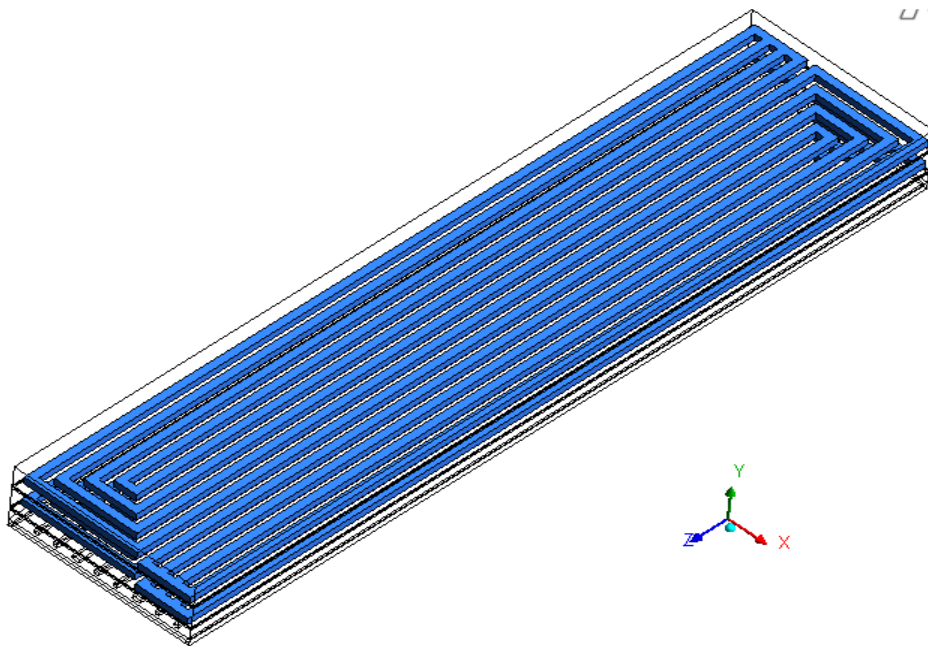


Figure 5.2: Schematic diagram of the computational domain of FPSC (showing one half-channel in the cooling plate and cathode flow channels in two cells).

Typical results obtained for the case of an HT-PEMFC stack segment with an external coolant (Duratherm oil) entering the coolant plate at a temperature of 400 K are shown in Figure 5.3 where the contours of velocity, pressure and temperature are shown in the mid-height x-z plane of the cathode flow field for an air stoichiometric factor of 1 and a cell operating voltage of 0.5 V. The figures show the four parallel serpentine flow channels, each channel containing two U-bends. Since the width of this unit is 24 mm, four such units will cover a cell width of 100 mm. The straight length of channels can be increased arbitrarily; the calculations shown in Figure 5.3b have been done for a straight channel length of 100 mm. It can be seen that the flow rate in the four channels is nearly the same indicating uniform reactant distribution. The serpentine channel pressure drop is expected to be higher than that for a straight channel and as shown in Figure 5.3b, the pressure drop within the cell active area (neglecting manifold losses) is about 700 Pa which is not very high. Increasing the stoichiometric factor to 4 may lead to a pressure drop of only about 3000 Pa which results in a fairly small blower power consumption. It

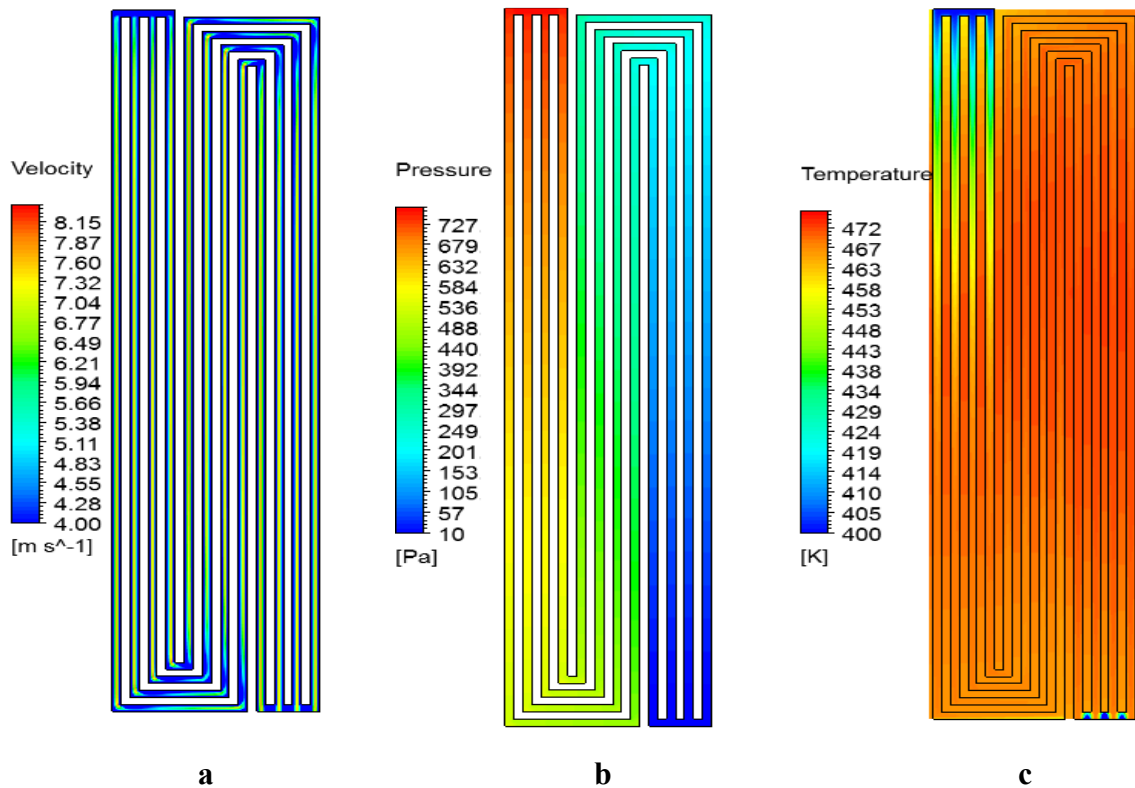


Figure 5.3: Four parallel serpentine channel (FPSC) in the cathode air flow field: (a) velocity profile, (b) pressure drop profile and (c) temperature profile.

may be noted that using a single serpentine channel to cover the same area would have resulted in a four-fold increase in the pressure loss and using it to cover the entire 100 mm width of the cell would have increased it by a further factor of four, i.e., a total pressure drop of ~ 50000 Pa in the cell active area for an air stoichiometric factor of four. The present arrangement, where the cell area is fed by four multi-parallel serpentes each containing four parallel serpentine channels thus decreases the pressure drop by a factor of 16 or more while ensuring fairly uniform flow throughout the cell. The predicted temperature distribution in the cathode flow field is shown in Figure 5.3c. Here it can be seen that a fairly uniform temperature is obtained throughout except for the region where cool air (at 300 K in this case) enters the cell. Preheating the air would reduce the temperature variation arising out of this.

The effect of using this more practically viable cathode flow field on the temperature and current density distribution on the catalyst layers is shown in Figure 5.4 and Figure 5.5 which show the contours of temperature and current density in the two catalyst layers, the bipolar plates and the cooling plate for the cases of integrated cathode air cooling and cooling with an external coolant, respectively. These can be compared with similar plots given in Chapter 4 for the case of parallel channel configuration for the cathode flow fields. It can be seen from Figure 5.4 for the integrated air cooling method that cathode air entering the cooling plate (from the bottom in Figure 5.4g) at 300 K gets heated quickly and leaves the cooling plate at ~ 410 K from the top and subsequently enters the cathode side of the first (Figure 5.4e) and the second bipolar plates (Figure 5.4f) at the top left hand corner. The air again gets heated quickly, but as it flows through, its temperature drops again due to the effect of the cool air entering the coolant plate. This effect is more prominent in the first cathode bipolar plate (Figure 5.4e) which is closer to the coolant plate than in the second cathode bipolar plate (Figure 5.4f). It can be seen from Figure 5.4c and d showing temperature distribution in the cathode catalyst layers that the effect persists even here and that as a consequence the current density variation (Figure 5.4a and b) follows a similar trend. Figure 5.5 shows the corresponding contours for the external coolant case where the coolant (Duratherm oil) enters the cooling plate at a temperature of 450 K at the top (Figure 5.5g) and flows down through parallel channels. While air enters the cathode channels at 300 K, it quickly heats up and the temperature distribution (Figure 5.5e and f) follows primarily that in the cooling plate. As a result, the first bipolar plate and the first cathode

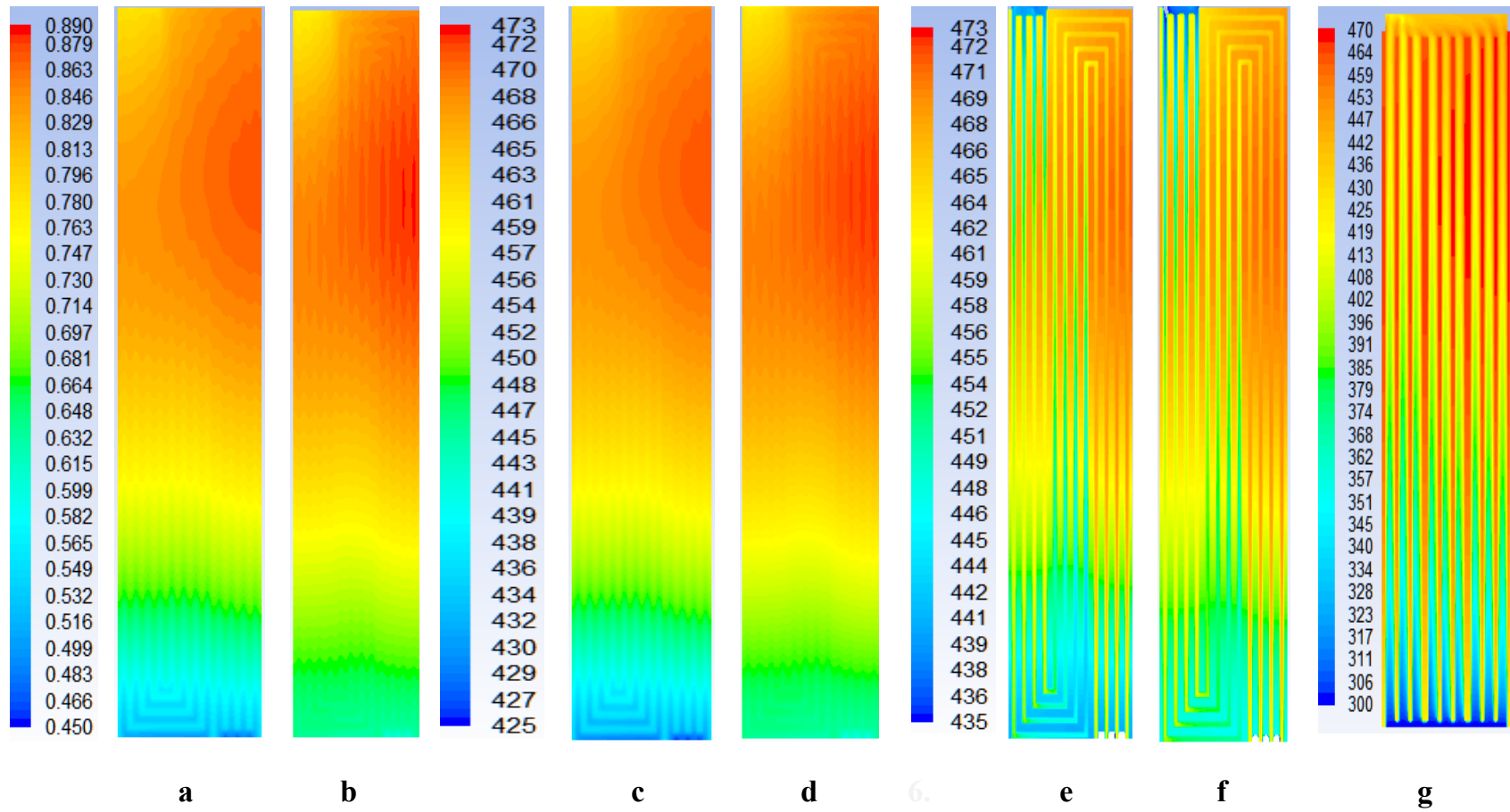


Figure 5.4: Integrated air cooling with FPSC (a) spatial current density variation in CCL-1, and (b) CCL-2, and (c) temperature variation in CCL-1, and (d) CCL-2, and (e) temperature variation in CFF-1, and (f) CFF-2, and (g) in the cooling plate.

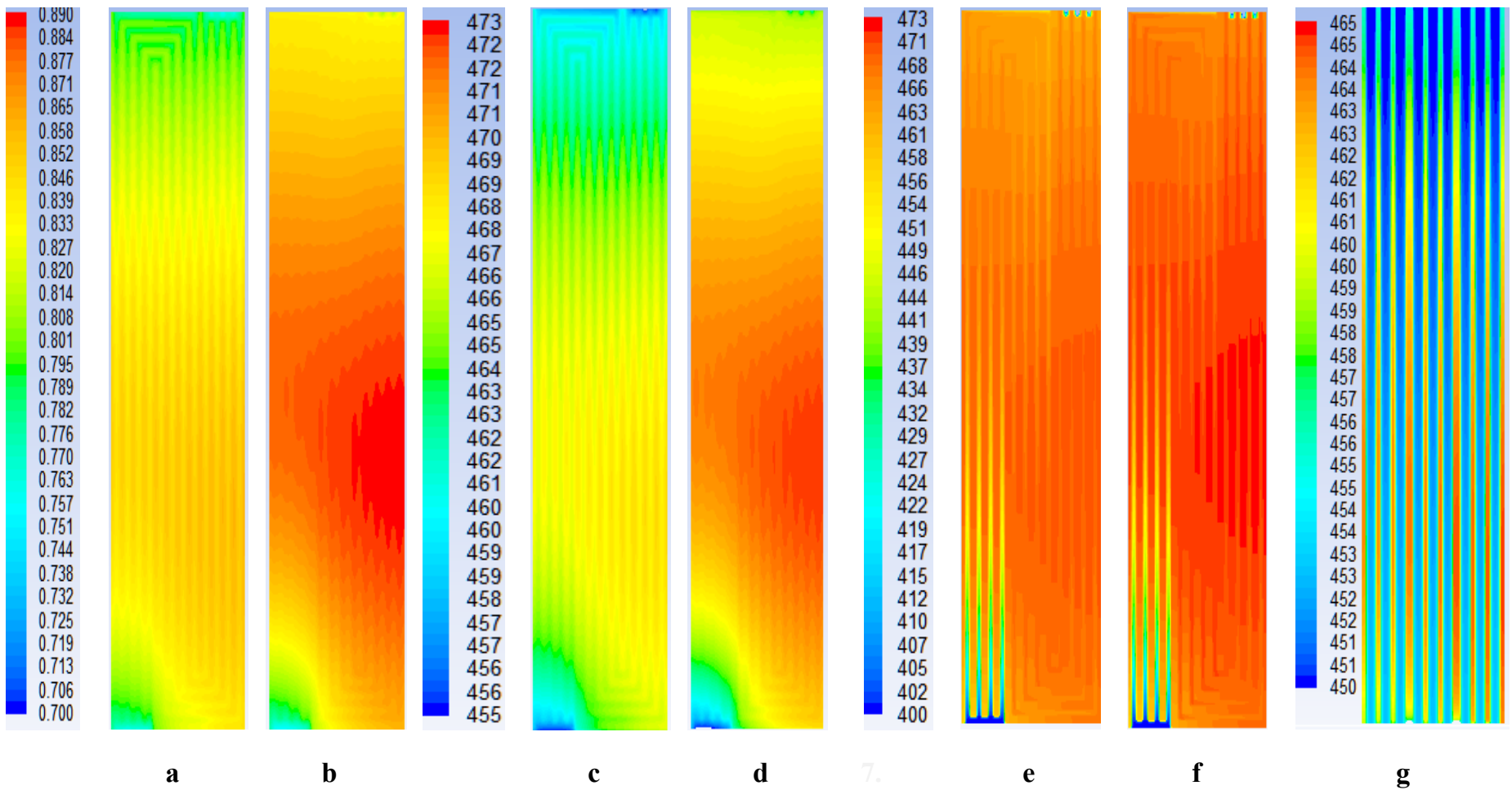


Figure 5.5: Liquid cooling with FPSC (at $T_{Cin} = 450$ K; $T_{Bin} = 400$ K $\lambda=2$), (a) spatial current density variation in CCL-1, and (b) CCL-2, and (c) temperature variation in CCL-1, and (d) CCL-2, and (e) temperature variation in CFF-1, and (f) CFF-2, and (g) in the cooling plate.

catalyst layer have a relatively lower temperature (Figure 5.5c and d) and lower current density (Figure 5.5a) than the corresponding layers of second cell (Figure 5.5b). Thus, the temperature distribution in the cooling plate has a strong effect on the temperature and current density distribution in the stack.

The effect of the cathode flow field on the average current density etc is summarized in Table 5.1. Here, the computed maximum temperature variation across the catalyst layers and the average current density obtained from the stack unit are both listed as a function of the coolant (oil or air) inlet temperature, the cathode air inlet temperature and the cathode air stoichiometric factor for parallel channel (PC) and four-parallel serpentine channel (FPSC) configurations. Also given here are the pressure drops between the inlet and the outlet of the coolant, and the air streams for each case. It can be seen that for the integrated air cooling case, the change of the cathode flow field from parallel to serpentine introduces only marginal differences in the average current density while pressure drop is higher by a factor of four. While it appears that therefore the parallel channel flow field is better, it must be noted that having a large number of parallel channels leads to flow maldistribution among the channels (Maharudrayya et al., 2005).

Table 5.1: Comparison between PC vs FPSC flow configuration in the bipolar plate for integrated air cooling and liquid cooling.

Type of Coolant	Type of the channel in the Bipolar plate	T_{Cin} (K)	T_{Bin} (K)	λ	ΔT_{Cat1} (K)	ΔT_{Cat2} (K)	i_{avg} (A/cm ²)
Air	PC	300	432	9.2	49	41	0.794
Air	FPSC	300	437	9.0	46	32	0.800
Oil	FPSC	400	300	1	50	42	0.721
Oil	FPSC	400	300	3	43	41	0.771
Oil	FPSC	450	300	1	24	28	0.835
Oil	FPSC	450	300	3	32	45	0.826

This effect is not considered in the present CFD simulations; a uniform flow through all the parallel channels is imposed as a boundary condition. Since the pressure drop with the FPSC configuration is fairly small (as shown later, the pumping power would amount to less than 1% of the total output), and multi-parallel serpentine flow-channels have proven better at flow

distribution and reducing mass transfer losses, FPSC flow-fields are recommended for air and fuel delivery to the cells. The same argument holds good for the external coolant case too; the cathode flow field configuration does not appear to have a significant bearing on the average current density; it is primarily determined by the coolant flow conditions. Increasing the coolant inlet temperature leads to a significant improvement in the average current density in all the cases. Specifically, for the case of coolant inlet at 450 K and air stoichiometric factor of 3, the average current density is 0.826 A/cm^2 , which is about 93% of the nominal value (of 0.890 A/cm^2) obtained assuming a constant temperature (of 473 K) across the cell. The computed current density and temperature on the second catalyst layer are shown in Figure 5.6; these show fairly uniform values over the entire cell. Based on these calculations, it is concluded that a four-parallel serpentine channel flow field would be a good choice for the electrode flow fields in the bipolar plates.

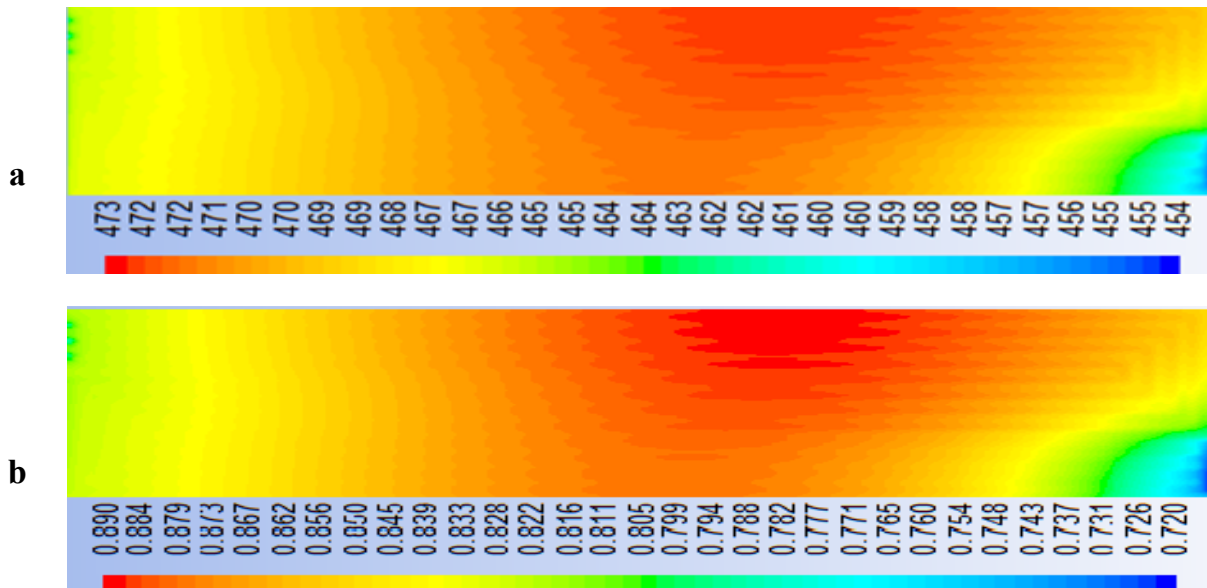


Figure 5.6: Liquid as coolant with FPSC ($T_{Cin} = 450 \text{ K}$; $T_{Bin} = 400 \text{ K}$ and $\lambda=3$), the spatial variation of (a) the current density in the CCL-2, and (b) the temperature in the CCL-2.

5.3 Flow fields for the coolant

Design requirements for a cooling plate are to have a high rate of heat transfer, whilst operating with a low coolant pressure drop and flow rate. Additionally, cooling plates that promote a

uniform temperature within the fuel cells are desirable, and as with all applications, low mass and cost are also objectives. In order to maintain a high average current density, cooling systems must be in place to keep the stack working in an optimal temperature range. Too low a temperature will reduce the efficiency of the cell and excessive variation in the temperature distribution in the cathode catalyst layers can lead to a reduction in the power available. However, the cooling system's power requirements should be as low as possible to reduce parasitic losses from the stack's electrical power output. Implementing an efficient and effective cooling system for an HT-PEMFC stack leads to higher stack power density and an increased lifespan of the cell components. The choice of the material for the cooling plate has been discussed in Chapter 4. The choice of the flow field is of present concern because for optimal performance, the coolant should be accessible equally to all parts of the cell. Given the results from the previous section, it may appear that a four-parallel serpentine channel configuration should be used for the coolant plate as well. However, as shown above, for high average current densities, it is necessary to maintain high coolant inlet temperatures. Since the maximum temperature anywhere in the cell is limited to 473 K in this study, increasing the coolant inlet temperature reduces the coolant temperature rise across the cell. For the same amount of heat to be removed, the coolant flow rate therefore increases, especially as the coolant inlet temperature approaches that of the cell temperature. This leads to very high pressure losses in the coolant plate, as will be shown presently.

In view of this difficulty of needing to maintain high coolant inlet temperatures while keeping the pressure losses low, three possible coolant flow field configurations have been considered in the present study. These are schematically shown in Figure 5.7 and can be described as follows:

- A parallel flow field with a channel width of 1 mm and a land width also of 1 mm,
- A parallel flow field with a channel width of 2 mm and a land width of 0.5 mm with the land width being 1 mm for every third channel, and
- A four-parallel serpentine channel with a channel and land widths of 1 mm each.

While the first and the third flow fields require no further elaboration, the second one is designed to reduce the pressure drop by increasing the width of the channel. The larger land area

for every third channel provides mechanical support for the cell. Increasing the channel width also reduces the number of parallel channels for a given cell face area and thus reduces the flow maldistribution problem. Flow and temperature calculations have been done for different cases as before for different coolant plate configurations while using an FPSC configuration for the bip

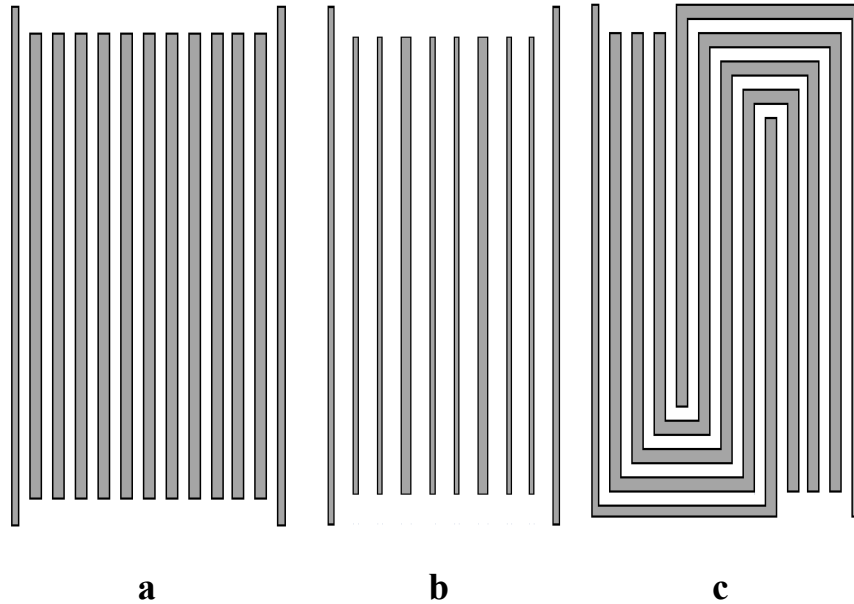


Figure 5.7: Flow field configurations in the cooling plate (a) parallel flow field with a channel width of 1 mm, (b) parallel flow field with a channel width of 2 mm and (c) four parallel serpentine channel.

-olar plates on cells operating at 0.5 V. The results are summarized in Table 5.2 which shows the computed temperature difference at the two catalyst layers, the average cell current density and the pressure drop in the coolant channel for different cathode air stoichiometric factors, coolant inlet temperatures and coolant flow fields. It can be seen that for a coolant inlet temperature of 400 K, the average current density is rather low at $\sim 0.75 \text{ A/cm}^2$. For this condition, the FPSC configuration gives a markedly higher current density but at the cost of a pressure drop which is higher by a factor of 40-100. If the coolant inlet temperature is increased to 450 K, all the coolant flow fields show marked improvement in the current density (all configurations give over 0.82 A/cm^2). However, the pressure drop across the coolant plate also increases tremendously due to the higher coolant flow rate with the FPSC showing a pressure drop of 3 to 4 bar. This can be reduced somewhat by increasing the channel width but will still be very high. The second

configuration, on the other hand, gives a pressure drop that is nearly half of that of the 1 mm wide PC configuration without compromising on the average current density. The computed current density and temperature distribution on the second cathode catalyst layer for this case are shown in Figure 5.8. These show a fairly uniform distribution without any marked hot or cold spots. Based on these considerations, it is therefore concluded that the wide-channel PC configuration shown in Figure 5.7b would make an ideal choice for the coolant plates.

Table 5.2: Comparison of different flow field configurations in the cooling plate.

TC _{in} (K)	Configuration (W _{ch})	λ	ΔT_{Cat1} (K)	ΔT_{Cat2} (K)	i_{avg} (A/cm ²)	ΔP_{CPch} (Pa)	m_{cp} (kg/s)
400	PC (1 mm)	1	50	42	0.721	303	1.38×10 ⁻⁴
400	PC (2 mm)	1	49	40	0.737	100	1.56×10 ⁻⁴
400	FPSC (1mm)	1	34	27	0.805	13336	1.96×10 ⁻⁴
400	PC (1 mm)	3	43	41	0.771	173	7.92×10 ⁻⁵
400	PC (2 mm)	3	41	41	0.759	81	1.26×10 ⁻⁴
400	FPSC (1mm)	3	33	44	0.825	10508	1.55×10 ⁻⁴
450	PC (1 mm)	1	24	28	0.835	5714	3.42×10 ⁻³
450	PC (2 mm)	1	19	25	0.839	2608	3.81×10 ⁻³
450	FPSC (1mm)	1	21	28	0.837	463327	2.23×10 ⁻³
450	PC (1 mm)	3	32	45	0.826	2615	2.44×10 ⁻³
450	PC (2 mm)	3	30	43	0.826	1422	2.15×10 ⁻³
450	FPSC (1mm)	3	31	45	0.822	315366	1.37×10 ⁻³

5.4 Pressure drop estimation in manifolds

5.4.1 Type of manifolds

Fuel cell stacks with a large number of cells require a manifold for uniform flow distribution among the cells connected in parallel in order to obtain good overall performance from the stack. The manifolds feed the reactant gases to the active cell areas and also collect the unused reactan-

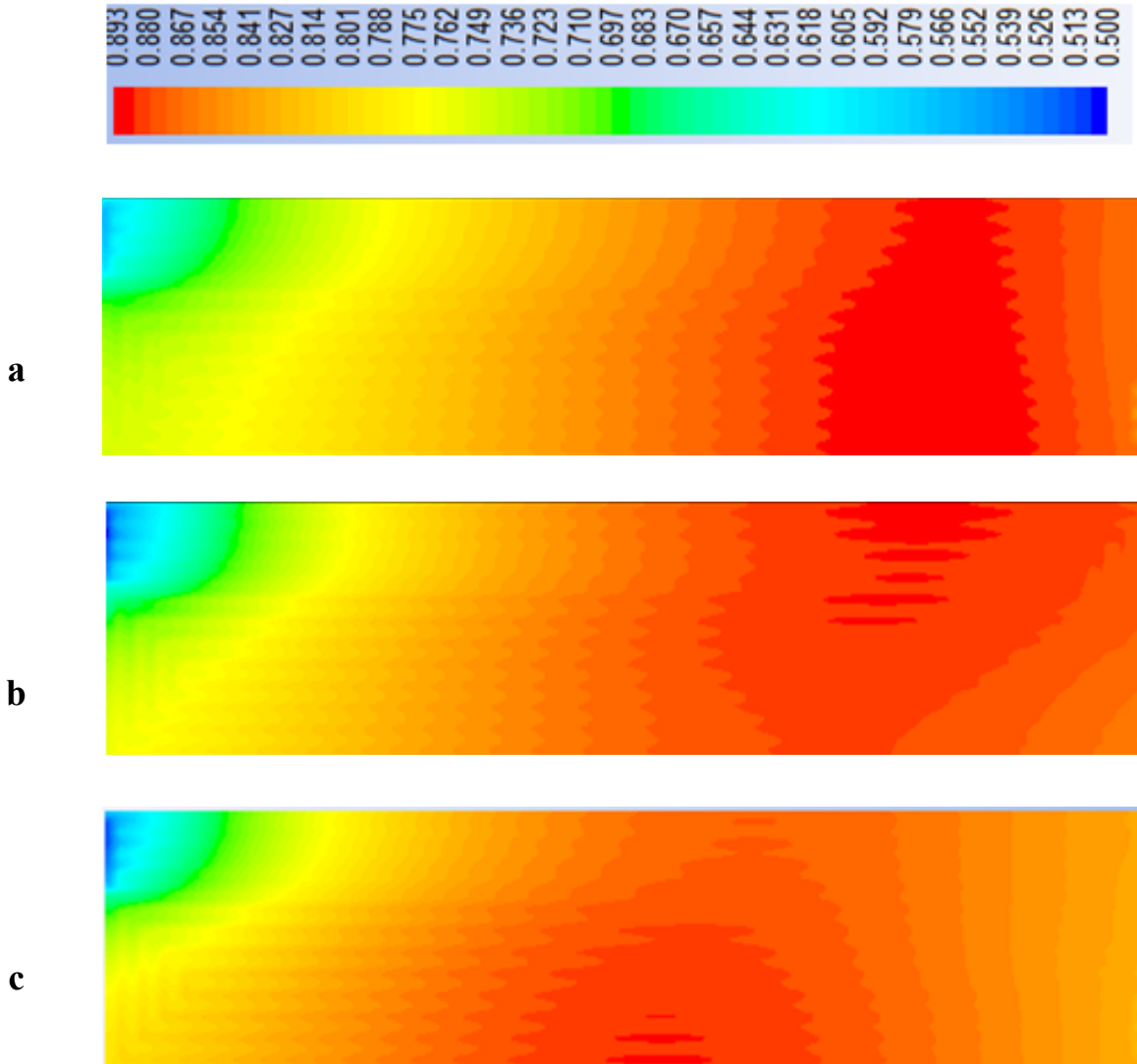


Figure 5.8: Spatial current density variation (A/cm²) in the CCl-2 with respect to cooling channel geometry of (a) PC (1 mm), (b) PC (2 mm), (c) FPSC (1 mm), cell operated at a $V_{\text{cell}} = 0.5$ V; $T_{\text{Bin}} = 400$ K; $T_{\text{Cin}} = 450$ K; $L_{\text{ch}} = 10\text{cm}$; $\lambda = 3$ and thermal oil as coolant.

ts and products of the reaction. The configuration of the gas flow manifolds for a fuel cell stack is therefore an important engineering problem where once again a balance needs to be struck between uniformity of flow distribution and minimizing pressure drops. It may also be noted that due to the small dimensions of the cells and flow channels and the sheer number of the cells connected in parallel, it is not feasible to have a valve located at each cell to ensure uniform flow. Therefore, valve-less gas manifolds are needed. The geometrical structure and size of the

gas manifolds are the important parameters that need careful consideration. The cross-sectional area of the manifold pipe is important because it determines the linear velocity of gas-flow through the manifolds for a given flow rate of the inlet gas. The shapes of manifold holes can be circular, rectangular, or oblong and are determined partly by the ease of fabrication of such geometries.

The gas flow domains within the stack are the inlet manifolds, the flow channels which feed the electrodes, and the outlet manifolds. As a general thumb rule, the pressure drop through the manifolds should be an order of magnitude lower than the pressure drop through each cell in order to ensure uniform flow distribution. Planar fuel cells have two types of manifolds, namely, internal or external manifolds. External manifolds are simpler, less costly than internal manifolds but are susceptible to leakage and sealing problems. Internal manifolds have the advantage of better sealing but are costlier and add weight to the stack. Given that HT-PEMFCs mostly deal with gaseous reactants and products (water is produced in vapour form), leakage from liquid water accumulation and corrosion is less of a problem. Since the reactant distribution manifolds of the anode and the cathode side are hydrodynamically decoupled, severe maldistribution of the reactants is possible across the stack. For large stacks, external manifolds offer more flexibility and more possibility of matching reactant flow rates. In view of these advantages, we consider external manifolds in this section. We use a branched manifold pattern in which the flow goes through a small number of subdivisions at each level. A typical example is shown in Figure 5.9 where a single pipe undergoes 2, 3, and 4 subdivisions to cater eventually to $2 \times 3 \times 4 = 24$ parallel cells. Such a configuration with a small number of subdivisions at each level will ensure that severe non-uniformities are avoided.

5.4.2 Methodology for pressure drop calculations

The objective of the branched manifold design is to ensure that at each subdivision, the flow is uniformly split at each level. We consider that the manifold piping is circular in cross section with varying diameter in stage. We assume that the reactant circuit pump is located at a distance of three stack lengths; throughout this length, the total reactant flow rate for the stack flows through a single pipe. Very close to the stack, the pipe splits successively into subdivisions. For the manifolds shown in Figure 5.9, the main pipe divides into two pipes, each of which

subdivided into three further pipes, each of which then further subdivide into four pipes which feed directly to each of the 24 cells. At each stage, the diameters of the split pipes are adjusted so as to have equal pressure drops for the different flow paths.

The velocity in a given manifold pipe section of diameter d can be computed for a given mass flow rate as

$$v = \frac{m}{\rho} \frac{1}{\pi d^2} \quad (5.1)$$

where v is the velocity in the manifold, m is a mass flow rate of the reactant through that section and ρ is the density of the reactant stream. The Reynolds number in the manifold section can be written as

$$Re = \frac{dv\rho}{\mu} \quad (5.2)$$

where μ is a viscosity of the reactant. The friction factor can be calculated depending on the Reynolds number as follows

for a laminar flow $f = \frac{16}{Re} \quad (5.3)$

for a turbulent flow $f = 0.079Re^{-0.25} \quad (5.4)$

The pressure drop in a pipe section of length l can then be calculated as

$$\Delta p = \frac{2f\rho v^2 l}{d} \quad (5.5)$$

It may be noted that equation (5.5) accounts only for the straight pipe pressure losses. The method of calculation can readily be extended to include losses due to bends etc. Since the present configuration contains only one bend per stage, and since the bend pressure losses are fairly small for low Reynolds number flows, this contribution is neglected in the present study. The objective of the manifold design for uniform flow distribution is then to choose the appropriate diameter for each delivery pipe in such a way that the pressure drop at each stage

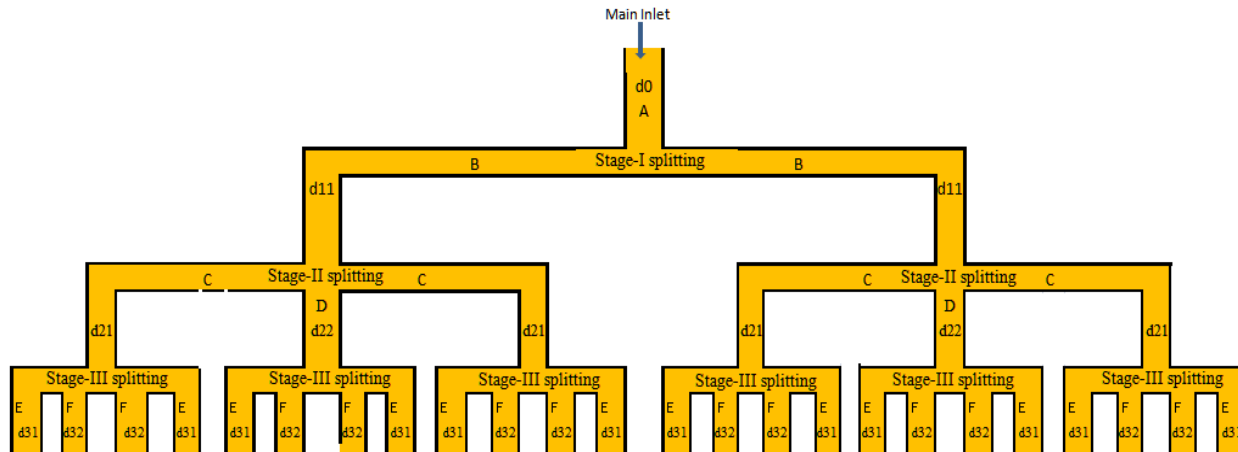


Figure 5.9: External manifold arrangement for the reactant.

for each flow path is the same. This becomes clear with the following specific example. Figure 5.9 shows the splitting of the inlet flow into sub-channels in three stages of branching. In stage-I, the inlet flow (shown in the figure as channel-A) is divided into two parts (shown as channel-B); these are identical because the flow split is symmetric and each part supplies the amount of reactant which is required for 12 cells in the stack. In stage-II, the mass flow in channel-B is split into three equal parts, two delivery flow paths (channel C) which are identical to each other and one (channel D) which is shorter. Therefore, channels C and D should have different diameters (diameter D should be smaller than that of C) in order to have the same pressure drop in the stage. Thus, the diameters of channels C and D are adjusted in order to make equal pressure drops at the junction. In stage-III, the flow through channels C and D is further split into four parts containing two symmetric branching patterns. This requires channels of two distinct diameters, channels E and F, such that the pressure drop is the same in the stage for the different flow paths. Thus, if advantage is taken of the symmetry afforded by the geometry, then it is possible to use a manifold with three branchings and channels of six distinct diameters so as to distribute the flow uniformly across the 24 cells connected in parallel. Application of this methodology to the design of the air, hydrogen and coolant manifolds is illustrated below.

5.4.3 Pressure drop in the air manifold

The pressure drop in the manifold should be less than the pressure drop in the cell active area to help in uniform distribution across the cells. In the present study, a 1 kWe HT-PEMFC stack

operating at a cell voltage of 0.5 V has 24 cells connected in series with an active cell cross-section of 100 mm x 100 mm. The manifolds are taken to be of circular cross section and the three-stage splitting of the manifold shown in Figure 5.9 is considered. The pressure drop in the FPSC flow field on the cathode side is about 750 Pa. Therefore, the manifold pressure drop should be considerably less than this. In view of this, the main pipe is chosen to have an internal diameter of about 1.4 cm and successive sub-divided channels are gradually reduced in size so as to have a uniform transition to the cell cross-section of 1 mm x 1 mm. The results of these calculations for a stoichiometric factor of three are summarized in Table 5.3. It can be seen that

Table 5.3: Pressure drops and manifold diameter in an external air manifold ($L_{ch}=10$ cm, $\lambda=3$ and $N_{cell}=24$).

	Inlet	Stage-1	Stage-2		Stage-3	
Section	A	B	C	D	E	F
Mass flow (kg/s)	2.18×10^{-3}	1.09×10^{-3}	3.63×10^{-4}	3.63×10^{-4}	9.07×10^{-5}	9.07×10^{-5}
Diameter (m)	17×10^{-3}	9×10^{-3}	6.025×10^{-3}	2.50×10^{-3}	2.40×10^{-3}	2.06×10^{-3}
Velocity (m/s)	7.71	13.76	10.23	59.44	16.12	21.88
Reynolds no., R_e	9012	8512	4238	10214	2660	3099
Friction factor, f	8.1×10^{-3}	8.2×10^{-3}	9.8×10^{-3}	7.9×10^{-3}	11×10^{-3}	10.6×10^{-3}
ΔP (Pa)	18	11	6	6	18	18

the pressure drop in the three stages, including that in the feed pipe from the air pump, is about 53 Pa for the inlet manifold. Assuming a similar configuration for the outlet manifold, the total manifold pressure drop comes out to be ~105 Pa which is considerably less than the pressure drop of ~760 Pa over the cell. It may be noted that although bend losses, contraction/expansion losses, etc. have been neglected in these calculations, these can be readily included for a specific case.

5.4.4 Pressure drop in the fuel manifold

The hydrogen supply to the stack through a splitting fuel manifold (as shown in Figure 5.9) is done in the same way as for cathode air. The results for a stack length of 10 cm and for a

stoichiometric factor of three are shown in Table 5.4. Since the hydrogen flow rate is considerably less than that on the cathode, the pressure drops are also lower. The inner diameter of the main inlet is 10 mm and gradually reduces to that of the cell cross-section. The total pressure drop in the fuel inlet manifold is ~ 19 Pa, giving a total manifold pressure drop of ~ 38 Pa which compares favourably with the FPSC anode flow field pressure drop of ~ 236 Pa.

Table 5.4: Pressure drops and manifold diameter in an external fuel manifold ($L_{ch} = 10$ cm, $\lambda = 3$ and $N_{cell} = 24$).

	Inlet	Stage-1	Stage-2		Stage-3	
Section	A	B	C	D	E	F
Mass flow (kg/s)	8.41×10^{-5}	4.20×10^{-5}	1.40×10^{-5}	1.40×10^{-5}	3.50×10^{-6}	3.50×10^{-6}
Diameter (m)	10×10^{-3}	6×10^{-3}	5×10^{-3}	2×10^{-3}	2×10^{-3}	1.7×10^{-3}
Velocity (m/s)	13.07	18.16	8.72	54.48	13.62	18.85
Reynolds no., Re	1273	1061	424	1061	265	312
Friction factor, f	1.26×10^{-2}	1.51×10^{-2}	3.77×10^{-2}	1.51×10^{-2}	6.03×10^{-2}	5.13×10^{-2}
ΔP (Pa)	9	3	1	1	5	5

5.4.5 Pressure drop in the coolant manifold

An HT-PEMFC stack with 24 cells has seven cooling plates (see Figure 5.10) as each cooling plate serves four cells. A two-stage splitting of the coolant manifold (as shown in Figure 5.11) is considered for the seven parallel channels. The coolant flow rate depends highly on the coolant inlet temperature and increases by more than an order of magnitude when the coolant inlet temperature is increased from 400 K to 450 K, as seen earlier in Section 5.3. For the present calculations, the case with the highest pressure drop, which corresponds to a coolant inlet temperature of 450 K, is considered. For the manifold pattern shown in Figure 5.11, the splitting is done in two stages: in stage-I, the inlet flow (indicated as Cp-A) is divided into three parts (indicated as two Cp-B channels and one Cp-C channel), in which each Cp-B supplies coolant to three channels in the stack while channel Cp-c supplies coolant directly to the central coolant plate. In stage-II, coolant flow through each Cp-B channel is further divided into three branches. As per the coolant flow rate requirement, the last coolant plate cools only two cells and therefore

has half the flow rate requirement. Therefore the coolant through channels Cp-B are split into channels of size Cp-E, Cp-F, each of which has the same flow rate (which is equal to the flow rate in channel Cp-C) and Cp-D which has half of the mass flow rate of Cp-E.

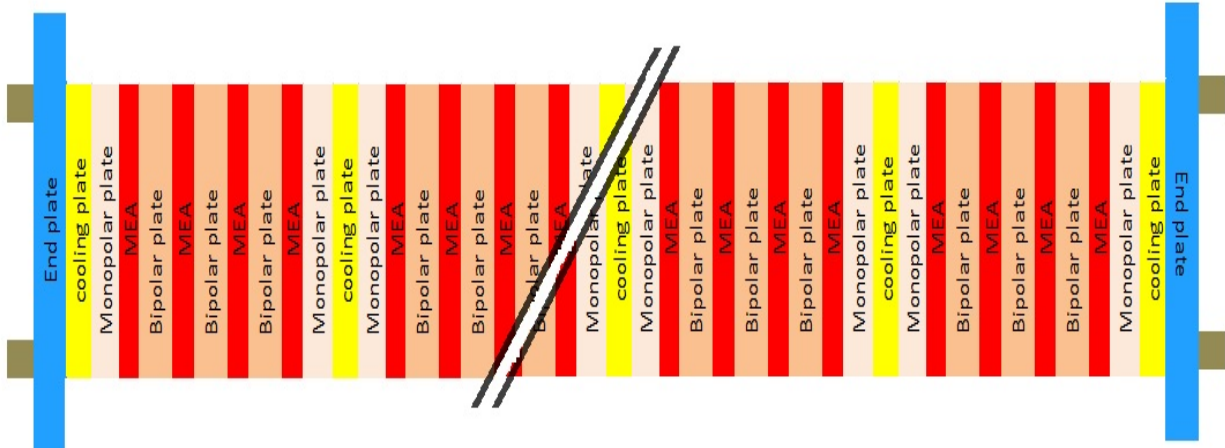


Figure 5.10: Cells and cooling plate arrangement in the stack.

The channel diameters from Cp-A to Cp-F are adjusted in order to have the required flow distribution in each channel while ensuring low pressure drop in the manifold compared to that in the coolant plate. The calculations are summarized in Table 5.5. It can be seen that the inlet pipe has an inner diameter of 17 mm. The pressure drop in the coolant inlet manifold is ~ 300 Pa which gives a total manifold pressure drop of ~ 600 Pa which is well below the coolant plate pressure drop of ~ 800 Pa for this case.

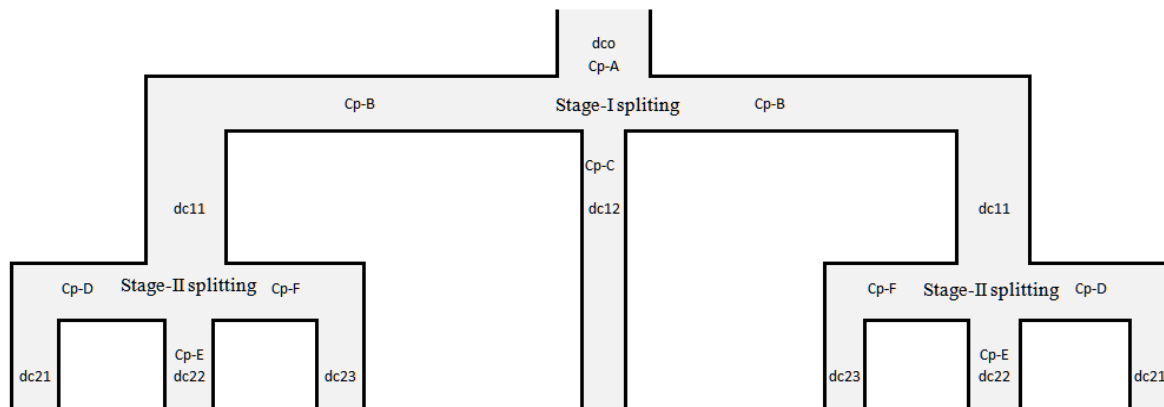


Figure 5.11: External manifold arrangement for the coolant.

Table 5.5: Pressure drops and manifold diameter in an external coolant manifold ($L_{ch}= 10$ cm, $N_{cell}=24$, $T_{Cin}=450$ and $T_{Bin}= 400$ K and $\lambda=3$).

	Inlet	Stage-1		Stage-2		
Section	Cp-A	Cp-B	Cp-C	Cp-D	Cp-E	Cp-F
Mss flow (kg/s)	3.13×10^{-3}	1.50×10^{-1}	6.26×10^{-2}	2.50×10^{-2}	1.25×10^{-2}	2.50×10^{-2}
Diameter (m)	17.6×10^{-3}	8.8×10^{-3}	1.19×10^{-3}	4.1×10^{-3}	2.2×10^{-3}	5.1×10^{-3}
Velocity (m/s)	0.73	1.19	10.17	1.10	7.41	1.42
Reynolds no., Re	3684	3040	5638	1306	4803	2100
Friction factor, f	10.14×10^{-3}	10.64×10^{-3}	9.12×10^{-3}	12.25×10^{-3}	9.49×10^{-3}	7.62×10^{-3}
ΔP (Pa)	103	101	194	93	92	93

5.5 Scale up for higher power

Due to the wide range of power requirements in fuel cell applications in the transportation sector, the cell and stack sizing must be configured by taking the following aspects into account:

- uniform flow distribution of reactants to each cell and within cell active area,
- maintenance of required temperature/uniform temperature in each cell,
- minimum resistive losses (choice of materials, configuration, uniform contact pressure),
- no leakage of reactant gases and coolant (internal between the cells or external),
- mechanical strength (to withstand internal pressure, external forces during handling and operation, including shocks and vibration).

In the present section, we address the thermal management problem by considering various possibilities of cooling stacks of different sizes.

5.5.1 External air flow over the stack

Increase in the stack size reduces the surface area to volume ratio and therefore the area available for heat transfer by external air cooling over the stack. The distance from the surface to the core of the stack also increases. Due to these two factors, natural convective heat transfer calculations show the amount of heat removed through the edges by natural convection is reduced from

4.67% to 2.35% with an increase in cell active area from 0.01-0.0625 m². In the case of forced draft, an air velocity of 25 m/s (90 kmph) leads to a temperature difference of 50 K between the surface and the core for a 0.1 m × 0.1 m cell. If the cell size is increased to 0.25 m × 0.25 m, the temperature difference for the same air velocity increases to 120 K, i.e., parts of the cell along the outer edge will operate at cell temperatures as low as 80°C, which will be disastrous for a PBI-based membrane. Therefore, operation of a large HT-PEMFC stack with forced draft alone for thermal management is not advisable.

5.5.2 Integrated cathode air cooling

As seen in Chapter 4, with integrated cathode air cooling, it is possible to keep the cell temperatures to below 200°C by operating at a high stoichiometric factor of about 8 for a cell area of 0.1 m × 0.1 m. These calculations have been repeated for cell sizes of 0.2 m × 0.2 m and 0.3 × 0.3 m by increasing the length of the flow domain appropriately. The predicted temperature and current density contours in the second cathode catalyst layer are compared in Figure 5.12 for the three (the images are scaled in order to allow easier visual comparison). It can be seen that the pattern of temperature and current distribution is similar although the range of variation appears to increase as the size of the cell increases. The results, in terms of the average current density and maximum temperature difference over the catalyst layer, are summarized in Table 5.6.

Table 5.6: Temperatures and current density in stack with parallel flow field in the cooling plate and FPSC in the bipolar plate at a cell voltage of 0.5 V.

L _{ch} (cm)	λ	Outlet temperature (K)		Minimum temperature (K)		i _{avg} (A/m ²)
		T _{out1}	T _{out2}	T _{cat1}	T _{cat2}	
10	7.85	410	413	425	441	0.794
20	8.88	399	403	407	424	0.766
30	9.09	395	399	399	418	0.755

It can be seen that as the cell size increases, the air stoichiometric factor required to keep the maximum cell temperature below 473 K increases slightly. While the average current density decreases slightly with increasing cell size, the minimum catalyst layer temperature shows a more pronounced decrease with increasing cell size. This decrease in average cell temperature causes the observed decrease in average current density. For higher current densities (at lower cell voltages), the drop in performance is more pronounced. For example, at a cell voltage of 0.5 V, the average current density deviation from the ideal is about 11% for a cell size of 100 mm, 14% for a cell size of 200 mm and 15% for a cell size of 300 mm. Also, with increasing cell size, the air flow requirements will also be higher and the air-side pressure drop will increase, especially for such high stoichiometric factors. Thus, the integrated air cooling may not be an good option for large cells.

5.5.3 Liquid coolant

Similar calculations for larger cell sizes have been done for the external coolant case. The predicted temperature and current density contours in the first cathode catalyst layer for thermal oil coolant with an inlet temperature of 450 K for cell sizes of 100×100 , 200×200 and 300×300 mm are shown in Figure 5.13 (images are scaled for easier visual comparison). The contours show a similar effect of increasing cell size on the average current density as for the integrated air cooling case.

However, as noted earlier, the performance of the external coolant depends significantly on the coolant inlet temperature. This is illustrated in Figure 5.14 and Figure 5.15 which show the average current density and the temperature differences on the two catalyst layers as a function of the length of the cell and the cathode air Stoichiometric ratio for coolant inlet temperatures of 400 K and 450 K, respectively. It can be seen that in the former case, there is a pronounced increase in temperature difference on the catalyst layer when the cell size increases and a consequent decrease in the average current density (Figure 5.15). The response to the cell size is more muted when the coolant inlet temperature is increased to 450 K, as can be seen in Figure 5.15. Here too, one can see fairly large temperature differences on the catalyst layers. However, these are associated with the air inlet temperature and since, the cathode air heats up very quickly, this variation does not have a significant effect on the average current density

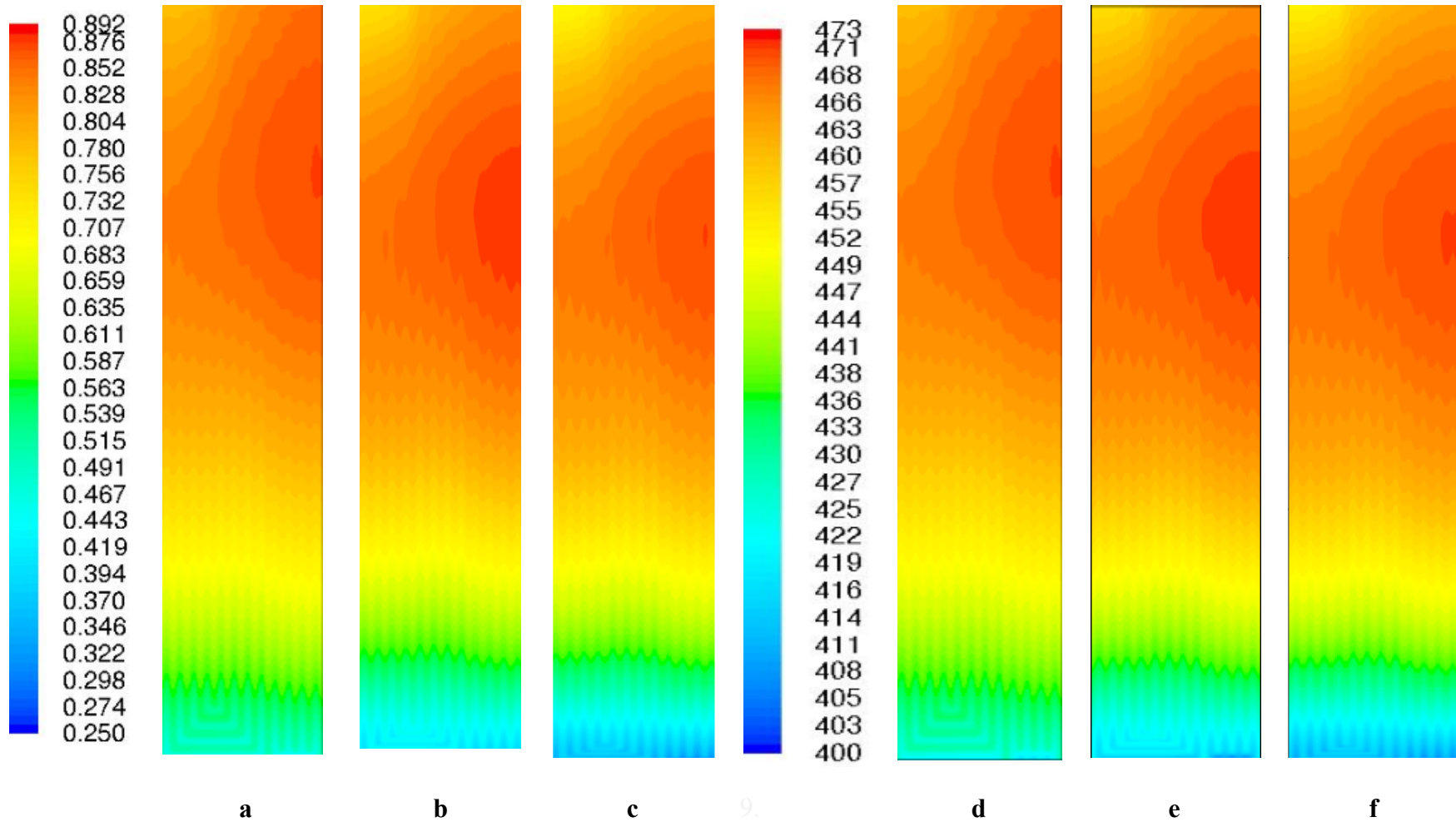


Figure 5.12: Spatial current density (A/cm^2) variation in CCL-2 (a) $L_{ch} = 10$ cm, (b) $L_{ch} = 20$ cm, (c) $L_{ch} = 30$ cm, spatial temperature (K) variation in CCL-2 (d) $L_{ch} = 10$ cm, (e) $L_{ch} = 20$ cm, and (f) $L_{ch} = 30$ cm for an integrated air cooling method.

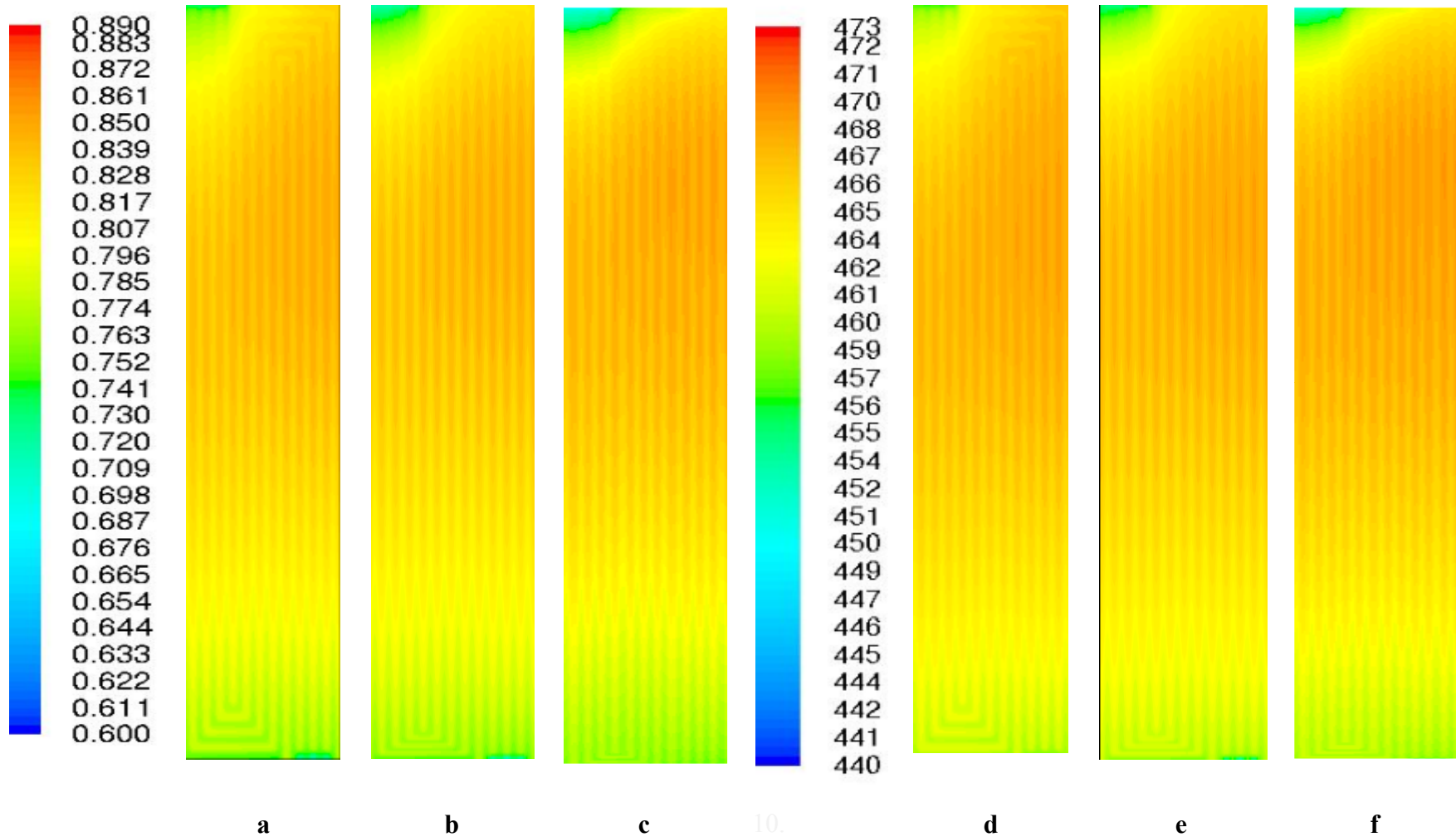
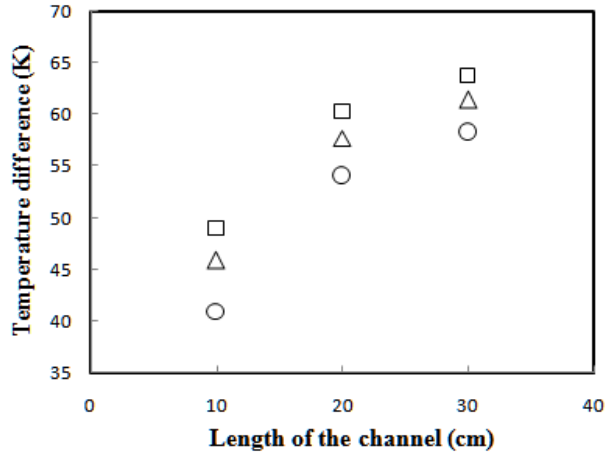
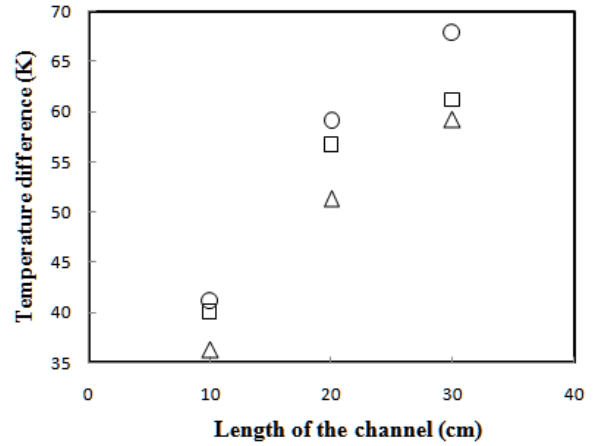


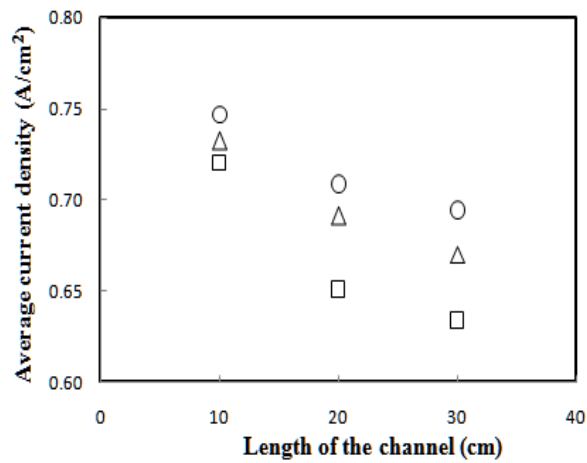
Figure 5.13: Spatial current density (A/cm^2) variation in CCL-2 (a) $L_{ch} = 10$ cm, (b) $L_{ch} = 20$ cm, (c) $L_{ch} = 30$ cm, spatial temperature (K) variation in CCL-2 (d) $L_{ch} = 10$ cm, (e) $L_{ch} = 20$ cm, and (f) $L_{ch} = 30$ cm for an external liquid cooling method.



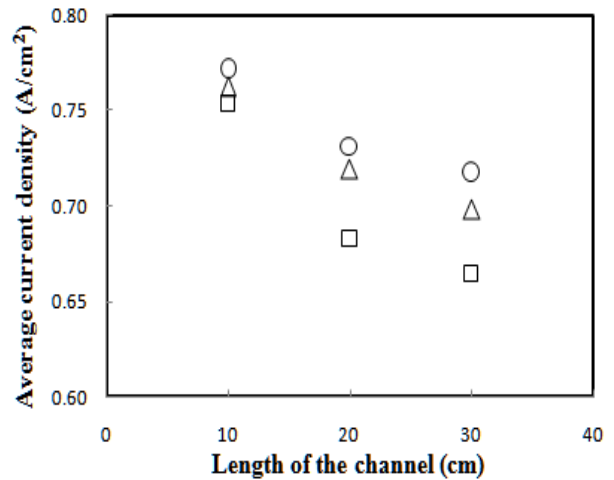
a



b



c



d

Figure 5.14: (a) ΔT_{cat1} , (b) ΔT_{cat2} , (c) i_{avg} in CCL-1 and (d) i_{avg} in CCL-2 with respect to channel length and excess amount of air in the cathode channel; oil-cooled stack; $\lambda=1$ (rectangular); $\lambda=2$ (triangular); $\lambda=3$ (circular); $V_{cell} = 0.5$ V; $T_{Bin} = 300$ K and $T_{Cin} = 400$ K.

which remains fairly high. Figure 5.15 also shows the results obtained for an air inlet temperature of 400 K. While this leads to substantial drop in the temperature difference in the catalyst layer, the average current density is not altered significantly, which reinforces the above point.

The above results show that with a liquid coolant, the cell temperature variation over the catalyst can be controlled within a tight range by having a high coolant inlet temperature. This results in a fairly uniform temperature and current density variation, as shown in Figure 5.15, even for large cells.

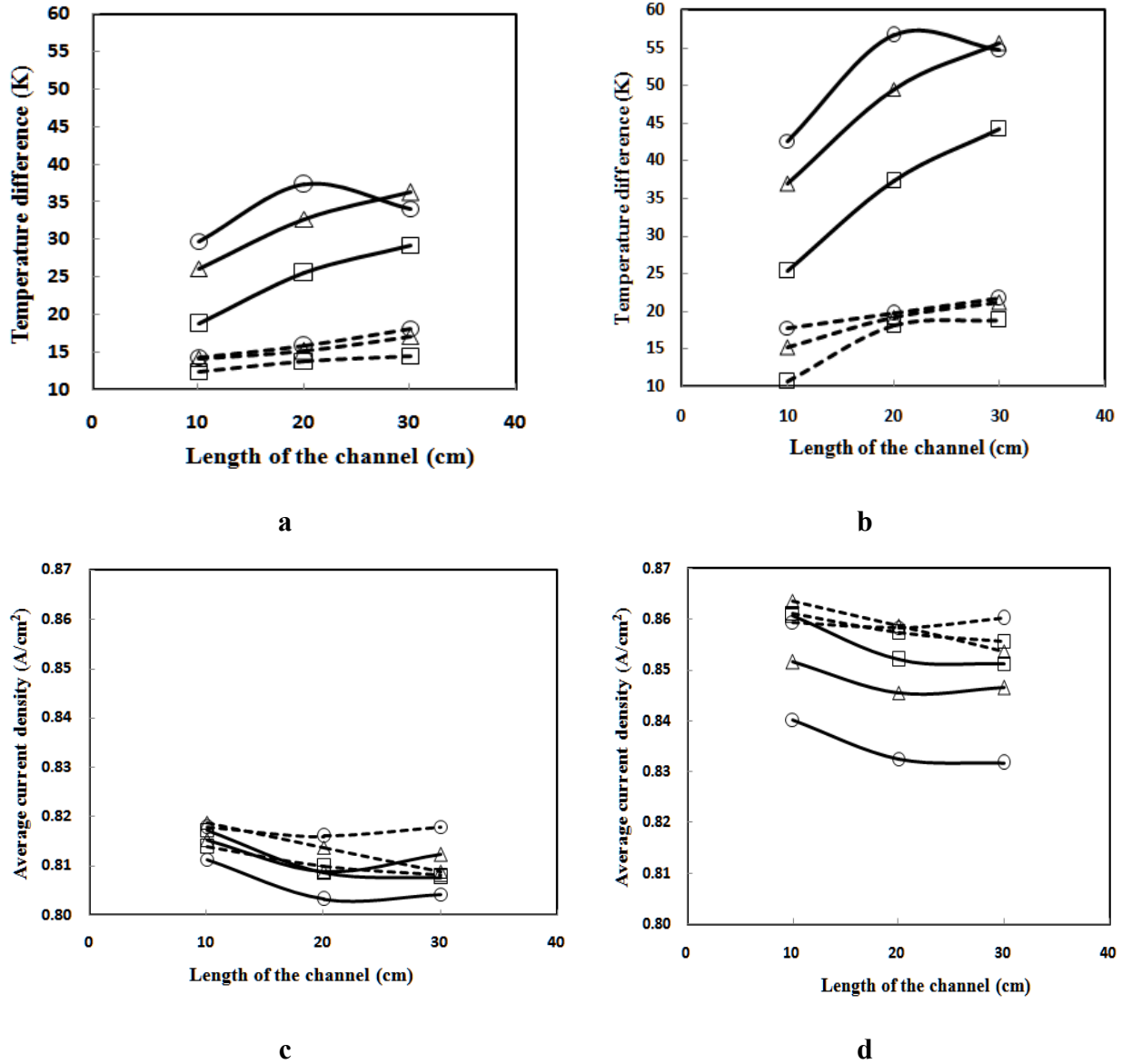


Figure 5.15: (a) ΔT_{cat1} , (b) ΔT_{cat2} , (c) i_{avg} in CCL-1. and (d) i_{avg} in CCL-2 with respect to channel length and excess amount of air in the cathode channel; $\lambda=1$ (rectangular); $\lambda=2$ (triangular); $\lambda=3$ (circular)). $V_{cell} = 0.5$ V; $T_{Bin} = 300$ K (solid line) and 400 K (dashed line); $T_{Cin} = 450$ K.

Table 5.7: Current density and specific power density for stacks with liquid cooling vs integrated air cooling at cell voltage of 0.5 V.

T _{Cin} (K)	T _{Bin} (K)	λ	Specific power density (W/kg)			i _{avg} (A/cm ²)		
			10 cm	20 cm	30 cm	10 cm	20 cm	30 cm
400	300	1	515	466	454	0.737	0.667	0.649
400	300	3	538	504	494	0.769	0.720	0.706
450	400	1	586	583	582	0.837	0.834	0.832
450	400	3	587	586	587	0.839	0.837	0.839
300*		~9-11	555	536	528	0.794	0.766	0.755

* Values for an integrated air cooling system are given in the last row for comparison.

5.5.4 Stack design

When scaling up to larger power requirements, the key variables are the size of the active cell area, the number of cells, the operation temperature and the current density at the design point. The maximum temperature is limited by thermal stability of cell components such as the membrane. As the size and the number of cells increases, thermal management becomes more and more difficult. A related problem that also becomes more severe as stacks are scaled up is that of stack startup. A possible solution is the use of modular fuel cell stacks which has the further advantage of adding redundancy to the entire system and also enabling operation during partial breakdown (Rajalakshmi et al., 2008). The fuel cell system can be constructed by using an encapsulated cooling cell concept in order to produce the required power output. Systems of various power ratings can be obtained by simply connecting these compact stacks electrically in series or parallel depending on the end use. As an example, 10 stacks designed for 10 kWe each can be integrated in a modular design with common gas manifolds for hydrogen, air, and coolant to produce 100 kWe. An illustration of such a modular construction is shown in Figure 5.16.

As discussed in the above sections the cell active area pressure drops need to be compared to the manifold pressure drop. The pressure drop on the air and fuel sides are shown in Table 5.8 and for coolant are shown in Table 5.9 for a module with 24 cells, each with a cell active area of 30 cm × 30 cm. As seen earlier, when the coolant inlet temperature is increased (to

improve temperature uniformity over the cells and thus increase average current density), the coolant flow-rate required increases which leads to a higher pressure drop in the coolant circuit.

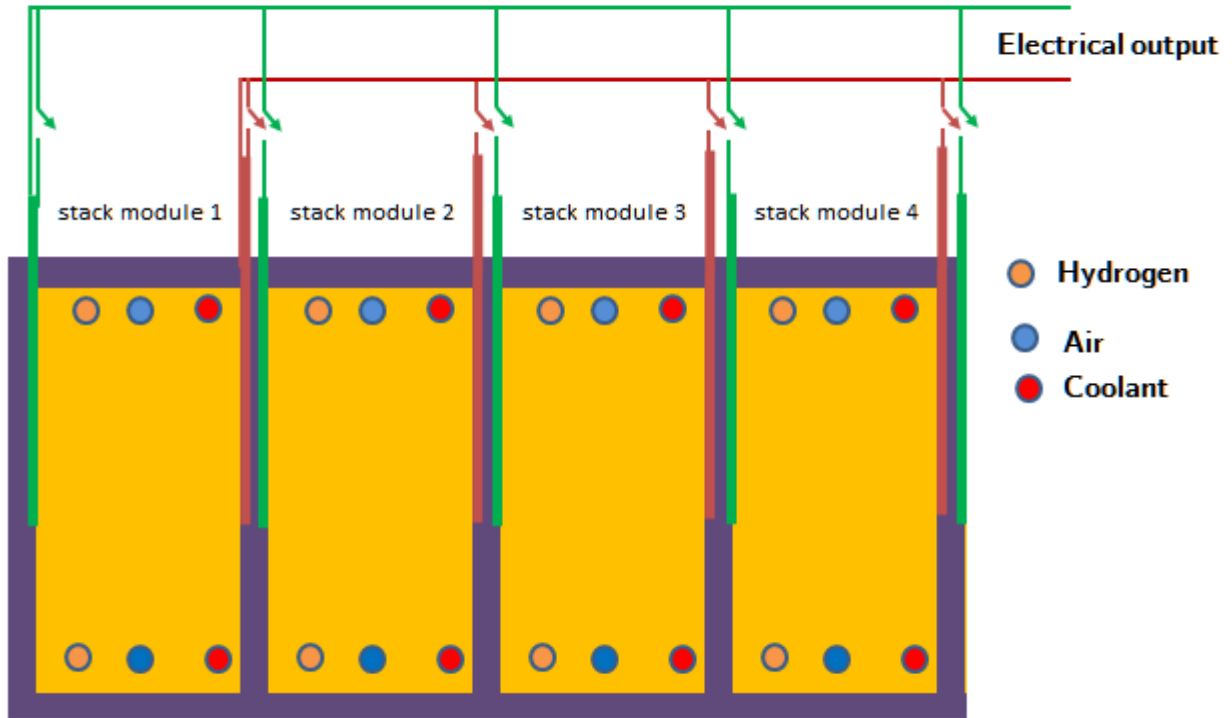


Figure 5.16: Schematic of modular arrangement of fuel cells.

Table 5.8: Air and fuel pressure drop variations in a module with 24 cells, each with a cell active area of 30 cm × 30 cm.

λ	Cathode air pressure drop (Pa)			Fuel pressure drop (Pa)		
	ΔP_{active}	$\Delta P_{\text{manifold}}$	ΔP_{total}	ΔP_{active}	$\Delta P_{\text{manifold}}$	ΔP_{total}
1	1974	719	2693	708	210	918
2	4498	2420	6918	1417	662	2078
3	6867	4920	11787	2125	1378	3503

Table 5.9: Coolant pressure drop variations in a module of 24 cells, each with a cell active area of 30 cm × 30 cm.

T _{Cin}	T _{Bin}	$\Delta P_{\text{manifold}}$ (Pa)			ΔP_{active} (Pa)			ΔP_{total} (Pa)		
		$\lambda = 1$	$\lambda = 2$	$\lambda = 3$	$\lambda = 1$	$\lambda = 2$	$\lambda = 3$	$\lambda = 1$	$\lambda = 2$	$\lambda = 3$
K	K									
400	300	22	21	19	932	876	782	954	897	801
450	300	2870	1151	521	33774	17429	11068	36644	18580	11589
450	350	3573	2086	1062	39996	25130	17503	43569	27216	18565
450	400	3759	2387	1412	37774	27358	20230	41533	29745	21642

5.6 Summary

- External liquid coolant is a better option for thermal management of stacks larger than 5 kWe while integrated air cooling can be used for stacks of about 1 kWe.
- In order to maintain high performance of the stack, the external coolant should be introduced at a high inlet temperature; pre-heating of cathode air also helps by further smoothing out temperature differences in the stack.
- Using a four-parallel serpentine flow field for the bipolar plates appears to be a good working compromise between the need for ensuring uniform reactant distribution and minimizing parasitic pumping losses.
- It may be sufficient to use parallel flow fields in the cooling plate to avoid excessive pressure drop losses which are associated with the need to operate at high coolant inlet temperatures. Use of wider parallel channels will have the dual advantage of increasing flow uniformity (by having fewer numbers of parallel channels) and lower pressure drop (by increasing the hydraulic diameter of the channel).
- It is possible to design branched external manifolds that can minimize pressure drops in the inlet and outlet manifolds while ensuring uniform distribution of the reactants and coolant in the stack.

CHAPTER-6

CONCLUSIONS

The heat generation rate in HT-PEMFC stacks is high at high current densities where it can exceed the total electric power output. The performance of an HT-PEMFC is highly sensitive to the operating temperature: a low cell temperature leads to a decrease in cell performance as well as efficiency while cell temperatures above $\sim 200^{\circ}\text{C}$ could damage the materials of the stack. These requirements pose a challenge to maintaining the temperature within the stack within acceptable limits. This challenge is especially severe in automobiles which operate at high current/power density during the acceleration phase of vehicular movement. Therefore, proper thermal management is required in order to prevent the formation of local hotspots and to maintain the high performance and durability of the fuel cells within the stack.

Against this background, the objective of the present work was to systematically study the thermal management of an HT-PEMFC stack, quantify the effect of various stack cooling strategies on the overall performance of the stack, and make specific design and operational recommendations for thermal management of HT-PEMFC stacks that can be used in small motor vehicles.

To this end, a multi-scale computational fluid dynamics (CFD) model of the stack model was developed by coupling the electrochemistry with the flow and temperature fields within the stack. While the flow and temperature fields are fully resolved in this model, the electrochemistry is simplified by using an empirical cell polarization curve to capture local current density. The local current density retains a dependence on local temperature within the active regions of each cell but is assumed to be independent of local reactant/product concentrations. This approach greatly reduces computational effort and time by removing the need for the extremely fine mesh resolution required to resolve the concentration and current fields within the catalyst and porous transport layers while retaining the essential physics and the coupling between the temperature and current density fields, thus enabling studies that clarify thermal management at the stack level: the focus of this study. A specific goal of this work was to investigate stack cooling methods that enable as high an average stack temperature as possible

while ensuring that the temperature does not exceed 200°C anywhere in the stack. A number of factors that have a bearing on the temperature distribution within the cell and the stack have been investigated using this model and this detailed parametric analysis of the HT-PEMFC stack shows that there is considerable scope for fine-tuning the thermal management of HT-PEMFC stacks to achieve a desired level of performance.

The following conclusions can be drawn from the present study:

- Integrated air cooling can keep the cell temperatures within required limits while also pre-heating the cathode air. However, a large stoichiometric factor of the order of 10, is required to maintain cell temperature below 200°C unless coupled with forced convective cooling flow over the stack.
- For transport applications requiring relatively small stacks (~1 kWe), where the stack is mounted on a moving vehicle, external cooling can be achieved by directing the flow of ambient air over the stack. In such a case, the stack can be operated at a reduced stoichiometric factor 4 to 5 for a vehicle velocity of 9 to 10 m/sec. This strategy will not work for larger stacks as the stack core temperatures may be unacceptably high.
- A combination thermal management system where integrated air cooling is coupled with a metal hydride H₂ storage system that serves as a heat sink appears viable. For the same operating conditions as for the integrated air cooling system alone, the required air flow-rate in this configuration is halved.
- While cathode air cooling is effective for small cell areas (of the order of 10 cm × 10 cm), larger cell areas require an external liquid coolant to maintain temperature variations between cells in the stack to within ~10 K.
- Liquid cooling allows the most uniform temperature and current density distributions among all cooling options studied. Temperature variations within cells in a stack can be reduced further by sending a liquid thermal oil with an inlet temperature close to the stack operating temperature. This will however lead to substantially higher pressure drops in the coolant circuit thus impacting the pumping requirements.
- In order to maintain high performance of the stack, pre-heating of cathode air helps by further smoothing out temperature differences in the catalyst layers to around 3-7 K.

- Use of graphite cooling plates, as opposed to copper plates. The thermal conductivity of the cooling plate is not a big consideration as using graphite instead of copper (copper's thermal conductivity is 20 times higher than that of graphite) results in a negligible performance loss while giving considerable gains in terms of the weight of the stack.
- One cooling plate for every four cells appears to be sufficient to maintain reasonably low temperature variation within the stack. Due to the inherently high conductivities of the thick coolant and bipolar plates (graphite) and the thinness of the low conductivity materials (like the MEA), the temperature gradients across the cell are reasonably low, thus permitting one coolant plate for every four cells.

Recommendations for future work

The work reported in the thesis can be extended to include the following points for further investigation:

- Resolution of the reactant flow field effects. This requires a full coupling of the flow, temperature, mass transfer and electrochemical effects and will bring out further anomalies associated with the variation of the concentration of the reactants over the cell and the stack.
- Resolution of stack and system dynamics. The present study has considered steady state operation. In a dynamic situation, the response of the various phenomena will be different and the heat transfer at cell and stack level is expected to be slowest to respond. Such effects on the performance of the stack in the short term, as well as in the long term, can be investigated further.

REFERENCES

- Adzakpa, K.P., Ramousse, J., Dube, Y., Akremi, H., Agbossou, K., Dostie, M., Poulin, A., Fournier, M., 2008. Transient air cooling thermal modeling of a PEM fuel cell. *J. Power Sources* 179, 164-176.
- Ahluwalia, R., 2007. Sodium alanate hydrogen storage system for automotive fuel cells. *Int. J. Hydrogen Energy* 32, 1251-1261.
- Ahluwalia, R., Hua, T., Peng, J., 2011. On-board and Off-board performance of hydrogen storage options for light-duty vehicles. *Int. J. Hydrogen Energy* 37, 2891-2910.
- Andreasen, S.J., Ashworth, L., Reman, I.N.M., Rasmussen, P.L., Nielsen, M.P., 2008a. Modeling and implementation of a 1 kW, air cooled HTPEM fuel cell in a hybrid electrical vehicle. *ECS Trans.* 12, 639-650.
- Andreasen, S.J., Kær, S.K., 2008b. Modelling and evaluation of heating strategies for high temperature polymer electrolyte membrane fuel cell stacks. *Int. J. Hydrogen Energy* 33, 4955-4664.
- Aoki, M., Asano, N., Miyatake, K., Uchida, H., Watanabe, M., 2006. Durability of sulfonated polyimide membrane evaluated by long-term polymer electrolyte fuel cell operation. *J. Electrochem. Soc.* 153, A1154-A1158.
- Aoki, M., Uchida, H., Watanabe, M., 2006. Decomposition mechanism of perfluorosulfonic acid electrolyte in polymer electrolyte fuel cells. *Electrochem. Commun.*, 8, 1509-1513.
- Arsalis, A., 2012. Modeling and simulation of a 100 kW HT-PEMFC subsystem integrated with an absorption chiller subsystem. *Int. J. Hydrogen Energy* 37, 13484-13490.
- Asghari, S., Akhgar, H., Imani, B.F., 2011. Design of thermal management subsystem for a 5 kW polymer electrolyte membrane fuel cell system. *J. Power Sources* 196, 3141-3148.
- Baek, S.M., Yu, S.H., Nam, J.H., Kim, C.J., 2011. A numerical study on uniform cooling of large-scale PEMFCs with different coolant flow field designs. *Appl. Therm. Eng.* 31, 1427-1434.
- Barbir, F., 2005. *PEM Fuel Cells: Theory and Practice*, Academic Press, New York.
- Bergmann, A., Gerteisen, D., Kurz, T., 2010. Modelling of CO poisoning and its dynamics in HTPEM fuel cells. *Fuel Cells*, 10, 278-287.
- Bernardi, D.M., 1990. Water balance calculations for solid polymer electrolyte fuel cells. *J. Electrochem. Soc.* 137, 3344-3350.
- Bernardi, D.M., Verbrugge, M.W., 1992. A mathematical model of the solid-polymer-electrolyte fuel cell. *J. Electrochem. Soc.* 139, 2477-2491.

- Bose, S., Kuila, T., Nguyen, T.X.H., Kim, N.H., Lau, K.T., Lee, J.H., 2011. Polymer membranes for high temperature proton exchange membrane fuel cell: recent advances and challenges. *Prog. Polym. Sci.* 36, 813-836.
- Breiter, M.W., 1969. *Electrochemical Processes in Fuel cells*. Springer-Verlag Berlin, New York.
- Buchi, F.N., Gupta, B., Haas, O., Scherer, G.G., 1995. Study of radiation grafted FEP-G-polystyrene membranes as polymer electrolytes in fuel cells. *Electrochim. Acta* 40, 345-353.
- Carrette, L., Friedrich, K.A., Stimming, U., 2001. *Fuel Cells-Fundamentals and Applications*. Fuel Cells 1, 5-39.
- Chang, P.A.C., St-Pierre, J., Stumper, J., Wetton, B., 2006. Flow distribution in proton exchange membrane fuel cell stacks. *J. Power Sources* 162, 340-355.
- Cheddie, D.F., Munroe, N.D.H., 2005. Review and comparison of approaches to proton exchange membrane fuel cell modeling. *J. Power Sources* 147, 72-84.
- Cheddie, D.F., Munroe, N.D.H., 2006a. Parametric model of an intermediate temperature PEMFC. *J. Power Sources* 156, 414-423.
- Cheddie, D.F., Munroe, N.D.H., 2006b. Three dimensional modeling of high temperature PEM fuel cells. *J. Power Sources* 160, 215-223.
- Cheddie, D.F., Munroe, N.D.H., 2006c. Analytical correlations for intermediate temperature PEM fuel cells. *J. Power Sources* 160, 299-304.
- Cheddie, D.F., Munroe, N.D.H., 2006d. Two Dimensional Phenomena in Intermediate Temperature PEMFCs. *Int. J. Transport Phenomena* 8, 51-68.
- Cheddie, D.F., Munroe, N.D.H., 2006e. Mathematical model of a PEMFC using a PBI membrane. *Energy Conv. Management* 47, 1490-1504.
- Cheddie, D.F., Munroe, N.D.H., 2007. A two-phase model of an intermediate temperature PEM fuel cell. *Int. J. Hydrogen Energy* 32, 832-841.
- Cheddie, D.F., Munroe, N.D.H., 2008. Semi-analytical proton exchange membrane fuel cell modeling. *J. Power Sources* 183, 164-173.
- Cheng, C.H., Lin, H.H., 2009. Numerical analysis of effects of flow channel size on reactant transport in a proton exchange membrane fuel cell stack. *J. Power Sources* 194, 349-359.
- Choi, J., Kim, Y.H., Lee, Y., Lee, K. J., Kim, Y., 2008. Numerical analysis on the performance of cooling plates in a PEFC. *J. Mech. Sci. Technol.* 22, 1417-1425.

- Cozzolino, R., Cicconardi, S.P., Galloni, E., Minutillo, M., Perna, A., 2011. Theoretical and experimental investigations on thermal management of a PEMFC stack. *Int. J. Hydrogen Energy* 36, 8030-8037.
- Cunningham, B., 2007. The development of compression moldable polymer composite bipolar plates for fuel cells, Ph.D. Thesis, Virginia Polytechnic Institute and State University.
- Faghri, A., Guo Z., 2005. Challenges and opportunities of thermal management issues related to fuel cell technology and modeling. *Int. J. Heat Mass Transfer* 48, 3891-3920.
- Fluckiger, R., Tiefenauer, A., Ruge, M., Aebi, C., Wokaun, A.B., Chi, F.N., 2007. Thermal analysis and optimization of a portable, edge-air-cooled PEFC stack *J. Power Sources* 172, 324-333.
- Forde, T., Eriksen, J., Pettersen, A., Vie, P., Ulleberg, O., 2009. Thermal integration of a metal hydride storage unit and a PEM fuel cell stack. *Int. J. Hydrogen Energy* 34, 6730-6739.
- Geormezi, M., Deimede, V., Gourdoupi, N., Triantafyllopoulos, N., Neophytides, S., Kallitsis, J.K., 2008. Novel pyridine-based poly (ether sulfones) and their study in high temperature PEM Fuel Cells, *Macromolecules* 41, 9051-9056.
- Goebel, S.G., Evaporative cooled fuel cell, US Patent 6960404, assigned to General Motors Corporation.
- Grubb, W.T., Niedrach, L.W., 1960. Batteries with solid ion-exchange membrane electrolytes, II Low temperature hydrogen-oxygen fuel cells. *J. Electrochem. Soc.* 107, 131-135.
- Guo, Q., Pintauro, P.N., Tang, H., O'Connor, S., 1999. Sulfonated and crosslinked polyphosphazene-based proton-exchange membranes. *J. Membr. Sci.* 154, 175-181.
- Hawkes, G., O'Brien, J., Stoots, C., Hawkes, B., 2009. 3D CFD model of a multi-cell high-temperature electrolysis stack. *Int. J. Hydrogen Energy* 34, 4189-4197.
- Holman, J.P., 1986. *Heat Transfer*, 6th ed, McGraw-Hill, Singapore.
- Hu, J., Zhang, H., Zhai, Y., 2006. Performance degradation studies on PBI/H₃PO₄ high temperature PEMFC and one-dimensional numerical analysis. *Electrochim. Acta* 52, 394-401.
- Jalani, N.H., Ramani, M., Ohlsson, K., Buelte, S., Pacico, G., Pollard, R., Datta, R., 2006. Performance analysis and impedance spectral signatures of high temperature PBI-phosphoric acid gel membrane fuel cells. *J. Power Sources* 160, 1096-1103.
- Jiao, K., Li, X., 2010. A Three-Dimensional non-isothermal model of high temperature proton exchange membrane fuel cells with phosphoric acid doped polybenzimidazole membranes. *Fuel Cells*, 10, 351-362.

- Ju, H.C., Wang, C.Y., 2008. Effects of coolant channels on large-scale polymer electrolyte fuel cells (PEFCs). *Int. J. Automotive Technol.* 9, 225-232.
- Ju, H., Meng, H., Wang, C.Y., 2005. A single-phase, non-isothermal model for PEM fuel cells. *Int. J. Heat Mass Transfer* 48, 1303-1315.
- Ju, H., Meng, H., Wang, C.Y., 2005a. A single-phase, non-isothermal model for PEM fuel cells. *Int. J. Heat Mass Transfer* 48, 1303-1315.
- Ju, H., Wang, C.Y., Cleghorn, S., Beuscher, U., 2005b. Non-isothermal modeling of polymer electrolyte fuel cells I. Experimental Validation. *J. Electrochem. Soc.* 152, A1645-A1653.
- Kandlikar, S.G., Lu, Z., 2009. Thermal management issues in a PEMFC stack - A brief review of current status. *Appl. Therm. Eng.* 26, 1276-1280.
- Kim, H.J., Cho, S.Y., An, S.J., Eu, Y.C., Kim, J.Y., Yoon, H.K., Kweon, H.J., Yew, K.H., 2004. Synthesis of poly(2,5-benzimidazole) for use as a fuel-cell membrane. *Macromol Rapid Commun.* 25, 894-897.
- Koh, J.H., Hsu, A.T., Akay, H.U., Liou, M.F., 2005. Analysis of overall heat balance in self-heated proton-exchange-membrane fuel cells for temperature predictions. *J. Power Sources* 144, 122-128.
- Kordesch, K., 1963. Fuel cells, Chapter 8, Academic Press, New York.
- Korsgaard, A.R., Nielsen, M.P., Bang, M., Kær, S.K., 2006a. Modeling of CO influence in PBI electrolyte PEM fuel cells. The 4th International Conference on Fuel Cell Science, Engineering and Technology June 19-21, Irvine, CA.
- Korsgaard, A.R., Nielsen, M.P., Kær, S.K., 2008a. Part one: A novel model of HTPEM-based micro-combined heat and power fuel cell system. *Int. J. Hydrogen Energy* 33, 1909-1920.
- Korsgaard, A.R., Nielsen, M.P., Kær, S.K., 2008b. Part two: Control of a novel HTPEM-based micro combined heat and power fuel cell system. *Int. J. Hydrogen Energy* 33, 1921-1931.
- Korsgaard, A.R., Refshauge, R., Nielsen, M.P., Bang, M., Kær, S.K., 2006b. Experimental characterization and modeling of commercial polybenzimidazole-based MEA performance. *J. Power Sources* 162, 239-245.
- Kulikovsky, A.A., Oetjen, H.F., Wannek, C., 2010. A Simple and accurate method for high temperature PEM fuel cell characterisation. *Fuel Cells* 10, 363-368.
- Kvesic, M., Reimer, U., Froning, D., Luke, L., Lehnert, W., Stolten, D., 2012. 3D modeling of a 200 cm² HT-PEFC short stack. *Int. J. Hydrogen Energy* 37, 2430-2439.
- Kvesic, M., Reimer, U., Froning, D., Luke, L., Lehnert, W., Stolten, D., 2012. 3D modeling of an HT-PEFC stack using reformat gas. *Int. J. Hydrogen Energy* 37, 12438-12450.

- Lampinen, M.J., Fomino, M., 1993. Analysis of Free energy and entropy changes for half cell reactions. *J. Electrochem. Soc.* 140, 3537-3546.
- Larminie, J., Dicks, A., 2000. *Fuel Cell Systems Explained*, Wiley, New York.
- Li, X., 2000. *Principles of Fuel Cells*, Taylor and Francis, New York.
- Liu, W., Zuckerboard, D., 2005. In-situ detection of hydrogen peroxide in PEM fuel cells. *J. Electrochem. Soc.* 152, A1165-A1170.
- Lobato, J., Caizares, P., Rodrigo, M.A., Pinar, F.J., Ubeda, D., 2011. Study of flow channel geometry using current distribution measurement in a high temperature polymer electrolyte membrane fuel cell. *J. Power Sources* 196, 4209-4217.
- Lobato, J., Caizares, P., Rodrigo, M.A., Piuleac, C.G., Curteanu, S., Linares, J.J., 2010. Direct and inverse neural networks modelling applied to study the influence of the gas diffusion layer properties on PBI-based PEM fuel cells. *Int. J. Hydrogen Energy* 35, 7889-7897.
- Lobato, J., Canizares, P., Rodrigo, M.A., Pinar, F.J., Mena, E., Beda, D.U., 2010. Three-dimensional model of a 50 cm² high temperature PEM fuel cell. Study of the flow channel geometry influence. *Int. J. Hydrogen Energy* 35, 5510-5520.
- Lobato, J., Canizares, P., Rodrigo, M.A., Pinar, F.J., Mena, E., Beda, D.U., 2010. Three-dimensional model of a 50 cm² high temperature PEM fuel cell. Study of the flow channel geometry influence. *Int. J. Hydrogen Energy* 35, 5510-5520.
- Luke L., Janben, H., Kvesic, M., Lehnert, W., Stolten, D., 2012. Performance analysis of HT-PEMFC stacks. *Int. J. Hydrogen Energy* 37, 9171-81.
- Mamlouk, M., Sousa, T., Scott, K., 2011. A High Temperature Polymer Electrolyte Membrane Fuel Cell Model for Reformate Gas. *Int. J. of Electrochem.* 2011, 1-18.
- Matian, M.A.M., Brandon, N.A., 2010a. application of thermal imaging to validate a heat transfer model for polymer electrolyte fuel cells. *Int. J. Hydrogen Energy* 35, 12308-12316.
- Matian, M., Marquis, A., Brandon, N., 2010b. An experimentally validated heat transfer model for thermal management design in polymer electrolyte fuel cells, *Proceedings of IMechE Part A: J. Power and Energy* 224, 1069-1082.
- McBride, B.J., Zehe, M.J., Gordon, S., 2002. NASA glenn coefficients for Calculating thermodynamic properties of individual species, NASA report TP-2002-211556.
- Merlo, L., Ghielmi, A., Cirillo, L., Gebert, M., Arcella, V., 2007. Resistance to peroxide degradation of Hyflon Ion membranes. *J. Power Sources* 171, 140-147.

- Niedrach, L.W., Alford, H.R., 1965. A new high-performance fuel cell employing conducting-porous-teflon electrodes and liquid electrolytes. *J. Electrochem. Soc.* 112, 117-124.
- Oono, Y., Fukuda, T., Sounai, A., Hori, M., 2010. Influence of operating temperature on cell performance and endurance of high temperature proton exchange membrane fuel cells. *J. Power Sources* 195, 1007-1014.
- Pandiyan, S., Jayakumar, K., Rajalakshmi, N., Dhathathreyan, K., 2008. Thermal and electrical energy management in a PEMFC stack - An analytical approach. *Int. J. Heat Mass Transfer* 51, 469-473.
- Park, S.K., Choe, S.Y., 2008. Dynamic modeling and analysis of a 20-cell PEM fuel cell stack considering temperature and two-phase effects. *J. Power Sources* 179, 660-672.
- Peng, J., Lee, S.J., 2006. Numerical simulation of proton exchange membrane fuel cells at high operating temperature. *J. Power Sources* 162, 1182-1191.
- Peng, J., Shin, J.Y., Song, T.W., 2008. Transient response of high temperature PEM fuel cell, *J. Power Sources* 179, 220-231.
- Pfeifer, P., Wall, C., Jensen, O., Hahn, H., Fichtner, M., 2009. Thermal coupling of a high temperature PEM fuel cell with a complex hydride tank. *Int. J. Hydrogen Energy* 34, 3457-3466.
- Rajalakshmi, N., Pandiyan, S., Dhathathreyan, K., 2008. Design and development of modular fuel cell stacks for various applications. *Int. J. Hydrogen Energy* 33, 449-454.
- Rao, R.M., Bhattacharyya, D., Rengaswamy, R., Choudhury, S.R., 2007. A two-dimensional steady state model including the effect of liquid water for a PEM fuel cell cathode. *J. Power Sources* 173, 375-393.
- Roos, M., Batawi, E., Harnisch, U., Hocker, T., 2003. Efficient simulation of fuel cell stacks with the volume averaging method. *J. Power Sources* 118, 86-95.
- Sasmito, A.P., Birgersson, E., Mujumdar, A.S., 2011. Numerical evaluation of various thermal management strategies for polymer electrolyte fuel cell stacks. *Int. J. Hydrogen Energy* 36, 12991-13007.
- Sasmito, A.P., Lum, K., Birgersson, E., Mujumdar, A., 2010. Computational study of forced air-convection in open-cathode polymer electrolyte fuel cell stacks. *J. Power Sources* 195, 5550-5563.
- Schmidt, H., Buchner, P., Datz A., Dennerlein, K., Lang, S., Waidhas, M., 2002. Low-cost air-cooled PEFC stacks. *J. Power Sources* 105, 243-249.
- Scholta, J., Messerschmidt M., Jorissen L., Hartnig, C., 2009. Externally cooled high temperature polymer electrolyte membrane fuel cell stack. *J. Power Sources* 190, 83-85.

- Scholta, J., Zhang, W., Jorissenc, L., Lehnertd, W., 2008. Conceptual Design for an Externally Cooled HT-PEMFC Stack. *ECS Trans.* 12, 113-18.
- Scott, K., Mamlouk, M., 2009. A cell voltage equation for an intermediate temperature proton exchange membrane fuel cell. *Int. J. Hydrogen Energy* 34, 9195-9202.
- Scott, K., Pilditch, S., Mamlou, M., 2007. Modelling and experimental validation of a high temperature polymer electrolyte fuel cell. *J. Appl. Electrochem.* 37, 1245-1259.
- Shahsavari, S., Desouza, A., Bahrami, M., Kjeang, E., 2012. Thermal analysis of air-cooled PEM fuel cells. *Int. J. Hydrogen Energy* 7, 18261-18271.
- Shamardina, A., Chertovich, A., Kulikovskiy, A.A., Khokhlov, A.R., 2010. A simple model of a high temperature PEM fuel cell. *Int. J. Hydrogen Energy* 35, 9954-9962.
- Shamardina, O., Kulikovskiy, A.A., Chertovich, A.V., Khokhlov, A.R., 2012. A model for high temperature PEM fuel cell: the role of transport in the cathode catalyst layer. *Fuel Cells* 12, 577-582.
- Siegel, C., Bandlamudi, G., Heinzl, A., 2010. Systematic characterization of a PBI/H₃ PO₄ sol-gel membrane-Modeling and simulation. *J. Power Sources* 196, 2735-2749.
- Sohn, Y.J., Park, G.G., Yang, T.H., Yoon, Y.G., Lee, W.Y., Yim, S.D., Kim, C.S., 2006. Operating characteristics of an air-cooling PEMFC for portable applications. *J. Power Sources* 145, 604-609.
- Song, T.W., Choi, K.H., Kim, J.R., Yi, J.S., 2011. Pumpless thermal management of water-cooled high-temperature proton exchange membrane fuel cells. *J. Power Sources* 196, 4671-79.
- Sousa, T., Mamlouk, M., Scott, K., 2010a. An isothermal model of a laboratory intermediate temperature fuel cell using PBI doped phosphoric acid membranes. *Chem. Eng. Sci.* 65, 2513-2530.
- Sousa, T., Mamlouk, M., Scott, K., 2010b. A Non-isothermal Model of a Laboratory Intermediate Temperature Fuel Cell Using PBI Doped Phosphoric Acid Membranes. *Fuel Cells* 10, 993-1012.
- Srinivasrao, M., Bhattacharyya, D., Rengaswamy, R., Narasimhan, S., 2010. Performance analysis of a PEM fuel cell cathode with multiple catalyst layers *Int. J. Hydrogen Energy* 35, 6356-6365.
- Suresh, N.S., Jayanti, S., 2011. Cross-over and performance modeling of liquid-feed Polymer Electrolyte Membrane Direct Ethanol Fuel Cells. *Int. J. Hydrogen Energy* 36, 14648-14658
- Tao, W.Q., Min, C.H., Liu, X.L., He, Y.L., Yin, B.H., Jiang, W., 2006. Parameter sensitivity examination and discussion of PEM fuel cell simulation model validation: Part I. Current status of modeling research and model development. *J. Power Sources* 160, 359-373.

- Trogadas, P., Parrondo, J., Ramani, V., 2008. Degradation mitigation in polymer electrolyte membranes using cerium oxide as a regenerative free-radical scavenger, *Electrochem. Solid State Lett.* 11, B113-B116.
- Trogadas, P., Ramani, V., 2007. Pt/C/MnO₂ hybrid electrocatalysts for degradation mitigation in polymer electrolyte fuel cells. *J. Power Sources* 174, 159-163.
- Ubong, E.U., Shi, Z., Wang, X., 2009. Three-dimensional modeling and experimental study of a high temperature PBI-based PEM fuel cell. *J. Electrochem. Soc.* 156, B1276-B1282.
- Verda, V., Sciacovelli, A., 2011. Design improvement of circular molten carbonate fuel cell stack through CFD Analysis. *Appl. Therm. Eng.* 31, 2740-2748.
- Wang, C.P., Chu, H.S., Yan, Y.Y., Hsueh, K.L., 2007. Transient evolution of carbon monoxide poisoning effect of PBI membrane fuel cells. *J. Power Sources* 170, 235-241.
- Wang, C.Y., Gu, W.B., Liaw, B.Y., 1998. Micro-macroscopic coupled modeling of batteries and fuel cells. *J. Electrochem. Soc.* 145, 3407-3417.
- Wang, J.T., Savinell, R., Wainright, J., Litt M., Yu, H., 1996. A H₂-O₂ fuel cell using acid doped polybenzimidazole as polymer electrolyte. *Electrochim. Acta* 41, 193-197
- Wu, J., Galli, S., Lagana, I., Pozio, A., Monteleone, G., Yuan, X.Z., Martin, J., Wang, H., 2009. An air-cooled proton exchange membrane fuel cell with combined oxidant and coolant flow. *J. Power Sources* 188, 199-204.
- Xie J., Wood, D.L., Wayne, D.M., Zawodzinski, T.A., Atanassov, P., Borup, R.L., 2005. Durability of PEFCs at high humidity conditions. *J. Electrochem. Soc.* 152, A104-A113.
- Xing, D.M., Zhang, H.M., Wang, L., Zhai, Y.F., Yi, B.L., 2007. Investigation of the AgSiO₂/sulfonated poly(biphenyl ether sulfone) composite membranes for fuel cell. *J. Membr. Sci.* 296, 9-14.
- Xu, H., Hou, X., 2007. Synergistic effect of CeO₂ modified Pt/C electrocatalysts on the performance of PEM fuel cells. *Int. J. Hydrogen Energy* 32, 4397-4401.
- Yu, S.H., Sohn, S., Nam, J.H., Kim, C.J., 2009. A numerical study to examine the performance of multi-pass serpentine flow fields for cooling plates in polymer electrolyte membrane fuel cells. *J. Power Sources* 194, 697-03.
- Yu, S., Jung D., 2008. Thermal management strategy for a proton exchange membrane fuel cell system with a large active cell area, *Renew. Energ.* 33, 2540-2548.
- Yu, X., Zhou, B., Sobiesiak, A., 2005. Water and thermal management for Ballard PEM fuel cell stack. *J. Power Sources* 147, 184-195.

Zenith F., Seland, F., Edvard, O., Børresen, B.R., Tunold, R., Skogestad, S., 2006. Control-oriented modeling and experimental study of the transient response of a high-temperature polymer fuel cell. *J. Power Sources* 162, 215-227

Zhang, G., Kandlikar, S.G., 2012. A critical review of cooling techniques in proton exchange membrane fuel cell stacks. *Int. J. Hydrogen Energy* 37, 2412-2429.

Zhang, J., Tang, Y., Song, C., Zhang, J., 2007. Polybenzimidazole membrane based PEM fuel cell in the temperature range of 120-200°C. *J. Power Sources* 72, 163-171.

Zhang, J., Xie Z., Zhang, J., Tang Y., Song C., Navessin, T., Shi, Z., Song, D., Wang, H., Wilkinson, D.P., Liu, Z.S., Holdcroft, S., 2006. High temperature PEM fuel cells. *J. Power Sources* 160, 872-891.

Zhang, Y., Ouyang, M., Lu Q., Luo, J., Li, X., 2004. A model predicting performance of proton exchange membrane fuel cell stack thermal systems. *Appl. Therm. Eng.* 24, 501-513.

Zhou, C., Guerra, M.A., Qiu, Z.M., Zawodzinski, J.T.A., Schiraldi, D.A., 2007. Chemical durability studies of perfluorinated sulfonic acid polymers and model compounds under mimic fuel cell conditions, *Macromolecules* 40, 8695-8707.

Zhou, T., Liu, H., 2001. A general three-dimensional model for proton exchange membrane fuel cells. *Int. J. Transport Phenomena* 3, 177-198.

APPENDIX

USER DEFINED FUNCTIONS

```

/*****
/* Volumetric Heat Source in Cathode Catalyst layers */
*****/
#include "udf.h"
#include "sg_udms.h"
#define Acell 0.01 /*Active area of the catalyst (m^2)*/
#define Volumecat 1.3e-7 /*Volume of the catalyst (m^3)*/
#define Vcell1 0.5 /* cell voltage (V) */
#define Vcell2 0.6 /* cell voltage (V) */
/***** Initialization *****/
DEFINE_INIT(temperature_initilazion,d)
{
    cell_t c;
    Thread *t;
    real xc[ND_ND];
thread_loop_c(t,d)
{
    begin_c_loop_all(c,t) /* loop over all cells */
    {
        C_CENTROID(xc,c,t);
        C_T(c,t) = 460.;
    }
    end_c_loop_all(c,t)
}
}
/***** If cell operated at 0.5 V voltage *****/
/* ***** Catalyst layer-1 0.5 V *****/

DEFINE_SOURCE(cat1_HIGHvheatsource, c, t, dS, eqn)
{
    real source, i_current1, delH1, i_cat1;
    real Tcat1;
    Tcat1 = C_T(c, t);
    if (Tcat1>=473)
    {
        source = 4.2111e+08;
        i_cat1= 0.8933;
    }

    else if (Tcat1>394.)
    {
        i_current1=(4.75e-07*Tcat1*Tcat1*Tcat1)-(0.0006153*Tcat1*Tcat1)+(0.2738*Tcat1)-41.22;
        delH1=(285830)+(3.6985255e-4*Tcat1*Tcat1*Tcat1) (0.4833076*Tcat1*Tcat1)+ (152.42584114
            *Tcat1)-68260.578987;
        source =(((delH1/(2*96485))-Vcell1)*(i_current1/Acell))/Volumecat;
        i_cat1=1*i_current1;
    }
    else if (Tcat1>300.)
    {
        source =0.9899e+08;
        i_cat1=0.1929;
    }
}

```

```

    }
else
    {
    source =0.0;
    dS[eqn]=0.0;
    }
    C_UDMI(c, t,0) = Tcat1;      Set_User_Memory_Name(0,"cat1_temperature");
    C_UDMI(c, t,1) = source;     Set_User_Memory_Name(1,"cat1_heatsource");
    UDMI(c, t,2) = i_cat1;      Set_User_Memory_Name(2,"cat1_curentdensity");
return source;
}
/*****If cell operated at 0.5 V voltage *****/
/* **** Catalyst layer-2 0.5 V *****/

DEFINE_SOURCE(cat2_HIGHvheatsource, c, t, dS, eqn)
{
    real source, i_current2, delH2, i_cat2;
    real Tcat2;
    Tcat2 =C_T(c, t);
    if (Tcat2>=473)
    {
        source =4.2211e+08;
        i_cat2=0.8933;
    }
    else if (Tcat2 >394.)
    {
        i_current2=(4.75e-07*Tcat2*Tcat2*Tcat2)-(0.0006153*Tcat2*Tcat2)+(0.2738*Tcat2)-41.22;
        delH2=(285830)+(3.6985255e-4*Tcat2*Tcat2*Tcat2)-(0.4833076*Tcat2*Tcat2) +(152.42584114
            *Tcat2)-68260.578987;
        source =(((delH2/(2*96485))-Vcell1)*(i_current2/Acell))/Volumecat;
        i_cat2=1*i_current2;
    }
    else if (Tcat2>300.)
    {
        source =0.9899e+08;
        i_cat2=0.1929;
    }
    else
    {
        source =0.0;
        dS[eqn]=0.0;
    }
    C_UDMI(c, t,3) = Tcat2;      Set_User_Memory_Name(3,"cat2_temperature");
    C_UDMI(c, t,4) = source;     Set_User_Memory_Name(4,"cat2_heatsource");
    C_UDMI(c, t,5) = i_cat2;      Set_User_Memory_Name(5,"cat2_curentdensity");
return source;
}
/*****If cell operated at 0.6 V voltage *****/
/* **** Catalyst layer-1 0.6 V *****/

```

```

DEFINE_SOURCE(cat1_LOWveatsource, c, t, dS, eqn)
{
    real source, i_current1, delH1, i_cat1,cat1_heatsource;
    real Tcat1;
    Tcat1 = C_T(c, t);
    if (Tcat1>473)

```

```

    {
      source =1.7596e+08; ;
      i_cat1=0.4200;
    }
    else if (Tcat1>394.)
    {
      i_current1=(1.377e-7*Tcat1*Tcat1*Tcat1)-(0.0001767*Tcat1*Tcat1)+(0.07855*Tcat1)-11.77;
      delH1=(285830)+(3.6985255e-4*Tcat1*Tcat1*Tcat1)-(0.4833076*Tcat1*Tcat1)+ (152.42584114*
        Tcat1)-68260.578987;
      source =(((delH1/(2*96485))-Vcell2)*(i_current1/Acell))/Volumecat;
      i_cat1=1*i_current1;
    }
    else if (Tcat1>300.)
    {
      source =0.7297e+08;
      i_cat1=0.1672;
    }
    else
    {
      source =0.0;
      dS[eqn]=0.0;
      cat1_heatsource=source;
    }
    C_UDMI(c, t,0) = Tcat1;          Set_User_Memory_Name(0,"cat1_temperature");
    C_UDMI(c, t,1) = source;        Set_User_Memory_Name(1,"cat1_heatsource");
    C_UDMI(c, t,2) = i_cat1;       Set_User_Memory_Name(2,"cat1_currentdensity");
return source;
}
/*****If cell operated at 0.6 V voltage *****/
/* **** Catalyst layer-2 0.6 V *****/

```

```

DEFINE_SOURCE(cat2_LOWveatsource, c, t, dS, eqn)

```

```

{
  real source, i_current2, delH2, i_cat2;
  real Tcat2;
  Tcat2 =C_T(c, t);

  if (Tcat2>473)
  {
    source =1.7596e+08; ;
    i_cat2=0.4200;
  }
  else if (Tcat2 >394.)
  {
    i_current2=(1.377e-7*Tcat2*Tcat2*Tcat2)-(0.0001767*Tcat2*Tcat2)+(0.07855*Tcat2)-11.77;
    delH2=(285830)+(3.6985255e-4*Tcat2*Tcat2*Tcat2)-(0.4833076*Tcat2*Tcat2)+ (152.42584114
      *Tcat2)-68260.578987;
    source =(((delH2/(2*96485))-Vcell2)*(i_current2/Acell))/Volumecat;
    i_cat2=1*i_current2;
  }
  else if (Tcat2>300.)
  {
    source =0.7297e+08;
    i_cat2=0.1672;
  }
  else

```

```
{
source =0.0;
    dS[eqn]=0.0;
}
C_UDMI(c, t,3) = Tcat2;      Set_User_Memory_Name(3,"cat2_temperature");
C_UDMI(c, t,4) = source;    Set_User_Memory_Name(4,"cat2_heatsource");
C_UDMI(c, t,5) = i_cat2;    Set_User_Memory_Name(5,"cat2_curentdensity");
return source;
}
```

LIST OF PUBLICATIONS BASED ON THESIS

Refereed journal papers

- Reddy E.H., Monder D.S., Jayanti, S., 2013. Parametric study of an external coolant system for a high temperature polymer electrolyte membrane fuel cell. *Appl. Therm. Eng.* **58**, 155-164.
- Reddy E.H., Jayanti, S., 2012. Thermal coupling studies of a high temperature proton exchange membrane fuel cell stack and a metal hydride hydrogen storage system. *Energy Procedia* **29**, 254-264.
- Reddy E.H., Jayanti, S., 2012. Thermal management strategies for a 1 kWe stack of a high temperature proton exchange membrane fuel cell. *Appl. Therm. Eng.* **48**, 465-475.
- Reddy E.H., Monder D.S., Jayanti, S., 2013. Thermal management considerations in the scale-up of HT-PEMFC stack (Under preparation)

International conference papers

1. Jaggi V., Reddy E.H., Jayanti, S., An integrated ethanol reformer for high temperature PEM fuel cells, 6th Asian Conference on Electrochemical Power Sources, **ACEPS 2012**, 5th Jan- 8th Jan 2012, Chennai, INDIA.
2. Reddy E.H., Jayanti, S. Thermal coupling studies of a high temperature proton exchange membrane fuel cell stack and a metal hydride hydrogen storage system, 19th World Hydrogen Energy Conference (**WHEC-2012**), Toronto, 3rd Jun-8th Jun 2012, CANADA.

CURRICULUM VITAE

1. Name : Harikishan Reddy Ellamla

2. Date of Birth : 1st March 1983

3. Educational Qualifications

2005 Bachelor of Technology (B.Tech)

Institution : SRT Institute of Science and Technology, Nalgonda, AP
(Affiliated to JNT University, Hyderabad)

Specialization : Chemical Engineering

2008 Master of Technology (M.Tech)

Institution : National Institute of Technology – Rourkela

Specialization : Biochemical Engineering and Biotechnology

2013 Doctor of Philosophy (Ph.D)

Institution : Indian Institute of Technology – Hyderabad

Registration : Jan, 2009

DOCTORAL COMMITTEE

- GUIDE(S)** : **Dr. Sreenivas Jayanti**
Professor
Department of Chemical Engineering, IIT Madras
- Dr. Dayadeep Monder**
Assistant Professor
Department of Chemical Engineering, IIT Hyderabad
- MEMBERS** : **Dr. Vinod Janardhanan**
Assistant Professor, HOD
Department of Chemical Engineering, IIT Hyderabad
- Dr. Raja Banerjee**
Assistant Professor
Department of Mechanical Engineering, IIT Hyderabad
- CHAIRPERSON** : **Dr. Raja Banerjee**
Assistant Professor
Department of Mechanical Engineering, IIT Hyderabad